HIGH TEMPERATURE DEFORMATION BEHAVIOR, THERMAL STABILITY AND IRRADIATION PERFORMANCE IN GRADE 92 STEEL

A Dissertation

Presented in Partial Fulfillment of the Requirements for the

Degree of Doctor of Philosophy

with a

Major in Materials Science and Engineering

in the

College of Graduate Studies

University of Idaho

by

Sultan Alsagabi

May 2014

Major Professor: Indrajit Charit, Ph.D.

Authorization to Submit Dissertation

This dissertation of Sultan Alsagabi, submitted for the degree of Doctor of Philosophy in Materials Science and Engineering titled "High Temperature Deformation Behavior, Thermal Stability and Irradiation Performance in Grade 92 Steel," has been reviewed in final form. Permission, as indicated by signatures and dates given below, is now granted to submit final copies to the College of Graduate Studies for approval.

Major Professor: _____ Date: _____
Indrajit Charit, Ph.D.

Committee Members: _____ Date: _____
Krishnan Raja, Ph.D.

_____ Date: _____
Batric Pesic, Ph.D.

_____ Date: _____
Gabriel Potirniche, Ph.D.

Department Administrator: _____ Date: _____
Wudneh Admassu, Ph.D.

Discipline's College Dean: _____ Date: _____
Larry A. Stauffer, Ph.D.

Final Approval and Acceptance

Dean of the College of Graduate Studies: _____ Date: _____
Jie Chen, Ph.D.

Abstract

The 9Cr-2W ferritic-martensitic steel (i.e. Grade 92 steel) possesses excellent mechanical and thermophysical properties; therefore, it has been considered to suit more challenging applications where high temperature strength and creep-rupture properties are required. The high temperature deformation mechanism was investigated through a set of tensile testing at elevated temperatures. Hence, the threshold stress concept was applied to elucidate the operating high temperature deformation mechanism. It was identified as the high temperature climb of edge dislocations due to the particle-dislocation interactions and the appropriate constitutive equation was developed. In addition, the microstructural evolution at room and elevated temperatures was investigated. For instance, the microstructural evolution under loading was more pronounced and carbide precipitation showed more coarsening tendency. The growth of these carbide precipitates, by removing W and Mo from matrix, significantly deteriorates the solid solution strengthening. The MX type carbonitrides exhibited better coarsening resistance. To better understand the thermal microstructural stability, long tempering schedules up to 1000 hours was conducted at 560, 660 and 760°C after normalizing the steel. Still, the coarsening rate of $M_{23}C_6$ carbides was higher than the MX-type particles. Moreover, the Laves phase particles were detected after tempering the steel for long periods before they dissolve back into the matrix at high temperature (i.e. 720°C). The influence of the tempering temperature and time was studied for Grade 92 steel via Hollomon-Jaffe parameter. Finally, the irradiation performance of Grade 92 steel was evaluated to examine the feasibility of its eventual reactor use. To that end, Grade 92 steel was irradiated with iron (Fe^{2+}) ions to 10, 50 and 100 dpa at 30 and 500°C. Overall, the irradiated samples showed some irradiation-induced hardening which

was more noticeable at 30°C. Additionally, irradiation-induced defect clusters and dislocation loops were observed and the irradiated samples did not show any bubble or void.

Vita

Sultan F. Alsagabi was born in Riyadh, the capital city of Saudi Arabia. He finished his high school and graduated in the top 10% of his graduating high school class which have him the opportunity to join the Mechanical Engineering Department at King Saud University in Riyadh in 1999. After that, Sultan finished his Bachelor degree in 2004 maintaining a GPA of 3.88 and was chosen to continue his higher education via the scholarship system in King Abdulaziz City for Science and Technology (KACST). Upon graduation, he was hired as a researcher at the Atomic Energy Research Institute (AERI) for two years. Then, Sultan joined the Materials Science & Engineering Department in August 2008 at the University of Idaho under the supervision of his advisor Dr. Indrajit Charit. In December 2009, he earned his Master's degree in Metallurgical Engineering after defending his thesis titled "Fundamental Studies on the Thermal Stability, Mechanical and Corrosion Characteristics of AZ31 Alloy." Then, Sultan came back to Saudi Arabia and worked at KACST for less than a year and was selected to pursue his Ph.D. degree. Thereafter, he joined the University of Idaho again in 2010 to complete his Ph.D. degree when he joined the Chemical and Materials Engineering Department. Finally, Sultan started his Ph.D. working in Grade 92 steel and is expected to graduate in May 2014.

Acknowledgements

I would like to thank my major professor Dr. Indrajit Charit for his guidance and encouragement during my degrees (Master and Ph.D.) in the University of Idaho. His Help was much appreciated as he has contributed significantly to guide me through the path. Also, my acknowledgement extended to my dissertation committee members Dr. Krishnan Raja, Dr. Batric Pesic and Dr. Gabriel Potirniche for their inputs and valued comments through the qualifying and preliminary exams, and the associated meetings. My thanks also extended to faculty and staff of Chemical and Materials Engineering Department and the Department chair Dr. Wudneh Admassu.

Moreover, I am thankful to my colleagues Triratna Shrestha and Somayeh Pasebani who helped me through my times here. Thanks also go to the Advanced Test Reactor National Scientific User Facility (ATR NSUF) for funding some parts of this work through the 13-452_ATR_RTE award after winning the Rapid Turnaround Experiment (RTE) proposals.

Dedication

This is dedicated to my family

Father, Mother, Brothers, Sisters

and my pregnant Wife.

Table of Contents

List of Figures

List of Tables

CHAPTER 1: The Mechanical Characteristics, Thermal Stability and Irradiation Performance in 9-12% Cr Ferritic-Martensitic (FM) Steels

Sultan Alsagabi [a,b], and Indrajit Charit [a]

[a] Chemical and Materials Engineering, University of Idaho, Moscow, ID 83844-3024, USA

[b] Atomic Energy Research Institute, King Abdulaziz City for Science and Technology, Riyadh, Saudi Arabia

Abstract

The ferritic-martensitic (FM) steels were discovered last century and the steel design has progressed significantly. The improvement desire is driven by the need to increase the thermal efficiency of steam power plants and meet the operational perspectives of nuclear plants. For instance, more sever working conditions are expected which requires the ability of designated materials to perform satisfactorily. The high strength of 9-12% Cr steels is attributed to the influence of the solid strengthening effect (i.e. such as Cr, Mo and W) and the associated fine and stable carbides and carbonitride precipitates. The initial tempered martensite will evolve during the exposure at higher temperature which induces the microstructural evolution of these steels. Several mechanisms such as lath widening, coarsening of strengthening precipitates and the precipitation of new phases can contribute substantially on the strength of these steels. On the other hand, 9-12% Cr ferritic-martensitic steels show good resistance to irradiation exposure; however, the latest generations of these steels have been studied briefly. Thus, new designed 9-12% Cr ferritic-martensitic steels have to be investigated extensively to address the irradiation-induced damage.

Keywords: FM steel; mechanical characteristics; irradiation performance; thermal stability

1.1. Introduction

The chromium containing ferritic-martensitic (FM) steels were introduced back in 1912 to be used as blades in steam turbines [1-2]. Since then, significant progress has been made in steel design as they found more applications in power generation plants [1-3]. Later during 1960s, the CrMoV steels such as HT9 steel (12Cr-1MoWV) with higher strength were introduced and they were utilized for a few decades [2-3]. Afterwards, the Grade 91 steel (9Cr-1Mo) was developed and the mechanical properties were enhanced as a result of the formation of stable precipitates such as V and Nb based carbides and carbonitrides [3-4]. Finally, Grade 92 steel was introduced with superior properties as a result of adding elements such as W and B and reducing the amount of Mo [3-4]. With the addition of these alloying elements, the mechanical properties have been further improved and ferritic-martensitic (FM) steels were found to serve under more challenging conditions. Thus, the solid solution strengthening mechanism was enhanced as a result of adding W, for instance. Many ferritic-martensitic (FM) steels such as Grade 91, Grade 92 and HT9 have attracted considerable interest as a result of the motivation to improve the efficiency of power generation plants [5-7]. This desire is driven by economic and environmental perspectives to address the growing energy demand. For instance, the Next Generation Nuclear Plant (NGNP) is expected to operate at higher temperatures than the currently operating nuclear plants [1, 5-7]. Also, the NGNP will be designed to operate for much longer time periods (beyond 60 years). Therefore, the ferritic-martensitic steel has the potential to be considered for those applications based on the enhanced properties [6-12].

Grade 92 steel (Fe-9Cr-0.5Mo-1.7W-Nb-V, wt%) is a promising ferritic-martensitic steel and is considered a modified version of the Grade 91 steel, 9Cr-1Mo steel [6]. The

nominal chemical composition of this steel is described as 9Cr-0.5Mo-1.8W-VNb (in wt. %) [7]. Grade 92 steel has much better high temperature strength and creep-rupture properties compared to Grade 91 steel [7]. This steel, in general, possesses extraordinary mechanical and thermophysical properties [6-8]. For instance, it has high strength, low thermal expansion and high thermal conductivity [8-9]. The following microstructural features influence the high temperature deformation properties of these materials: fine, uniformly dispersed carbides and/or carbonitrides which pin the grain boundaries and obstruct the dislocation movement [10-14]; the dislocation density within the martensitic laths; and solid solution strengthening of the matrix by elements such as W and other alloying elements [2]. In Grade 92 steel, the fine/stable carbides and carbonitrides are formed due to the presence of strong carbide/carbonitride formers like Nb and V [7-9]. Therefore, the movement of dislocations can be hindered and plastic deformation can be delayed by which superior strength can be achieved [10-16].

1.1.1. The alloying elements in 9-12% Cr steels

The alloying elements in 9-12% Cr steels are introduced for many reasons. For example, some elements have a solid solution strengthening effect and others are added to stabilize some beneficial phases with superior properties such as high temperature strength and corrosion performance [17-18]. The influence of the main alloying elements and their effects on the alloy properties can be summarized as follows:

a) Chromium (Cr):

Chromium is the principal alloying element in 9-12% Cr steels. Chromium is a carbide former and a ferrite stabilizing element [17-19]. Also, the addition of Cr has shown to

improve the corrosion performance although the steel is not in the rank of stainless steel (12 wt.% or more) [20].

b) Tungsten (W):

Tungsten is a carbide former and a ferrite stabilizing element [5]. Also, the addition of tungsten promotes the formation of the secondary Laves phase [22-23]. Tungsten enhances the high temperature strength mainly through the solid solution strengthening and helps in reducing the coarsening rate of the $M_{23}C_6$ carbide precipitates [24-26].

c) Carbon (C):

Carbon is an austenite stabilizer and the presence of carbon promotes the formation of the secondary hardening carbides and carbonitrides [16, 27]. Also, carbon occupies interstitial sites with more solubility in austenite than ferrite.

d) Molybdenum (Mo):

Molybdenum is a carbide former and a ferrite stabilizing element [28-29]. Molybdenum enhances the steels via solid solution strengthening and it also has a beneficial effect in stabilizing phases such as the M_2X phase and the $M_{23}C_6$ phase [16, 30].

e) Manganese (Mn):

Manganese is an austenite stabilizer; however, the addition of Mn can be tolerated as Mn promotes the undesirable and coarse phase (i.e. M_6C) which removes the W from the matrix and dissolve the main precipitates such as $M_{23}C_6$ [31-32].

f) Vanadium (V):

Vanadium is a strong carbide former and a ferrite stabilizing element [33]. Also, vanadium promotes the formation of MX-type carbonitride precipitates [33-34]. The presence of MX-type precipitates improves the creep performance in 9-12% Cr steels.

g) Nitrogen (N):

Nitrogen is an austenite stabilizer and promotes the formation of MX-type precipitates [35]. Like carbon, nitrogen occupies interstitial sites in iron lattice [35-36]. The amount of N in B-containing steels should be restricted as a result of the formation of BN phase which deteriorates the beneficial effects of N in the steels [35-37].

h) Niobium (Nb):

Niobium is a ferrite stabilizing element and promotes the formation of MX-type precipitates which enhances the strength in 9-12% Cr steels [38].

i) Silicon (Si):

Silicon is a ferrite stabilizing element and enhances the oxidation performance of the steel [39-40]. It has been noted that the formation and coarsening of Laves phase can be accelerated as more Si is introduced to the solid solution.

j) Boron (B):

Boron stabilizes the morphology of $M_{23}C_6$ precipitates and the martensitic lath structure [41-42]. Thus, the $M_{23}C_6$ precipitates in the B-containing steels have shown a lower coarsening rate in 9-12% Cr steels [41-42].

1.1.2. Microstructure of 9-12% Cr steels

Carbides and carbonitride precipitates in 9-12% Cr steels are formed during the standard heat treatment of these alloys which consists of austenization and tempering [1]. Firstly, the austenization occurs at temperature above the Ac_3, the temperature at which austenite begins to form during heating [1]. At that time, a fully austenitic microstructure is obtained where most of the carbides and nitrides are dissolved [1, 7, 10]. After that, the martensitic microstructure is introduced after quenching the steel rapidly from the austenitic field. As a result, the majority of C atoms in the austenitic steel remain in the solution and a supersaturated solid solution of C in the matrix is obtained. The martensitic steel is hard and brittle with high dislocation density [1, 10]. The martensite has a body centered tetragonal (BCT) crystal structure because of the distortion associated with the diffusionless transformation [1, 7]. The martensite start temperature (M_s) is the highest temperature at which austenite to martensite transformation starts during cooling the steel rapidly; but, the martensite finish temperature (M_f) is defined as the temperature at which the formation of the martensite finishes during steel cooling [1, 7, 10]. The martensite start temperature can be roughly estimated based on the alloying elements [1, 43]. For instance, in 9-12% Cr steels, martensite start temperature (M_s) can be estimated as [43]:

$$M_s = 550°C - 450C - 33Mn - 20Cr - 17Ni - 10W - 20V - 10Cu - 11Nb - 11Si + 15Co \quad (1.1)$$

Generally, the M_f temperature is related to the M_s temperature for a given alloy and can be approximately estimated as 93-110°C below the martensite starts temperature, M_s [44]. Finally, tempering is introduced to soften the steel [45]. During tempering, recovery which promotes the formation of subgrains and dislocation networks takes place [45-46]. Also, carbides and carbonitride particles precipitate during tempering [45-46]. Tempering of the

normalized structure leads to a stress-free and relaxed martensitic structure [1, 6]. Moreover, the precipitation of carbides, carbonitrides and nitrides occur following the reaction [6, 43, 47]

$$M_3C \rightarrow M_7C_3 + M_2X \rightarrow M_{23}C_6 + MX \rightarrow \text{Laves phase} + \text{Z-phase}. \quad (1.2)$$

Besides the solid strengthening effect, the unique properties of Grade 92 steel is mainly attributed to the fine and stable carbide and carbonitride precipitates which hinder the dislocations movement [48-53]. These precipitates were introduced as a result of adding specific elements such as carbon (C), molybdenum (Mo), niobium (Nb), vanadium (V) and nitrogen (N) [50-52]. After tempering 9-12% Cr steels, a typical tempered martensitic microstructure is obtained [1, 6]. The microstructure of the tempered martensitic/ferritic 9-12% Cr steel is composed of martensite laths containing high dislocation density and distributed precipitates, as shown in Figure 1.1 [53]. The main precipitates are distributed along the prior austenite grain boundaries (PAGBs) and martensitic lath boundaries [53]. For instance, different types of precipitates decorate the boundaries after tempering such as the primary precipitates of $M_{23}C_6$ and MX-type precipitates [1, 53]. These primary precipitates play a crucial role in pinning the dislocation movement and stabilizing the subgrain structure via pinning subgrain boundary migration [6, 53]. The main precipitates in 9-12% Cr steels can be classified, in general, into three groups [54-55]:

i) $M_{23}C_6$ precipitates $(Cr, Fe, Mo, W)_{23}C_6$: They are coarser than other precipitates during tempering.

ii) MX precipitates (Nb, V)(N, C): Smaller in size and enhance the high temperature strength.

iii) Secondary precipitates such as Laves phase $(Fe, Cr)_2(Mo, W)$ and Z-phase (Cr(V,Nb)N).

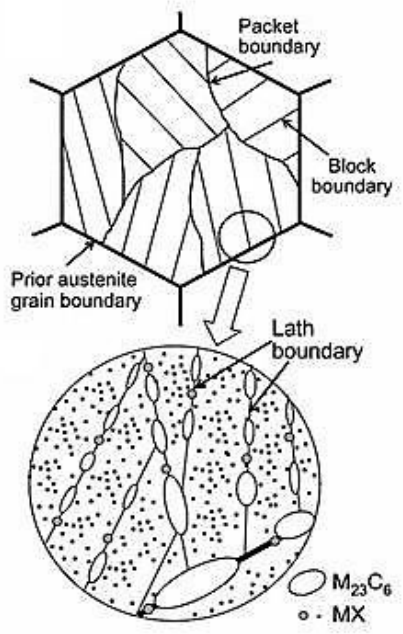

Figure 1.1. The microstructure of the tempered ferritic-martensitic 9-12% Cr steel [53].

Generally, the $M_{23}C_6$ carbide particles are coarser than other precipitates and precipitate preferentially on the prior austenite grain boundaries (PAGB), subgrain boundaries and martensite laths boundaries [6]. On the other hand, the MX-type precipitates are fine-type precipitates (i.e. (Nb, V)(N,C)) and appear, generally, in Grade 92 steel in three types [56]. To illustrate, fine spheroidal Nb(C,N), plate-like VN particles and some complex "V-wings" Nb(C,N)-VN [24]. During tempering, the undissolved precipitates during austenitizing, Nb(C, N) precipitates, act as nucleation sites for V-rich nitrides precipitates and the complex Nb(C,N)-VN precipitates are formed [6, 56]. Generally, the $M_{23}C_6$-type and MX-type precipitates have shown a good coarsening resistance within a wide range of temperatures which confirms the good high temperature resistance of these alloys [50-56]. The precipitate/dislocation interaction has shown to improve the mechanical performance of the

Grade 92 steel. To illustrate, the coarse $M_{23}C_6$ carbides were observed to precipitate preferentially on the prior austenite grain boundaries (PAGB), subgrain boundaries and martensite laths [6, 52-55]. As a result, subsequent grain growth can be retarded during tempering which influences the strength properties [6, 53-56]. Also, the fine MX precipitates have shown to improve mechanical properties of the Grade 92 alloys by pinning the free dislocations [6, 50-56].

The presence of strengthening precipitates enhances the high temperature strength of 9-12%Cr steels [50-52]. As the high temperature exposure occurs, many of these precipitates evolve as a result of being metastable in the first place [53]. For that purpose, the high temperature working condition, especially after long exposure hours, should be preciously noticed as some of these metastable precipitates might evolve because of the lower thermodynamic driving force of these metastable precipitates [52-56]. This is because of availability of the constituent elements to form these metastable precipitates or the lower associated strain energy involved in the development of these precipitates [55-56].

For a better understanding, the main precipitates involved in 9-12% Cr steels will be exhaustively discussed below [50-56]:

i) *$M_{23}C_6$ carbides*: This carbide evolves during tempering stages as they nucleate easily on PAGBs, lath and block boundaries [50, 57]. Theses precipitates usually enriched with Cr as a result of abundance of chromium in the matrix and the stability of these carbides [57-58]. They are coarser than other precipitates. Generally, $M_{23}C_6$ carbide is defined as the principal precipitate in 9-12% Cr steels and it has a face centered cubic structure [58-59]. These carbide

precipitates have good thermal stability but their coarsening deteriorates mechanical properties with time [57-59].

ii) *MX precipitates*: MX precipitates are finer than $M_{23}C_6$ carbide and they form when strong carbides and/or nitrides such as V, Nb or Ta are added to the matrix [34]. MX precipitates form during tempering on dislocations within the matrix or subgrain boundaries. Generally, they vary in size between 15-80 nm [60-61]. In 9-12% Cr steels, MX precipitates are enriched with vanadium and/or niobium rich carbonitrides. They stabilize the subgrain structure and impede the dislocation movement [60-62].

iii) *Laves phase*: Has a hexagonal crystal structure and recognized as $(Fe, Cr)_2(Mo, W)$. This intermetallic phase does not nucleate during tempering; however, it forms during the long exposure at elevated temperature [58, 27]. In 9-12% Cr steels, Laves phase is much abundant in Mo or W containing steels and it grows much faster in W-containing steels [63]. The Laves phase can be detected via backscattered electron (BSE) technique as the forming elements W and Mo appear brighter than others in the BSE mode because of their large atomic numbers [64]. They segregate along the PAGBs and lath boundaries [64]. The Laves phases can contribute to the overall strength in the beginning stages of its formation but as they grow in size they imply a loss in solid solution strengthening as a result of removing W/Mo from the matrix [26]. Therefore, Laves-phase should be avoided as it is not desirable in 9-12% Cr steels as their extensive growth would ultimately act as a cavity trigger [64-65].

iv) *Z-phase*: Z-phase has the formula of CrXN where X denotes Nb, V or Ta [18, 66]. It is very stable nitride precipitates at the working temperature of 600-700°C [18, 66]. The Cr content influences the precipitation kinetics of Z-phase [67]. Thus, it has been reported that the Z-phase is more pronounced in 11-12% Cr steels than 9% Cr steels [67]. For that reason, steels with lower Cr content show better creep strength; however, the higher Cr content steels suffer the breakdown in creep strength because of the progressive Z-phase precipitation [18, 66-67].

1.1.3. Strengthening mechanisms

The elevated temperature strength of 9-12% Cr steels can be enhanced as a result of strengthening the steel following several methods such as (i) solid solution strengthening, (ii) precipitation or dispersion strengthening, (iii) dislocation hardening, and (iv) boundary or sub-boundary hardening [42, 68]. Each strengthening mechanism operating in 9-12% Cr will be discussed below:

(i) *Solid solution strengthening*: As solute atoms are introduced into the matrix, they either occupy interstitial or substitutional sites. Thereafter, the presence of these solute atoms distort the parent lattice and introduces stress fields around these atoms [1, 25]. As a result, the dislocation movement will be hindered which contribute to strength of the matrix [1, 25]. In 9-12% Cr steels, the addition of solute elements such as Mo and W which have much larger atomic sizes than that of the solvent iron have been favored to produce solid solution strengthening effect in 9-12% Cr steels [1, 68-69]. Besides impeding the dislocation movement, the presence of tungsten in the matrix enhances the elevated temperature properties as a result of retardation of the migration of lath boundaries [68-69].

(ii) *Precipitation or dispersion hardening*: The microstructure of 9-12% Cr steels contains several types of precipitates [1]. These precipitates vary in size, shape and composition based on the compositional elements and scheduled heat treatment [1]. In 9-12% Cr steels, carbides and carbonitrides such as $M_{23}C_6$, MX and intermetallic compounds such as Laves phase were documented within the matrix and at grain/lath boundaries [34, 70]. In order for a dislocation to pass through a precipitate particle, the stress has to exceed the threshold stress [1, 70-72]. Several mechanisms have been proposed to explain the threshold stress such as Orowan's mechanism [68]. The Orowan's mechanism is expressed as [68]:

$$\sigma_{Or} = 0.8MGb/\lambda \quad (1.3)$$

where M is the Taylor factor (i.e. ~3), G shear modules, b the magnitude of Burgers factor and λ is the mean interparticle spacing [68]. Since the microstructure of 9-12%Cr steels does not contain any coherent particles, the particle cutting mechanism does not operate.

(iii) *Dislocation hardening*: As the dislocation density increases, the average distance between dislocations decreases; thus, dislocations start blocking the motion of each other [73-74]. The dislocation density is defined as the total dislocation length per unit volume of material [73]. The dislocation strengthening is given by:

$$\sigma_D = 0.5\, MGb(\rho_f)^{1/2} \quad (1.4)$$

where ρ_f is the dislocation density in the matrix. The elevated temperature exposure promotes the dislocation recovery as the microstructure becomes relaxed and dislocation annihilation becomes more pronounced [73-74]. Yet, the

tempered 9-12%Cr steels have high dislocation density in the range of $1\sim10\times10^{14}$ m^{-2} [73-74].

(iv) *Sub-boundary hardening*: The ferritic martensitic microstructure of the tempered 9-12%Cr steels consists of lath and block with a high dislocations density as shown in Fig. 1 [53]. The lath and block boundaries, after tempering, are considered as an elongated subgrains and they provide the sub-boundary hardening as they become barriers against the dislocation movement [1, 68]. The main precipitates, generally, are distributed preferentially along the prior austenite grain boundaries (PAGB) and the martensite lath boundaries. Therefore, they pin the movement of the subgrain structure [75-76]. The movement of these elongated subgrains softens the material as a result of the initiated dynamic recovery as this movement absorbs the excess dislocations inside the laths and blocks [1, 75-76]. The subgrain strengthening mechanism can be expressed by the following relation [68]:

$$\sigma_{sg} = 10Gb/\lambda_{sg} \quad (1.5)$$

where λ_{sg} is the short width of elongated subgrains .

1.1.4. Microstructural evolution of the tempered 9-12% Cr steels

As the ferritic-martensitic steel becomes exposed to elevated temperatures, the initial as-tempered martensite will evolve as a result of not being thermodynamically stable [77-78]. Therefore, it is important to understand the microstructural evolution mechanisms in order to optimize the evolution processes to enhance the achieved properties [78-79]. Microstructural evolution processes include, for instance, lath widening, carbide precipitate coarsening,

disappearance of PAGBs, precipitation of new undesirable phases and emergence of subgrains [1, 78-79]. Therefore, microstructural changes will be promoted under the influence of higher temperature and load which will reduce the overall strength of the material [53, 79].

The carbide coarsening (i.e. Ostwald ripening), for example, degrades the mechanical properties of steels as a result of increasing the average particle size [80-81]. The driving force for the carbide coarsening is the reduction of the interface free energy in the matrix; thus, particle with small size has higher surface to volume ratio [80]. So, as particles grow in size, the total free energy of the system will be reduced and this would be the driving force for the carbide coarsening [80-82]. The carbide coarsening rate of M_aC_b carbide in Fe-M-C, Ostwald ripening, is governed by the given equation:

$$r^3 - r_0^3 = k_3 t, \text{ and} \tag{1.6}$$

$$k_3 = 8(a+b)\sigma V D_M \mathcal{u}_M / 9aRT(\mathcal{u}_{pM} - \mathcal{u}_M)^2 \tag{1.7}$$

where r is the average particle size at the time t, r_0 is the average particle size at the time t=0, t is time, σ is the interfacial carbide energy, V is carbides molar volume, R is the gas constant, T is the temperature, D_M the volume diffusion of metal M, $\mathcal{u}_M$ and $\mathcal{u}_{PM}$ are the M concentrations in the matrix and carbides, respectively [82].

Even though carbides such as $M_{23}C_6$ in 9-12% Cr steels influence the strength properties of these steels, they have relatively high coarsening rate especially under long-term, elevated temperature exposure [50-53]. The $M_{23}C_6$ carbides form during tempering act as effective pining points, mainly in the range of 100–200 nm, against the migration of sub-grain boundaries and mobile dislocations. On the other hand, the MX-type precipitates are much

stable compared to other carbides even after long exposure time [1, 83]. Thus, they do not impair their size and chemical composition even after long aging periods [83].

Another microstructural evolution phenomenon is the coarsening of the subgrains as the ferritic/martensitic steel becomes exposed to elevated temperatures [84-85]. The subgrain coarsening rate depends on the stability of precipitates around the subgrain boundaries [20, 24-25]. However, those precipitates in contact with subgrains usually have higher coarsening rate as pipe diffusion would be more pronounced [85]. During the deformation, the subgrain size approaches a steady state value with respect to applied stress, this can be expressed as [86]:

$$w_{\infty} = k_w bG/\sigma \qquad (1.8)$$

where k_w is a numerical value of 10 for steels, b is Burgers vector, G shear modulus [86]. Therefore, the subgrain coarsening will occur in case the steady-state subgrain size was not achieved as stated in Eqn. 1.7 [87].

1.1.5. The irradiation performance of 9-12% Cr steels

When material becomes exposed to highly energetic radiation, atoms would be knocked out of their lattice original positions if the neutron collision has sufficient energy (i.e. more than the threshold energy E_d); otherwise, atoms would be vibrating around its equilibrium position and energy would be dissipated as heat through the lattice [1, 4]. Therefore, Primary Knock-on Atom (PKA) will be created if sufficient energetic radiation is involved and these PKAs would in turn produce further atomic dislodgements [4, 10]. As the primary knock-on atoms precede, secondary knock-on atoms are created leading to the production of the displacement cascades [4, 10]. The radiation damage induces microstructural changes that

include mechanisms such as the transmutation, dislocation loop forming and void swelling [1, 10]. Therefore, the irradiation induced microstructural evolution alters the mechanical properties of materials [4, 10].

The ferritic-martensitic 9-12% Cr steels, commonly, possess low swelling rates; swelling is defined as the ratio of the volume change to the original volume [88, 10]. Hence, 9-12% Cr steels can be considered for the structural applications that would see high amount radiation damage in advanced nuclear reactors [4, 10, 88].

1.2. Objectives

The specific objective of this dissertation research is to investigate one of the 9-12% Cr steels, Grade 92. In this work, the base material and the associated microstructure of the as-received material will be characterized. Also, tensile tests are performed at elevated temperatures and different strain rates to investigate the hot deformation behavior in Grade 92 steel. Correspondingly, the dominant high temperature deformation mechanism using the appropriate constitutive equations will be identified. Furthermore, the thermal stability will be investigated through a set of tempering schedules at different temperatures and times to investigate the induced microstructural changes. After that, the influence of the temper induced precipitates on the mechanical properties of Grade 92 steel will be studied. Finally, the irradiation performance of the investigated steel will be examined through studying the irradiation induced damage at different doses and temperatures. Thus, the mechanical properties and the microstructural evolution will be evaluated with respect to the irradiation induced damage.

The main foci of the proposed project is on understanding: (I) the high temperature deformation behavior of Grade 92 steel, (II) the thermal stability in Grade 92 steel at different temperatures and periods, and (III) the irradiation performance of Grade 92 steel. Therefore, the flow stress of Grade 92 steel will be analyzed at different temperatures (600 to 700°C) and strain rates (10^{-5} to 10^{-3} s^{-1}). Moreover, the dominant high temperature deformation mechanisms are identified using the Bird–Mukherjee–Dorn equation. However, the activation energy and the stress exponent are generally found higher for the high temperature deformation of the particle hardened alloys such as Grade 92 steel and they do not provide information on the intrinsic deformation mechanism. For instance, the presence of strengthening precipitates inhibits the dislocation movement, which explains the high stress exponents of particle-hardened alloys [1, 6]. So, to rationalize the observed deformation behavior of Grade 92 steel, the true stress exponent and activation energy of high temperature deformation will be evaluated using the threshold stress concept as applied to the modified Bird–Mukherjee–Dorn (BMD) equation [1, 6]. On the other hand, the thermal stability is evaluated through a set of tempering schedules. Times of 10, 100 and 1000 hours were chosen at temperatures of 560, 660 and 760°C. The experimental matrix was designed to investigate the evolution of main precipitates such as the $M_{23}C_6$, MX and secondary precipitates such as Laves phase. For instance, the evolution of the carbide precipitates and MX type precipitates is investigated with respect to temperature and time. Finally, the Laves phase is studied as it needs a temperature below 720°C and around 1000 hours to evolve. This part of the work will highlight the main precipitates in the Grade 92 steel and their influence on the mechanical properties. To have a better understanding, a tensile sample that corresponds to each tempering condition has been made to evaluate the

mechanical properties of tempered samples. Then, the irradiation performance in Grade 92 is evaluated at room temperature and elevated temperature. For instance, the microstructural evolution in Grade 92 using the iron ion irradiation is carried out at different radiation doses of 10, 50 and 100 displacements per atom (dpa) and temperatures of 30 and 500°C.

For each part of this work, the microstructure of the as-received, tempered, irradiated and fractured conditions are investigated using the appropriate instrumentations such as the optical microscopy (OM), scanning electron microscopy (SEM), transmission electron microscopy (TEM), and electron back-scattered diffraction (EBSD).

1.3. Background

1.3.1. Microstructural evolution of 9-12% Cr steels

The ferritic martensitic steel 9Cr-2W was modified from the previous generation steel Grade 91, modified 9Cr-1Mo [6]. Besides the solid solution strengthening effect, the excellent properties of Grade 92 alloys were mainly attributed to the fine and stable carbides and carbonitride precipitates which hinder the dislocations movement [10-11]. The precipitate/dislocation interaction has shown to improve the mechanical performance of Grade 92 steel. To illustrate, the coarse $M_{23}C_6$ carbides were observed to precipitate preferentially on the prior austenite grain boundaries (PAGBs), subgrain boundaries and martensite laths [6]. As a result, subsequent grain growth can be impeded during tempering which influences the strength properties [6, 47]. The fine MX precipitate, however, has shown to improve the mechanical properties of the Grade 92 steel by impeding the movement of dislocations [6, 47]. The temper induced precipitates in Grade 92 steel

exhibited good coarsening resistance which makes it a promising a high temperature alloy [1, 52-54].

The Thermo-Calc calculations for normalized Grade 92 steel revealed the influence of the main alloying elements at different tempering temperatures [55]. Thus, the Thermo-Calc calculations showed a complete dissolution of the $M_{23}C_6$ carbides after normalizing at 1050°C; however, some MX precipitates were detected after normalizing [55]. The previous result comes in good agreement with the work by Ennis *et al.* [6] that austenitizing at a temperature above 970°C was required to dissolve the $M_{23}C_6$ carbides; also, the MX precipitates remain undissolved even at a normalizing temperature of 1145°C [6, 55]. Moreover, there was a considerable mass fraction percentage difference between two of the main precipitates, $M_{23}C_6$ and MX [55]; the $M_{23}C_6$ carbides had more mass fraction than the MX [55]. As tempering temperature increases from 400 to 720°C, the coarsening rate of these two precipitates was low which was consistent with the findings of Ennis *et al.* [6, 55]. On the other hand, the Laves phase mass fraction was decreased significantly as temperature increased to 720°C. At that temperature, the Laves phase dissolved completely in the matrix [54, 55]. Also, the Laves phase formation requires a precipitation time of 103 hours or more, such as in creep, to be thermodynamically equilibrium [54-55]. So, the Laves phase is not expected to precipitate during normal tempering periods or short-term elevated temperature experiments [54-55].

As material becomes exposed to elevated temperature, significant microstructural changes occur such as dislocation density reduction and carbide coarsening [1, 4, 10]. For example, the coarsening of the coarse carbides $M_{23}C_6$ allows the martensite laths to transform to more equiaxed subgrains. However, coarsening of fine MX precipitates occurs

at a lower rate than $M_{23}C_6$ which alters the M composition (i.e. M refers to V or Nb) of these precipitates [1, 10, 52-56]. Also, Laves phase formation has been reported [16]. The formation of Laves phase takes place at elevated temperature, at temperature higher than 600°C, which coarsens rapidly especially under loading which degrades the mechanical properties of the material [1, 52-55]. Thereafter, the alloy strength was adversely affected as a result of weakening of the solid solution strengthening [25, 65]. The MX carbonitrides transform to Z-phase as a result of disappearance of the NbX during aging which introduces the VX as a result of the enrichment of Cr and Fe, which evolves eventually into Z-phase at later stages [88]. However, the Z-phase formation was observed during aging for more than 20,000 h in 10.5 wt.% Cr and the transition would be much slower in 9 wt. % Cr according to Yoshizawaa *et al.* [88]. To that end as the elevated temperature exposure takes place, the normalized and tempered microstructure undergoes evolution toward equilibrium with relatively large and near-equiaxed subgrains in the areas bound within the prior austenite grain boundaries (PAGB) [1, 10, 48].

The microstructural stability of Grade 92 steel has been investigated only in a limited fashion; therefore, more work has to be carried out in order to ensure the full understanding [6, 11, 67]. For instance, the prior austenite grain size increases with increasing austenitizing temperature. Also, the carbide precipitates (i.e. $M_{23}C_6$) are not dissolved during austenitizing at a temperature of 970°C; however, as austenitizing temperature increases to 1070°C, $M_{23}C_6$ precipitates are completely dissolved [6]. On the other hand, the Nb(C, N) precipitates did not dissolve even at austenitizing temperature of 1145°C; additionally, the particle diameter increased and its volume fraction decreased as austenitizing temperature increases [6]. These undissolved Nb(C, N) precipitates were found to act as nucleation sites

during tempering for the plate-like enriched-V precipitates; as a result, the well-known "V-wing" V-rich Nb(C, N) precipitates are formed, at a tempering temperature higher than 750°C. The hardness results seem to be independent of austenitizing temperature; thus, the hardness does not change with different austenitizing temperature according to Ennis *et al.* [6].

Tempering of the normalized structure introduces a stress-free and relaxed martensitic structure [6, 47, 49]. During tempering, dislocation density reduction and subgrain formation occur [47-49]. Further, various particles such as carbides, carbonitrides and nitride precipitation occur [6, 47]. Generally, the $M_{23}C_6$ carbide particles are coarser than other precipitates and have shown to precipitate preferentially on the prior austenite grain boundaries (PAGB), subgrain boundaries and martensite lath boundaries [6]. On the other hand, the MX-type precipitate are fine-type precipitates, (i.e. (Nb, V)(N,C) or (V, Nb)(N,C)), and was observed, generally, in Grade 92 alloy in three types [47]. To illustrate, fine spheroidal Nb(C,N), plate-like VN particles and some complex "V-wings" Nb(C,N)-VN [47]. Generally, the $M_{23}C_6$ carbides and MX-type precipitate have shown a good coarsening resistance within a wide range of temperatures which confirms the good high temperature resistance of these alloys [6, 47-49].

At lower tempering temperature around 400°C, the Fe-rich M_3C type precipitates along the undissolved MX (i.e. NbC) precipitates were revealed within the martensite laths of the tempered microstructure [55]. The enriched-Fe M_3C type precipitates appear as needle-like precipitates; on the contrary, the NbC precipitates have an equiaxed shape [55]. At higher tempering temperature (i.e. 525°C), the $M_{23}C_6$ carbides appeared as extended thin films on some high angle boundaries (HAB) of prior austenite grains; also, the M_3C and NbC

precipitates were retained within the martensite laths with no noticeable change [55]. Further increase in tempering temperature (i.e. 625°C) led to the dissolution of the M_3C type precipitates [6]. As tempering temperature increased, round-shaped $M_{23}C_6$ carbides were formed on the prior austenite grain boundaries (PAGBs), subgrain boundaries and martensite laths at higher temperature [55]. The equiaxed round-shaped $M_{23}C_6$ carbide formation occurred as a result of coagulation of the previously mentioned extended thin films $M_{23}C_6$ carbides and another independent precipitation of equiaxed $M_{23}C_6$ carbides where the latter mechanism largely dominates [55].

When tempering temperature was increased to 720°C, the martensite lath width increased noticeably [55]. Also, the thermodynamically equilibrium dispersion of $M_{23}C_6$ carbides seems to be revealed as a result of matching of the experimentally observed volume fraction with the Thermo-Calc calculated volume fraction [55]. These $M_{23}C_6$ carbides were equiaxed in shape and were present with almost 2% volume fraction.

The tempering of Grade 92 steel at different temperatures (i.e. 400-720°C) revealed that the $M_{23}C_6$ carbides can be distinguished into coarse $M_{23}C_6$ carbides on high angle boundaries and nano-scale $M_{23}C_6$ carbides within the lath boundaries [55]. But the MX type precipitates were only quantified with the enriched-Nb spheroidal MX precipitates with no V-enriched MX type precipitates formed [55]. According to Dudko *et al.* [55], the V-rich M(C, N) precipitation occurs at temperatures higher than 750°C. For example, the complex V-enriched MX-type precipitates were revealed at a tempering temperature of 775°C, V-wings type precipitates [6]. According to ref. [55], these complex Nb(C,N)-VN precipitates play a significant strengthening role; for that purpose, it has been believed that tempering in the range between 750-780°C influences the creep performance.

Statistically, during tempering between 400-835°C, the particle dimensions of the $M_{23}C_6$ carbides and the fine MX precipitates were measured at different tempering temperatures and both coarsened slightly, which indicates the superior high temperature strength of the Grade 92 steel [6, 55]. On the other hand, during tempering at temperatures higher than 750°C, the major axis length of the V-wing precipitates has increased considerably [6].

A long time annealing measurement has been carried out by Rodak *et al.* [56]; thus, the Grade 92 alloy has been annealed for 1000 hours at a temperature of 700°C. As a result, the subgrains were more homogeneous and equiaxed [56]. After annealing, the $M_{23}C_6$, MX and Laves phase were present. The $M_{23}C_6$ particle was the dominant particle type and it has shown to suppress the lath structure recovery. Particle coarsening rate was slow; particles were resistant to coarsening which comes in good agreement with refs. [6, 47, 55]. The Laves phase was expected to precipitate as a result of annealing for 1000 hours at a temperature below 720°C. The tungsten (i.e. W) concentration was quantified and it was found to increase after annealing in the $M_{23}C_6$ and the Laves phase [6, 47, 52-55]. The long time and high temperature exposure (> 500°C and $>10^3$ h) of Grade 92 steel showed that the subgrains are more homogeneous and equiaxed as compared to the tempered microstructure and the subgrain growth retardation is observed [24-25]. Also, the $M_{23}C_6$, MX and Laves phase are present. The $M_{23}C_6$ particle is the dominant particle type and it suppresses the recovery in the lath structures [6, 24-25]. The particle coarsening rate is slow and the Laves phase precipitates as a result of heat treatment for 10^3 hour at a temperature below 720°C [25]. However, as a result of the Laves phase formation, Mo and W are pulled out of the matrix which affects the solid solution strengthening effect adversely.

1.3.2. Mechanical properties of 9-12% Cr steels

As a result of considerable microstructural changes during tempering, the tempering temperature influences the hardness. As tempering temperature is increased from 400° to 720°C, there was a slight increase in hardness up to 525°C; afterwards, the hardness result decreased gradually as tempering temperature increased to 720°C [55]. For instance, tempering the Grade 92 steel in temperatures between 400-625°C did not reveal any significant change in dislocation density [55]. However, as tempering temperature increased to 720°C, there was a noticeable dislocation density reduction [55]. Further increasing in tempering temperature (i.e. 715-835°C), the hardness profile data decreased. Ennis *et al.* [6] indicated that the highest tempering temperature (i.e. 835°C) was associated with pronounced subgrain formation along with an estimated dislocation density around 2.3×10^{14} m^{-2}. However, it was 9×10^{14} m^{-2} after tempering at 715°C [6].

Given the importance of the mechanical properties of the Grade 92 steel, many researchers have studied mechanical properties of the ferritic-martensitic (FM) steels [7, 48-49, 78, 89-96]. However, more attention was devoted to the creep properties of these steels rather that the tensile flow properties; henceforth, this would explain the lack of the published research on the tensile flow properties of Grade 92 steel [93-96].

The creep-rupture curves at 600°C for different 9-12% Cr steels [i.e. 12Cr1MoV, 9Cr-1Mo (P9), modified 9Cr-1Mo (P91) and 9Cr-2W (P92)] were discussed in the work by Ennis *et al.* [97]. The results showed that the rupture stresses at short times for 12Cr1MoV were much lower than that for other steels, Figure 1.2. Also, the difference between P91 and P92 increased with time. Thus, 9Cr-2W steel (i.e. Grade 92) showed better creep-rupture strength than its previous generation steels (such as Grade 91).

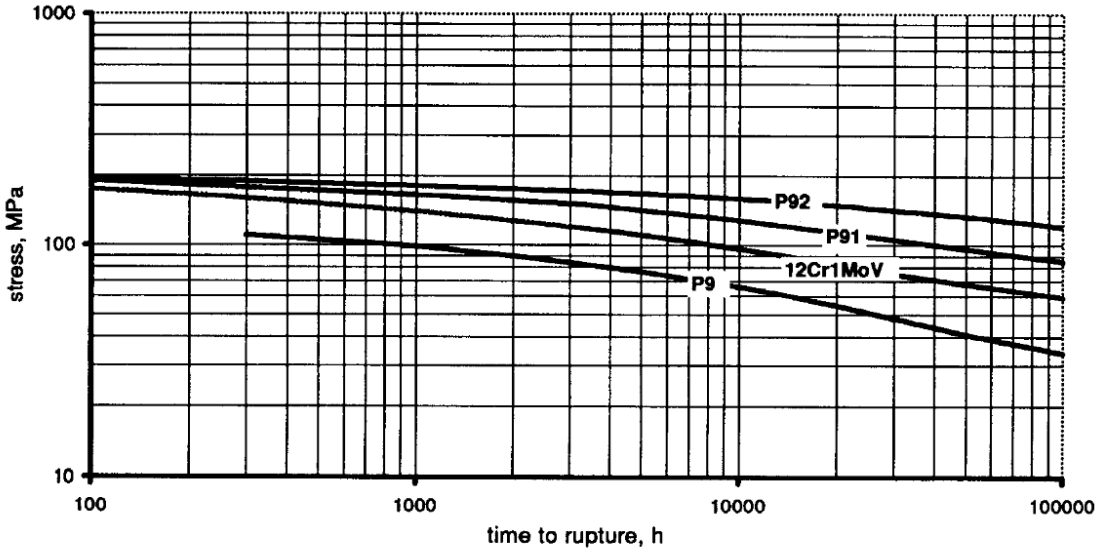

Figure 1.2. Creep-rupture curves for different 9-12% Cr steels at 600°C [97].

Even though the as-tempered microstructure has approximately the same dislocation density in these compared 9-12% Cr steels, the superior creep-rupture strength for Grade 92 among these other 9-12% Cr steels was attributed mainly to (i) the smaller average diameter of $M_{23}C_6$ and MX particles and (ii) the presence of the complex M(C,N) particles in Grade 92 steel only. For example, P9 steel which was accompanied with lower creep-rupture strength steel did not have any strong carbide former such as Nb or V; therefore, the as-tempered microstructure of P9 steel had the M23C6 precipitates after tempering which coarsen rapidly at temperatures around 600°C [6, 54, 19, 97]. On the other hand, the 12Cr1MoV has only V which promotes the formation of MX-type precipitates; but, the MX-type precipitates volume fraction is much less than that in P91 and P92. Lastly, the nominal composition of Grade 92 steel contains W and B and this would be the main difference between the remaining steels [1, 6, 97]. For instance, B stabilizes the morphology of $M_{23}C_6$ precipitates and lowers the coarsening rate in 9-12% Cr steels which enhances the creep behavior in Grade 92 steels [41-42]. Also, W enhances the high temperature strength and

promotes the carbide formation [22-26]. In brief, the better creep performance of Grade 92 is attributed to the slower recovery of the martensitic structure in Grade 92 steel. Thus, the dislocation density as a function of exposure time in a creep test at 600ºC showed slower recovery rate in Grade 92 steel [97]. Also, the smaller diameter of the strengthening particles and their slow coarsening rate made these particles more efficient in stabilizing the martensitic structure [1, 6, 97]. Similarly, Laves phase enhanced the mechanical properties of 9-12% Cr steels for a short time before the coarsening of this precipitate type occurs [1, 6, 97].

1.3.3. Irradiation performance of 9-12% Cr steels

The ferritic-martensitic steels are being considered for the advanced reactor applications [1, 15]. For instance, steels such as Grade 91, HT9 and Grade 92 are considered as structural components as a result of their superior properties [15, 26]. Thus, 9-12% Cr steels possess good resistance to irradiation exposure and they have superior thermal properties [15, 26]. However, the irradiation performance of these steels has not been discussed widely; especially, the new generations of these steels for instance (third and fourth generation). In general, 9-12% Cr steels have high thermal conductivity and low thermal expansion, which make these alloys promising for the NGNP reactor concept [2]. As these steels become exposed to irradiation, irradiation-induced precipitates occur which influence the mechanical properties of these steels [1, 4]. Therefore, the evaluation of the irradiation induced damage is critical in order to assess their usage in advanced reactors [15, 26-27]. For instance, the irradiation induced microstructural changes such as the carbide/matrix interface under irradiation and the carbide fragmentation [15, 26-27].

The irradiation performance of 9-12% Cr steels was investigated in the work by Horsten *et al.* and the Grade 92 steel showed lower hardening than the other 9-12% Cr steels [98]. The work by Topbasi *et al.* [99] showed that Grade 92 steel had no voids or irradiation induced precipitates at low dpa which indicates the good irradiation performance. Generally, the agglomeration of vacancies promotes the void swelling and 9-12% Cr steels have shown low swelling rate compared to conventional steels, Figure 1.3 [2, 98-99]. For instance, two steels of 9-12% Cr steels (HT9 and P91) developed less than 2% swelling when irradiated up to 200 dpa at a 400°C [4, 100].

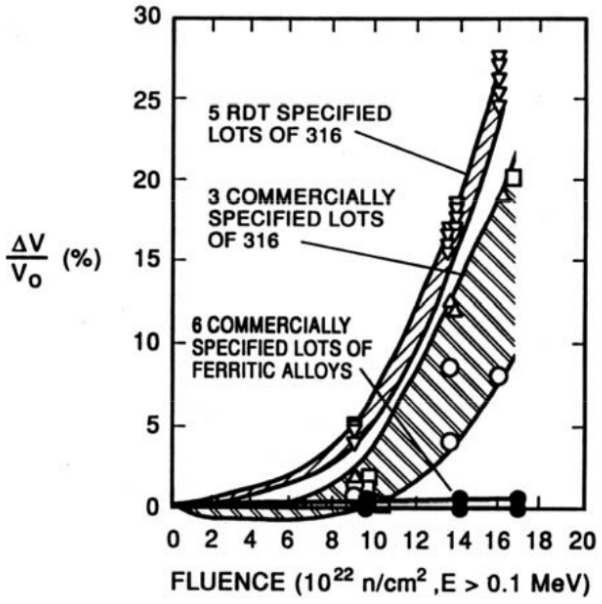

Figure 1.3. The swelling rate of ferritic-martensitic steels compared to those of the conventional 316 stainless steel at 80 dpa and 420°C [4].

On the other hand, the irradiation exposure affects the mechanical properties of these ferritic-martensitic steels and it greatly depends on temperature [1, 4]. For instance, the induced hardness in ferritic-martensitic steels increased as temperature increased up to around 450°C; finally, irradiation hardening saturates and no change occurs above 450°C, as

shown in Figures 1.4 and 1.5 [1, 4]. The ductility values in Fig. 1.5 highlights a couple of reasons. As hardening becomes more pronounced at the initial stage of irradiation due to (i) induced precipitates that form during the displacement damage and (ii) the higher density of dislocation loops and tangles, the ductility deteriorates before the irradiation hardening saturation occurs at 450°C [1, 98-101]. Subsequently at higher temperatures, ductility increases as a result of the microstructure evolution at that high temperature such as the coarsening of strengthening particles and the recovery of dislocation networks [98-101]. Hereafter, ductility can be enhanced as irradiation contributes to this microstructure evolution via enhancing the precipitate redistribution and diffusion [98-101]. So, Grade 92 steel has the potential to be employed in the advanced reactors for both in-core and out-of-core applications [15, 16].

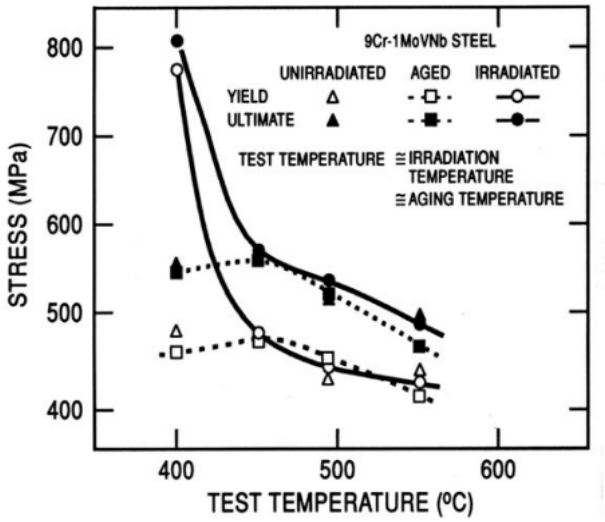

Figure 1.4. The influence of irradiation on the mechanical properties of Grade 91 steel irradiated at 9 dpa [4]

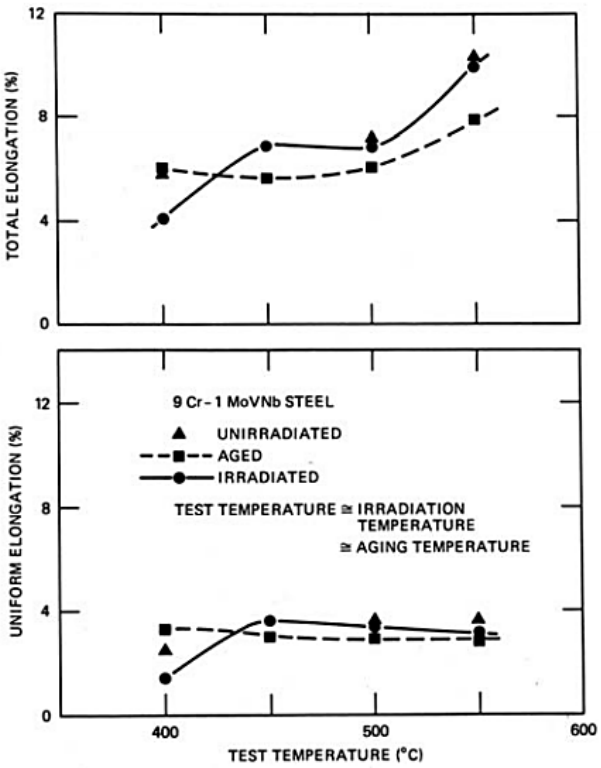

Figure 1.5. The influence of irradiation on the ductility of Grade 91 steel irradiated at 9 dpa [4].

References

[1] R. L. Klueh, R. Donald, R. Harries, High Chromium Ferritic and Martensitic Steels for Nuclear Applications, W. Conshohocken, PA, 2001.

[2] I. Charit, K.L. Murty, JOM 62 (9) (2010) 67–74.

[3] P. Ampornrat, G. Gupta, G.S. Was, J. Nucl. Mater. 395 (2009) 30-36.

[4] R.L. Klueh, A.T. Nelson, J. Nucl. Mater. 371 (2007) 37-52.

[5] L.J. Milovic, T. Vuherer, I. Blacic, M. Vrhovac, M. Stankovic, Mater. Des. 34 (2012) 566–575.

[6] P.J. Ennis, A. Zielinska-Lipiec, O. Wachter, A. Czyrska-Filemonowicz, Acta Mater. 45 (1997) 4901-4907.

[7] P.J. Ennis, A. Czyrska-Filemonowicz, Sadhana 28 (2003) 709-730.

[8] M. Carsi, F. Penalba, I. Rieiro, O.A. Ruano, Inter. J. Mater Res. 102 (2011) 1378-1383.

[9] E. I. Samuel, B. K. Choudhary, D.P. Rao Palaparti, M.D. Mathew, Procedia Eng. 55 (2013) 64-69.

[10] R.L. Klueh, Int. Mater. Rev. 50 (2005) 287-310.

[11] F. Masuyama, Int. J. Pres. Ves. Pip. 84 (2007) 53-61.

[12] Y. Kadoya, T. Goto, S. Date, T. Yamauchi, T. Saida, and T. Sada, ISIJ Int. 30 (1990) 854-861.

[13] K. Kimura, Y. Toda, H. Kushima, K. Sawada, Int. J. Pres. Ves. Pip. 87 (2010) 282-288.

[14] K. Sawada, K. Kubo, F. Abe, Mater. Sci. Eng. 319 (2001) 784-787.

[15] C. Topbasi, A. Motta, M. Kirk, J. Nucl. Mater. 425 (2012) 48-53.

[16] M. Yurechko, C. Schroer, A. Skrypnik, O. Wedemeyer, J. Konys, J. Nucl. Mater. 432 (2013) 78-86.

[17] L. Cipolla. H. K. Danilesen. D. Venditti, P.E. Di Nunzio, J. Hald, M. A. J. Somers, Acta Mater. 58 (2010) 669-679.

[18] H. K. Danielsen, J. Hald, Comput. Coupling Phase Diagrams Thermochem., 31 (2007) 505-514.

[19] P.J. Ennis, Y Wouters, W. J. Quadakker, J. Nutting (Eds.), Proc. Advanced heat resistant steels for power generation, San Sebastian, Spain (1998), pp. 457-467.

[20] F. Abe, S. Nakazawa, Mat. Sci. & Tech. 8 (1992) 1063-1069.

[21] A. Golpayergani, H.-O. Andren, H. K. Danielsen, J. Hald, ,Mater. Sci. Eng. A 489 (2008) 310-318.

[22] V. Knezevic, J. Balun, G. Sauthoff, G. Inden, A. Schneider, Mater. Sci. Eng. A 477 (2008) 334-343.

[23] U. E. Klotz, C. Solenthaler, P. Uggowitzer, Mater. Sci. Eng. A 476 (2008) 186-194.

[24] F. Abe, Mater. Sci. Eng. A 387-389 (2004) 565-569.

[25] F. Abe, Mater. Sci. Eng. A 319-321 (2001) 770-773.

[26] K. Sawada, M Takeda, K. Murayama, R. Ishii, M. Yamada, Y. Nygae, R. Komine, Metall. Mater. Trans. A 267 (1999)19-25.

[27] F. Abe, T. Horiuchi, M. Taneike, K. Sawada, Mater. Sci. Eng. A 378 (2004) 299-303.

[28] R.G. Baker, J. Nutting, J. Iron Steel I. 192 (1959) 257-268.

[29] K. Miyata, Y. Sawaragi, ISIJ Int. 41 (2001) 281-289.

[30] U. E. Klotz, C. Solenthaler, P. Uggowitzer, Mater. Sci. Eng. A 476 (2008) 186-194.

[31] Y. Tsuchida, R. Yamaba, K. Tokuno, K. Hashimoto, T. Ogawa, T. Takeda, Internal report, Nippon steel Corporation (1990).

[32] K. Miyata, M. Igarashi, Y. Sawaragi, ISIJ Int. 39 (1999) 947-954.

[33] T. Onizawa, T. Wakai, M. Ando, K. Aoto, Nucl. Eng. Des. 232 (2008) 408-416.

[34] M. Taneike, F. Abe, and K. Sawada, Nature 424 (2003) 294-296.

[35] T. Fujita, J. Thermal Nuclear Power 42 (1991) 1485-1496.

[36] K. Hidaka, Y. Fukui, S. Nakamura, et al, “Development of heat resistant 12%CrWCoB steel rotor for USC power plant”, in: R. Viswanathan, J. Nutting (Eds.), Proc. Advanced heat resistant steels for power generation, San Sebastian, Spain (1998), pp. 418-429.

[37] K. Sakuraya, H. Okada, F. Abe, Energy Materials 1 (2006) 158-166.

[38] T. Fujita, N. Takahashi, T. Iron Steel Jpn. 18 (1979) 269-278.

[38] J. H. Woodhead, A. G. Quarrel, J. Iron Steel I. 203 (1965) 605-620.

[40] N. Fujitsuna, M. Igarashi, F. Abe, Key Eng. Mat. 171-174 (2000) 469-476.

[41] M. Hatteststrand, H.-O. Andren, Mater. Sci. Eng. A 270 (1999) 33-37.

[42] F. Abe, Curr. Opin. Solid St. M. 8 (2004) 305-311.

[43] R. W. Cahn, P. Haasen, Physical Metallurgy, fourth ed., New York, USA, 1983.

[44] Timken, Practical Data for Metallurgists, 14th Edition, 1999.

[45] D. Porter, K. E. Easterling, Phase Transformations in Metals and Alloys, London, UK, 1992.

[46] M. Taneike, F. Abe, and K. Sawada, Nature 424 (2003) 294-296.

[47] A. Czyrska-Filemonowicz, A. Lipiec, P.J. Ennis, Journal of Achievements in Materials and Manufacturing Engineering 19 (2006) 43-48.

[48] J.S. Lee, H.G. Armaki, K. Maruyama, T. Muraki, H. Asahi, Mater. Sci. Eng. A 428 (2006) 270-275.

[49] T. Shrestha, M. Basirat, I. Charit, G. P. Potirniche, K. K. Rink, U. Sahaym, J. Nucl. Mater. 423 (2012) 110–119.

[50] K. Kimura, K. Sawada, H. Kushima, K. Kubo, Int. J. Mater. Res. 99 (2008) 395-401.

[51] K. Kimura, Y. Toda, H. Kushima, K. Sawada, Int. J. Pres. Ves. Pip. 87 (2010) 282-288.

[52] K. Sawada, K. Kubo, F. Abe, Mater. Sci. Eng. 319 (2001) 784-787.

[53] F. Abe, Strengthening mechanisms in creep of advanced ferritic power plant steels based on creep deformation analysis, in: Y. Weng, D. Hand (Eds.). Advanced Steels: The

Recent Scenario in Steel Science and Technology, Metallurgical Industry, Beijing,2011, pp. 409-22.

[54] J. Hald, Int. J. Pres. Ves. Pip. 85 (2008) 30–37.

[55] V. Dudko, A. Belyakov, R. Kaibyshev, Mater. Sci. Forum 706-709 (2012) 841-846.

[56] K. Rodak, A. Hernas, A. Kielbus, Mater. Chem. Phys. 81 (2003) 483–485.

[57] V. Thomas Paul, S. Saroja, M Vijayalakshmi, J. Nucl. Mater. 378 (2008) 273-281.

[58] M. Hatteststrand, M. Schwing, H.-O. Andren, Mater. Sci. Eng. A 250 (1998) 27-36.

[59] M. Hatteststrand, H.-O. Andren, Micron 32 (2001) 789-797.

[60] J. Janovec, A. Vyrostkova, M. Svoboda, A. Kroupa, H. J Grabke, Metall. Mater. Trans. A 35A (2004) 751-759.

[61] D. A. Skobir, F. Vodopivec, S. Spaic, B. Markoli, Z. Metalkd. 95 (2004) 1020-1024.

[62] M. Taneike, K. Sawada, F. Abe, Metall. Mater. Trans. A 35A (2004) 1255-1262.

[63] A. Aghajani, F. Richter, C Somsen, S. G Fries, I. Steinbach, G. Eggeler, Scripta Mater. 61 (2009) 1068-1071.

[64] Panait C G, Bendick W, Fuchsmann A, *et al.* Inter. J. Press. V. Pip., 87 (2010) 326–335.

[65] L. Korcakova, J. Hald, Mater. Charact. 47 (2001) 111-117.

[66] D. H. Jack, K. H. Jack, Mater. Sci. Eng. A 11 (1973) 386-405.

[67] H. K. Danielsen, J. Hald, Energy Mater. 1 (2006) 49-57.

[68] K. Maruyama, K. Sawada, J. Koike, ISIJ Int. 41 (2001) 641-653.

[69] R. Abbaschian, R. E. Reed-Hill, Physical Metallurgy Principles, fourth ed., Van Nostrand, New Jersey (2008).

[70] R. C. Thomson, H. K. D. H. Bhadeshia, Metall. Trans. A 23 (1992) 1171-1179.

[71] F. Abe, T. U. Kern, R. Viswanathan, Creep Resistant Steels, first ed., CRC Press Cambridge, England 2008.

[72] K Kimura, H Kushima, F Abe, K Suzuki, S Kumai, A Satoh, Microstructural change and degradation behaviour of 9Cr-1Mo-V-Nb steel in the long term, in: A. Strang, W. M. Banks, R. D. Conroy, G. M. McColvin, J. C. Neal. S. Simpson (Eds.), Proc. 5th International Charles Parsons Turbine Conference, Cambridge, UK 2000, pp. 590–602.

[73] N. Ridley, S. Maropoulos, J. D. H. Paul, Mater. Sci. Tech. 10 (1994) 239-249.

[74] F. Abe, Metall. Mater. Trans. A 34 (2003) 913-925.

[75] F. Abe, S. Nakazawa, H. Araki, T. Noda, Metall. Trans. A 23 (1992) 469-477.

[76] S. Takeuchi, A. S. Argon, J. Mater. Sci. 11 (1976) 1542-1566.

[77] D. Rojas, J. Garcia, O. Prat, C. Carrasco, G. Sauthoff, A.R. Kaysser-Pyzalla, Mater. Sci. Eng. A 527 (2010) 3864-3876.

[78] V. Sklenicka, K. Kucharova, M. Svoboda, L. Kloc, J. Bursik, A. Kroupa, Mater. Charact. 51 (2003) 35-48.

[79] G. Eggeler, Acta Metall. 37 (1989) 3225-3234.

[80] P. W. Voorhees, J. Stat. Phys. 38 (1985) 231-252.

[81] A. Bladan, J. Mater. Sci. 37 (2002) 2171-2202.

[82] M. Y. Wey, T. Sakuma, T. Nishizawa, Trans. Jpn. Inst. Met. 22 (1981) 733-742.

[83] Aghajani A, Somsen C, Eggeler G. Acta Mate. 57(2009) 5093–5106.

[84] G. Eggeler, N. Nilsvang, and B. Ilschner, Steel Res. 58 (1987) 97-103.

[85] F. Abe, H. Araki, T. Noda, Mater. Sci. Tech. 6 (1990) 714-723.

[86] D. Rojas, J. Garcia, O. Prat, L. Agudo, C. Carrasco, G. Sauthoff, A.R. Kaysser-Pyzalla, Mater. Sci. Eng. A 528 (2011) 1372-1381.

[87] J. S. Dubey, H. Chilukuru, J.K. Chakravartty, M. Schwienheer, A. Scholz, W. Blum, Mater. Sci. Eng. A 406 (2005) 152-159.

[88] S. Jin, L. Guo, T. Li et al, Mater. Charact. 68 (2012) 63–70

M. Yoshizawaa, M. Igarashia, K. Moriguchia, A. Isedab, Mater. Sci. Eng. A 510-511 (2009) 162-168.

[89] L. Kloc, V. Sklenicka, Mater. Sci. Eng. 234 (1997) 962–965.

[90] B.K. Choudhary, E.I. Samuel, J. Nucl. Mater. 412 (2011) 82–89.

[91] S. Spigarelli, E. Cerri, P. Bianchi, E. Evangelista, Mater. Sci. Technol. 15 (1999) 1433–1440.

[92] B. Ule, A. Nagode, Mater. Sci. Technol. 23 (2007) 1367–1374.

[93] F. Penalba, X. Gomez, R. Allende, M. Carsi, O. Ruano, Mater. Sci. Forum, 638 (2010) 3128-3133.

[94] F. Dobes, K. Milicka, Metal Sci. 10 (1976) 382-384.

[95] B.K. Choudhary, K.B.S. Rao, S.L. Mannan, Trans. Indian Inst. Met. 52 (1999) 327-236.

[96] B.K. Choudhary, S. Saroja, K.B.S. Rao, S.L. Mannan, Metall. Mater. Trans., A30 (1999) 2825-2834.

[97] P. J. Ennis, A. Zielinska-Lipiec, A. Czyrska-Filemonowicz, Microstructural Stability of Creep Resistant Alloys for High Temperature Plant Applications, The Institute of Materials, London, 1998.

[98] M. Horsten, M. Osch, D.S. Gelles, M.L. Hamilton, in: M.L. Hamilton, A.S. Kumar, S.T. Rosinski, M.L. Grossbeck (Eds.), Effects of Irradiation on Materials: 19th International Symposium, ASTM STP 1366, American Society for Testing and Materials, 2000, p. 579.

[99] C. Topbasi, A. Motta, M. Kirk, J. Nucl. Mater. 425 (2012) 48-53.

[100] R.L. Klueh, J.J. Kai, D.J. Alexander, J. Nucl. Mater. 225 (1995) 175-186.

[101] R.L. Klueh, J.M. Vitek, J. Nucl. Mater. 182 (1991) 230-239.

CHAPTER 2: High Temperature Tensile Deformation Behavior of Grade 92 Steel

Sultan Alsagabi [a,b], Triratna Shrestha [a] and Indrajit Charit [a]

[a] Chemical and Materials Engineering, University of Idaho, Moscow, ID 83844-3024, USA

[b] Atomic Energy Research Institute, King Abdulaziz City for Science and Technology, Riyadh, Saudi Arabia

(*Reviewed by the Journal of Nuclear Materials*)

Abstract

Candidate structural materials for advanced reactors need to have superior high temperature strength and creep-rupture properties among other characteristics. The ferritic-martensitic Grade 92 steel (Fe-9Cr-2W-0.5Mo, wt.%) is considered such a candidate structural material. Tensile tests were performed at temperatures of 600, 650 and 700 °C in the strain rate range of 10^{-5} – 10^{-3} s^{-1}. After analyzing the tensile results using the Bird-Mukherjee-Dorn (BMD) equation, a stress exponent of about 9.5 and an activation energy of about 646 kJ/mol were obtained. In the light of high values of the stress exponent and activation energy, the threshold stress concept was used to elucidate the operating high temperature deformation mechanism. As a result of this modification, the true activation energy and stress exponent of the high temperature deformation in Grade 92 steel were found to be about 245 kJ/mol and 5, respectively. Thus, the dominant high temperature deformation mechanism was identified as the high temperature climb of edge dislocations and the appropriate constitutive equation was developed.

Keywords: 9Cr-2W steel; tensile testing; activation energy; threshold stress

2.1. Introduction

Gen-IV nuclear reactors are designed to operate at higher temperatures and for longer time periods [1]. Hence, the candidate structural materials for such applications are required to have properties that enable them to perform satisfactorily under harsh reactor conditions [2]. There are many ferritic-martensitic (FM) steels such as Grade 91, Grade 92 and HT9, which have attracted considerable interest. Interestingly, the development of these alloys was first spearheaded for their use in the structural applications of fossil-fuel-fired power plants.

Grade 92 steel is considered a modified version of the Grade 91 steel [3]. The nominal chemical composition of this steel is Fe-9Cr-0.5Mo-1.8W-VNb (in wt.%), and is similar in composition to NF616 steel [4]. Grade 92 steel is a promising FM steel. This steel, in general, possesses excellent properties [3-5]. For instance, it has high creep and tensile strength, low thermal expansion coefficient and high thermal conductivity [5-6]. The following microstructural features exert influence on the high temperature deformation properties of these materials: fine, uniformly dispersed carbides and/or carbonitrides which pin the grain boundaries and lead to the obstruction of the dislocation movement [7]; the dislocation density within the martensitic laths (characterized by the narrow mesh of substructures); and solid solution strengthening of the matrix by elements such as W and other alloying elements [3-7]. In Grade 92 steel, the fine/stable carbides and carbonitrides are formed due to the presence of strong carbide/carbonitride formers like Nb and V [4-6].

The mechanical properties of FM steels such as Grade 92 steel have been investigated for better understanding [1,4,8-21]. However, more attention was devoted to understanding the creep properties of these alloys rather than the tensile flow properties. This explains the

lack of published literature on the flow properties of Grade 92 steel and elucidation of the high temperature deformation mechanisms [8-11]. Hence, the focus of the present study was on understanding the high temperature tensile deformation behavior of Grade 92 steel. In this work, the tensile flow behavior of Grade 92 steel is analyzed at different temperatures (600 to 700°C) and strain rates (10^{-5} to 10^{-3} s^{-1}). Furthermore, the dominant high temperature deformation mechanism was identified using the Bird–Mukherjee–Dorn equation with the help of threshold stress compensation.

2.2. Experimental procedure

The Grade 92 steel used in this study was procured from the Tianjin Tiangang Weiye Steel Co., China. The steel was received in the form of cylindrical bars with a diameter of 14 mm. The as-received alloy was in F92 condition in accordance with the ASTM A182 standard. According to the standard, the material was normalized at a temperature between 1040-1080°C. Then, tempering was conducted at a temperature between 730-800°C. The nominal composition of the as-received alloy is shown in Table 2.1.

The tensile specimens were prepared with a gage length of 25.4 mm and a gage diameter of 6.4 mm. An Instron universal tester (model no. 5982) was used to carry out the tensile tests. The test temperatures were maintained within ±3 °C of the set point in a three-zone furnace (model no. SF-16 2230) and the soaking time was kept at 50 min.

Standard metallographic procedures were followed in this work to reveal the relevant microstructure. After grinding, polishing was performed down to 3, 1 and 0.5 μm finish using water-based polycrystalline diamond suspensions. Afterwards, etching was completed using the Marble etchant consisting of 50 ml hydrochloric acid, 10 g of copper sulfate and

50 ml of distilled water. Next, an OLYMPUS PMG3 optical microscope was employed for examining the microstructure of the Grade 92 steel.

Table 2.1. The chemical composition of the as-received Grade 92 steel.

Element	**Composition (wt%)**
C	0.09
Mn	0.42
Si	0.34
P	0.015
S	0.001
Cr	8.68
Mo	0.55
V	0.19
N	0.045
Ni	0.12
Al	0.02
Nb	0.079
W	1.66
B	0.003
Fe	Bal .

TEM samples (disks with 3 mm diameter) were punched out from 60 μm thick foils and subsequently jet polished using a Fischione twin-jet polisher. Jet polishing was conducted in a low temperature environment using a dry ice bath (around -40°C) using a solution of 20 vol.% nitric acid and 80 vol.% methanol. Finally, TEM imaging was conducted using a JEOL JEM-2010 TEM microscope operated at an accelerating voltage of 200 kV.

2.3. Results and discussion

2.3.1. Microstructural characteristics

The microstructure of the as-received Grade 92 steel shows a normalized/tempered martensitic microstructure as shown in Figure 2.1. Figure 2.1a shows an optical micrograph of the overall tempered martensitic structure of the as-received alloy. The lath

microstructure of the Grade 92 alloy is evident in the TEM image presented in Figure 2.1b. During tempering, various particles precipitated on the prior austenite grain boundaries (PAGB), lath boundaries and within the lath microstructure such as the chromium-rich precipitates ($M_{23}C_6$) [3, 12]. Other precipitates were also reported in Grade 92 steel such as the fine-MX precipitates. The stability of these strengthening precipitates at high temperatures was found to be instrumental in enhancing the elevated temperature creep strength in Grade 92 steel [12-13].

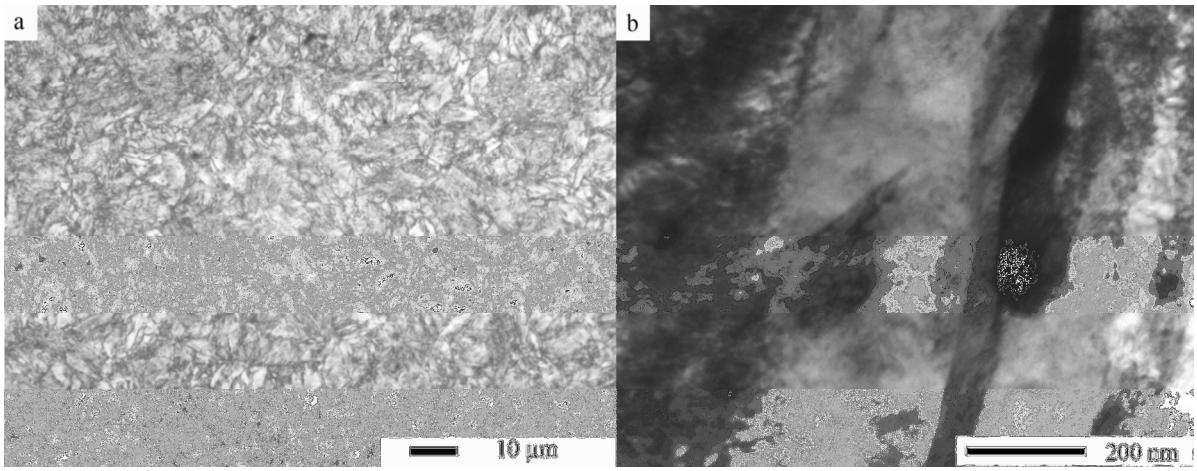

Figure 2.1. The microstructure of the as-received Grade 92 steel: (a) an optical micrograph shows the normalized and tempered microstructure, and (b) a bright field TEM image showing the lath microstructure.

2.3.2. Tensile properties of Grade 92 steel at elevated temperatures

Figure 2.2 shows a representative engineering stress-strain curve for the as-received Grade 92 steel at room temperature and a strain rate of 10^{-3} s^{-1}. The yield strength (YS) and ultimate tensile strength (UTS) were estimated to be 1063 and 1385 MPa, respectively. The tested alloy exhibited an elongation to fracture (ductility) of about 19%.

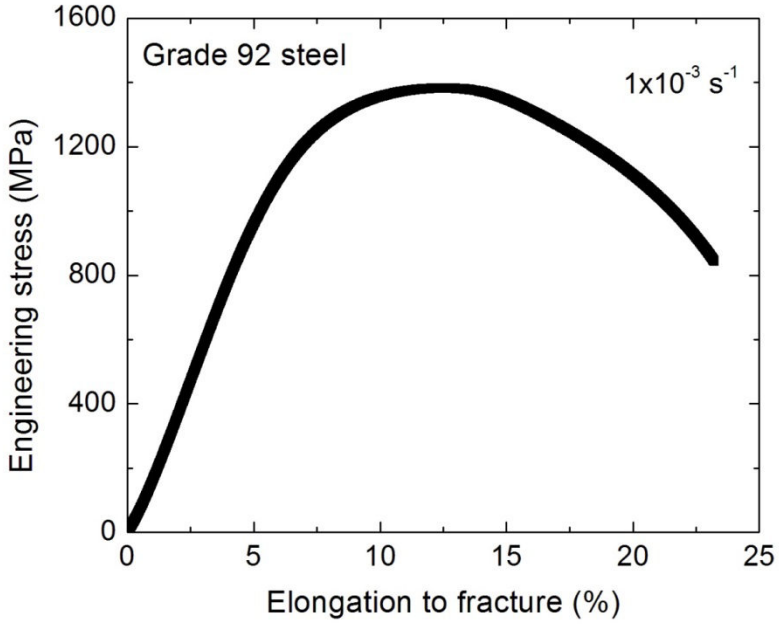

Figure 2.2. Engineering stress-strain curve for the as-received Grade 92 steel at room temperature and a strain rate of 10^{-3} s^{-1}.

Grade 92 steel specimens were tested at different temperatures of 600, 650 and 700°C. For each temperature, different strain rates of 1×10^{-3}, 3×10^{-4}, 1×10^{-4}, 3×10^{-5} and 1×10^{-5} s^{-1} were employed. The highest YS and UTS were obtained at the highest strain rate and the lowest temperature (10^{-3} s^{-1} and 600°C, respectively) among the test conditions. The strength of the Grade 92 steel decreased with decreasing strain rate for all test temperatures. Also, the strength dropped with increasing test temperatures. Therefore, the minimum strength was associated with the lowest strain rate and the highest temperature (10^{-5} s^{-1} and 700°C, respectively) as shown in Figure 2.3a-c. Clearly, the strength decreased as the temperature increased and the strain rate decreased. For instance, at 600°C the yield strength dropped from 820 MPa to 546 MPa as the strain rate decreased from 10^{-3} s^{-1} to 10^{-5} s^{-1}. Likewise, for a constant strain rate, the strength deceased as the temperature increased. As the deformation temperature increases, the effect of precipitate strengthening weakened due to the thermal activation [14]. Moreover, according to Wang *et al.* and other researchers [14-16], the fast

diffusion at higher temperature (around 650°C) plays an important role in assisting dislocations passing over the existing precipitates. Also, the decreasing strength at elevated temperatures has been attributed to the subgrain coarsening and the reduction in dislocation density, Figure 2.4a-c show the TEM images of the deformed microstructure after tensile testing at 1×10^{-5} s^{-1} and different testing temperatures (600, 650 and 700°C) .

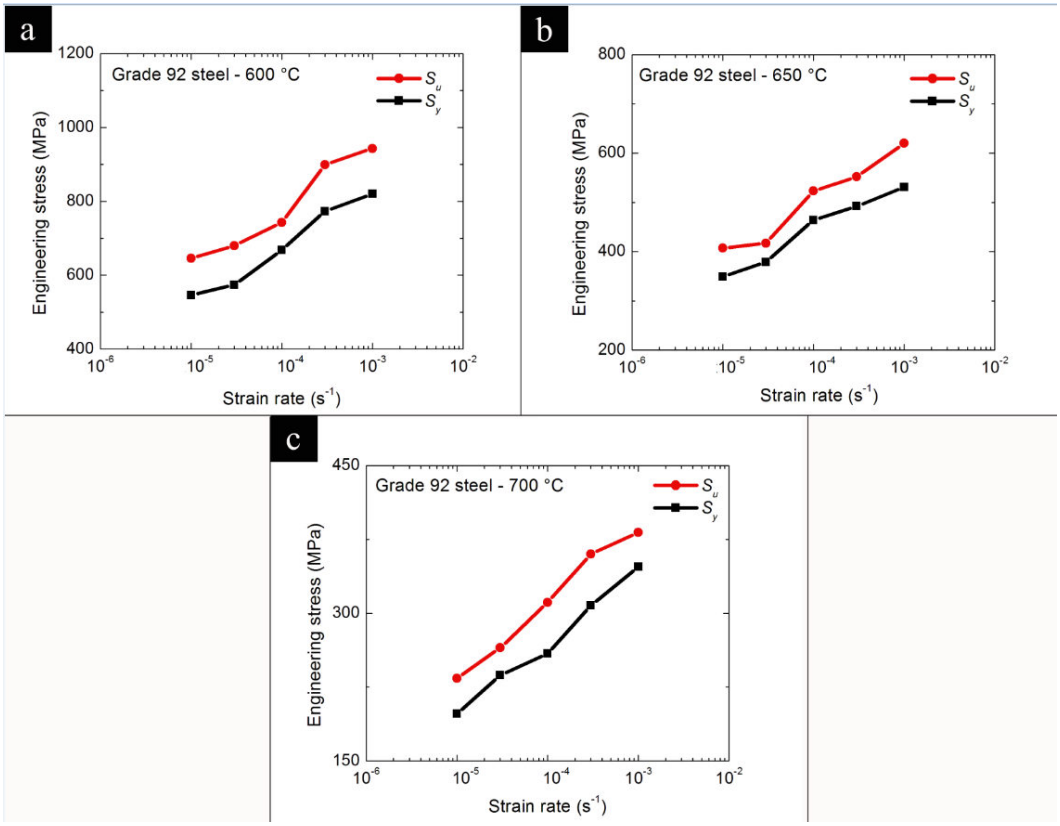

Figure 2.3. The variation of yield strength (*Sy*) and ultimate tensile strength (*Su*) of the Grade 92 steel as a function of strain rate at (a) 600°C, (b) 650°C, and (c) 700°C.

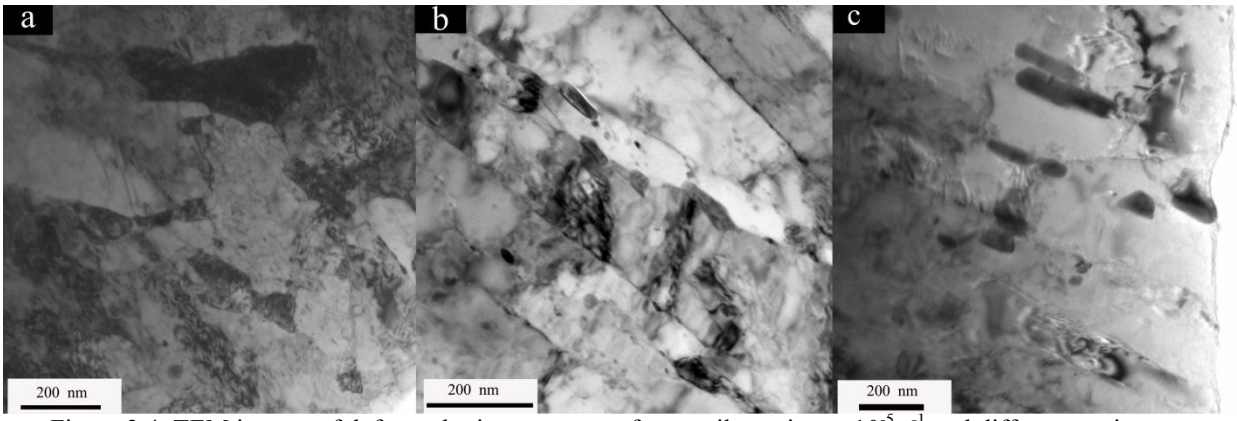

Figure 2.4. TEM images of deformed microstructure after tensile testing at 10^{-5} s^{-1} and different testing temperatures of a) 600°C, b) 650°C and 700°C.

The ductility values obtained at various testing temperatures and strain rates are listed in Table 2.2. The ductility at elevated temperatures was smaller than that at room temperature. For instance, the ductility of Grade 92 steel at room temperature was around 19% and ductility at the elevated testing temperatures never reached 19%; rather the closest was 18.8% at 700°C and 10^{-3} s^{-1}. So, the ductility of Grade 92 steel does not show a monotonic function of temperature within the test temperature range (600-700°C) studied. Likewise, similar behavior has been reported for ferritic-martensitic steels such as Grade 92 and Grade 91 steels [14, 21]. A new term (e_u /$e_{non\text{-}u}$) is used to understand the ductility of Grade 92 steel better. In this term, e_u is the percentage of the uniform plastic strain and the non-uniform plastic strain is denoted by $e_{non\text{-}u}$. At room temperature, e_u /$e_{non\text{-}u}$ was 0.46 indicating that the uniform plastic deformation was 46% of the non-uniform plastic deformation. However, the quantity (e_u/$e_{non\text{-}u}$) dropped significantly at elevated temperatures. For instance, e_u/$e_{non\text{-}u}$ remained below 0.1 at elevated temperatures (except for one test condition, 600°C and 1×10^{-3} s^{-1}), indicating that the uniform plastic deformation (e_u) was less than 10% of the non-uniform plastic deformation ($e_{non\text{-}u}$) in almost all cases.

From Table 2.2, the strain rate appears to have a relation with the quantity e_u/$e_{non\text{-}u}$. For example, at a constant strain rate (3×10^{-4} s^{-1}) the quantity e_u/$e_{non\text{-}u}$ decreases as the

temperature increases (0.09 for 600°C, 0.07 for 650°C and 0.05 for 700°C). This would suggest that the percentage of the uniform plastic deformation to the non-uniform plastic deformation decreases as the temperature increases for a constant strain rate. However, the trend was continuous until reaching the slowest strain rate (1×10^{-5} s^{-1}) when $e_u/e_{non\text{-}u}$ became independent of temperature (0.07 for 600, 650 and 700°C).

Table 2.2. The measured ductility of Grade 92 steel at elevated temperatures and strain rates in terms of elongation and reduction of area.

Test Conditions	**Elongation (%)**	**Uniform plastic strain (e_u)**	**Non-uniform plastic strain ($e_{non\text{-}u}$)**	$e_u/e_{non\text{-}u}$	**Reduction of Area (%)**
600°C and 1×10^{-3} s^{-1}	13.9	1.60	12.30	0.13	56.3
600°C and 3×10^{-4} s^{-1}	13.1	1.10	12.00	0.09	54.1
600°C and 1×10^{-4} s^{-1}	15.3	0.90	14.40	0.06	62.3
600°C and 3×10^{-5} s^{-1}	15.0	0.90	14.10	0.06	63.6
600°C and 1×10^{-5} s^{-1}	12.4	0.80	11.60	0.07	54.1
650°C and 1×10^{-3} s^{-1}	16.0	0.90	15.10	0.06	64.2
650°C and 3×10^{-4} s^{-1}	16.3	1.00	15.30	0.07	66.0
650°C and 1×10^{-4} s^{-1}	15.3	0.90	14.40	0.06	67.9
650°C and 3×10^{-5} s^{-1}	17.4	0.90	16.50	0.05	67.9
650°C and 1×10^{-5} s^{-1}	13.6	0.90	12.70	0.07	56.3
700°C and 1×10^{-3} s^{-1}	18.8	0.80	18.00	0.04	72.2
700°C and 3×10^{-4} s^{-1}	17.3	0.90	16.40	0.05	68.7
700°C and 1×10^{-4} s^{-1}	17.3	0.80	16.50	0.05	67.9
700°C and 3×10^{-5} s^{-1}	15.5	0.90	14.60	0.06	66.0
700°C and 1×10^{-5} s^{-1}	12.8	0.80	12.00	0.07	54.1

2.3.3. Tensile flow mechanism in Grade 92 steel

In order to analyze the high temperature flow behavior of Grade 92 steel, true stress-strain curves were constructed for all the tensile test conditions. A representative set of true stress-strain curves at 700 °C for different strain rates is shown in Figure 2.4. In the tensile flow curves such as shown in Figure 2.5, a long softening stage was noted. This behavior has also been reported by Wang *et al.* [14] and Giroux *et al.* [21] in Grade 92 steel. Albeit the softening behavior is not completely understood in FM steels, it is generally attributed to the free dislocation density reduction and subgrain size growth [22]. According to Giroux *et al.* [21], the long softening stage in Grade 92 steel was attributed to physical mechanisms such as the subgrain size evolution and diffused necking [21]. On the other hand, Wang *et al.* [14] suggested that the operation of two mechanisms: (1) the mobile dislocation annihilation mechanism and (2) the grain boundary annihilation mechanism lead to a long softening stage in Grade 92 steels.

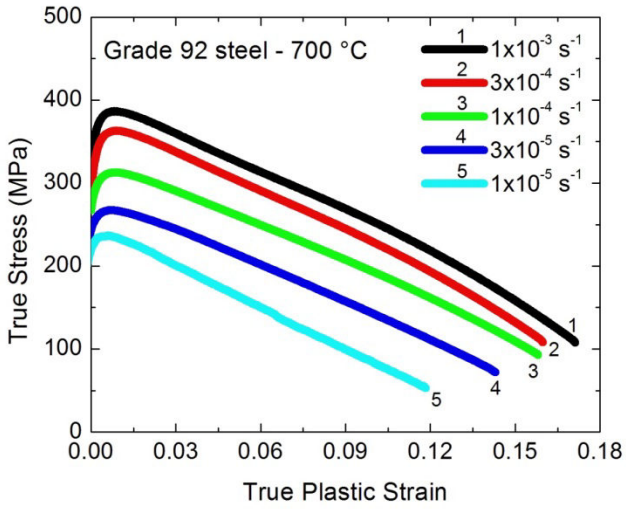

Figure 2.5. True stress-strain curves of Grade 92 steel as a function of strain rates at 700°C.

In the initial analysis of the high temperature deformation data, the stress exponent and activation energy was calculated using the Arrhenius type equation [23]:

$$\dot{\varepsilon}.exp\left(\frac{Q}{R.T}\right) = A\,\sigma^{n} \qquad (2.1)$$

where A is a constant, $\dot{\varepsilon}$ the strain rate, σ the true stress, R the universal gas constant, T the temperature in K, Q the apparent activation energy and n the stress exponent.

In order to estimate the stress exponent (n), the strain rate sensitivity (m) is first calculated. The stress exponent is defined as the reciprocal of the strain rate sensitivity (i.e. $n = 1/m$). The strain rate sensitivity (m) helps in identifying the appropriate high temperature flow deformation mechanism (i.e., $m = \frac{\delta \log \sigma}{\delta \log \dot{\varepsilon}}$) [5, 24-25]. Ideally, a larger m value indicates a larger ductility and higher necking resistance. For analyzing the deformation data, flow stress ($\sigma_{\varepsilon=0.01}$) data at a true plastic strain of 0.01 from the true stress-strain curves were taken in order to estimate the deformation parameters. The m values were estimated by plotting $\sigma_{\varepsilon=0.01}$ versus $\dot{\varepsilon}$ data on a double logarithmic plot as shown in Figure 2.6, and taking the slopes of the fitted straight lines at different temperatures as the 'm' values. The stress exponent (n) was estimated as the average of the reciprocal of the m values. Thus, the n_{avg} was calculated to be about 9.5.

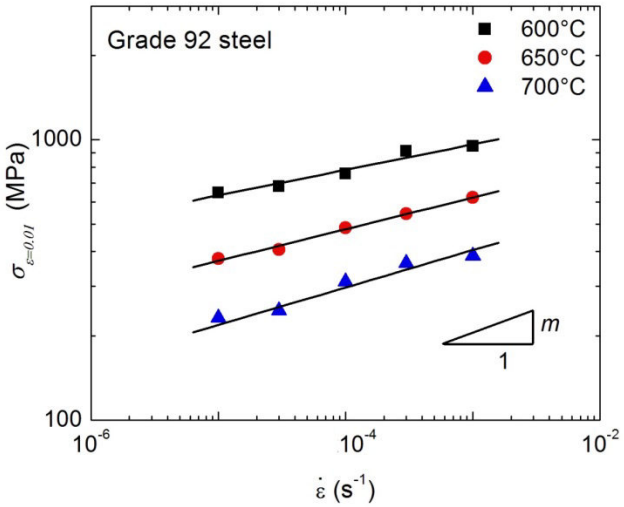

Figure 2.6. The relationship between the flow stress versus strain rate on a log-log scale.

Eqn. 2.1 can be rewritten in the following form in order to estimate the activation energy for elevated temperature deformation:

$$\ln(\sigma) = \frac{ln\dot{\varepsilon} - \ln A}{n} + \frac{Q}{R.n} \cdot \frac{1}{T} \qquad (2.2)$$

Thus, the activation energy is estimated by plotting $\sigma_{\varepsilon=0.01}$ versus $1/T$ as a semi-logarithmic plot as shown in Figure 2.7. According to Eqn. 2.2, the slope of the fitted line signifies the term, $\frac{Q}{R.n_{avg}}$. The flow stresses used in this analysis were taken at strain rates of 10^{-3}, 10^{-4} and 10^{-5} s^{-1}. Therefore, the average of the activation energy was calculated to be about 645±33 kJ/mol. The estimated activation energy for elevated temperature deformation is found to be much higher than the activation energy of self-diffusion in α-iron (250 kJ/mol) [1]. However, the activation energy and stress exponent values are generally found higher for the high temperature deformation of the particle-hardened alloys such as Grade 92 steel and do not provide information on the intrinsic deformation mechanism. Table 2.3 summarizes these deformation parameters obtained in other studies [1, 7, 25-26]. For instance, the presence of strengthening precipitates inhibits the dislocation movement, which

explains the high stress exponents of particle hardened alloys [1, 3]. Thus, the higher values of the activation energy and stress exponent make them only apparent in nature. Table 2.4 lists the expected stress exponents and activation energy values for different high temperature deformation mechanisms. For instance, the deformation mechanism is identified as the viscous glide deformation when n = 3 and the activation energy is close to that of the solute diffusion; however, when n = 4-6, the dislocation climb becomes the rate-controlling mechanism with an activation energy close to that of the lattice self-diffusion [27-29]. So, to rationalize the observed deformation behavior of Grade 92, the true stress exponent and activation energy of high temperature deformation will be evaluated using the threshold stress concept as applied to the modified Bird–Mukherjee–Dorn (BMD) equation [1-3].

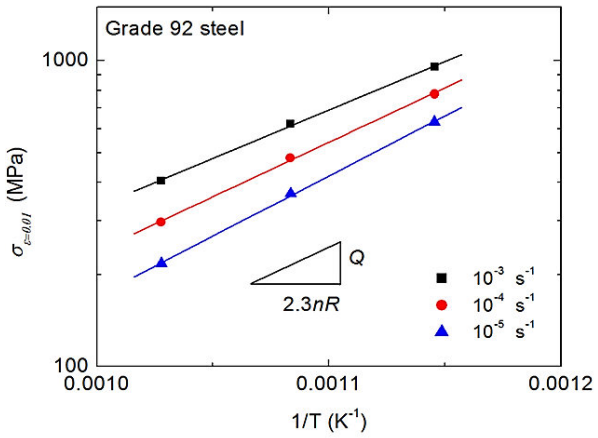

Figure 2.7. The relationship between the true stress value and the reciprocal of the temperatures according to the Arrhenius type equation.

Table 2.3. The estimated activation energy and stress exponent for different ferritic-martensitic steels.

Alloy	Activation energy (kJ/mol)	Stress exponent	Reference
Grade 92 (F92)	646	9.5	Present study
P92	390	-	[5]
T91	680	-	[7]
P92	437	6.6	[24]
Grade 91	792	10-17	[25]

Table 2.4. Parametric dependencies of different deformation mechanisms [1].

Mechanism	***D***	***n***	***p***
Viscous Glide	Solute Diffusion	3	0
Climb of Edge Dislocations	Lattice Diffusion	4-6	0
Grain Boundary Sliding	Grain Boundary Diffusion	2	2
Low Temperature Climb	Dislocation Core Diffusion	7	0
Harper-Dorn	Lattice Diffusion	1	0
Nabarro–Herring	Lattice Diffusion	1	2
Coble	Grain Boundary Diffusion	1	3

2.3.4. Application of the threshold stress approach

The elevated temperature deformation mechanism, as a thermally activated diffusion-assisted deformation process, can be described by the Bird–Mukherjee–Dorn (BMD) equation [1]. The BMD equation is described as:

$$\frac{\dot{\varepsilon} kT}{DEb} = A\left(\frac{\sigma}{E}\right)^n \left(\frac{b}{d}\right)^p \tag{2.3}$$

where A is a constant, $\dot{\varepsilon}$ the strain rate, k the Boltzmann constant, T the temperature in K, E the modulus of elasticity, b the Burgers vector, σ the true stress, n is stress exponent, d the grain diameter, p the inverse grain size exponent and D is the diffusivity parameter which is described by:

$$D = D_0 \exp(-\frac{Q}{RT}) \tag{2.4}$$

where D_o is defined as the frequency factor, Q the appropriate activation energy and R the universal gas constant.

In general, the BMD equation can be useful in identifying the rate-controlling deformation mechanism. Incorporation of the threshold stress concept can rationalize the operating deformation mechanism. The threshold stress is generally defined as the stress below which no deformation takes place following that specific mechanism. The modified BMD equation can be expressed as [1]

$$\frac{\dot{\varepsilon}kT}{DEb} = A'\left(\frac{\sigma-\sigma_{th}}{E}\right)^{n}\left(\frac{b}{d}\right)^{p} \quad (2.5)$$

where σ_{th} is the threshold stress and the term $(\sigma - \sigma_{th})$ quantifies the effective stress responsible for deformation rather than the applied stress [1, 27]. In this study, threshold stresses at different temperatures were estimated following the extrapolation method as discussed elsewhere [1, 28-29]. In this method, a set of stress exponents are assumed from 2 to 7 and corresponding threshold stresses are calculated using the $\dot{\varepsilon}^{1/n}$ data plotted against $\sigma_{\varepsilon=0.01}$. Following the calculation of threshold stresses, the fitting correlation coefficients and activation energy were analyzed. The most appropriate and consistent stress exponent is identified as the true stress exponent. The corresponding threshold stresses are then used to calculate the true activation energy of the high temperature deformation. The correlation coefficient was more than 0.95 for all conditions; however, the activation energy was also estimated and it must correlate with the relevant deformation mechanism depending on the chosen *n* value.

Table 2.5 lists the correlation coefficients and calculated activation energy for different *n* values (2-7). For *n* = 2, the threshold stress at 600°C was too high (621 MPa) and the grain boundary sliding was not a dominant mechanism given the type of microstructure of Grade 92 steel. Therefore, the assumption was excluded from further consideration. For *n* = 7, the correlation coefficient values were higher than 0.97 and the average stress exponent was estimated to be 7.3±0.02. However, the calculated activation energy was estimated to be about 354 kJ/mol and this activation energy is higher than that of the lattice self-diffusion in alpha-iron, and is considerably higher than that of the dislocation core diffusion (125-175 kJ/mol). The low temperature climb mechanism requires an activation energy that is close to that of the dislocation core diffusion as listed in Table 2.4. Since that is not the case here, the

assumption of n = 7 was excluded. Looking at the remaining assumptions, the stress exponent of 5 and 6 were mainly considered because (1) the correlation coefficient was consistently high (> 0.97), (2) the estimated average stress exponent aligned well with the assumed stress exponent, and (3) the estimated activation energy is consistent with that of the lattice self-diffusion in α-Fe. Here representative plots for calculation of the threshold stress and activation energy for n = 5 are shown in Figure 2.8a and b, respectively.

Table 2.5. Various results of the threshold stress analysis of Grade 92 steel.

Assumed stress exponent *n*	**Temp. (°C)**	**Threshold stress (MPa)**	**Correlation coefficient**	**Avg. stress exponent**	**Activation energy (kJ/mol)**
2	600	621	-	-	-
	650	371	-		
	700	228	-		
3	600	551	0.96	3.0±0.3	132.3±7.5
	650	318	0.99		
	700	183	0.95		
4	600	469	0.97	4.2±0.4	211.8±13.2
	650	258	0.99		
	700	151	0.96		
5	600	401	0.97	5.1±0.4	245.1±10
	650	208	0.99		
	700	111	0.97		
6	600	331	0.97	6.4±0.6	291.5±17.2
	650	153	0.99		
	700	74	0.97		
7	600	253	0.97	7.4±0.9	354.2±13
	650	105	0.99		
	700	38	0.98		

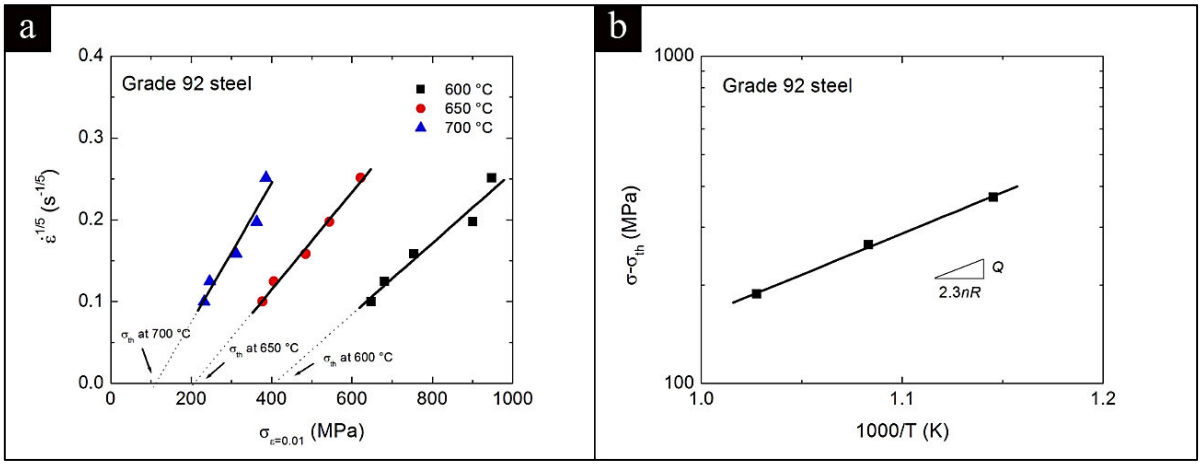

Figure 2.8. The calculation of (a) the threshold stresses through the linear extrapolation method and (b) the activation energy for high temperature deformation for n=5.

For n = 5 and 6, the high temperature climb of edge dislocations is the dominant deformation mechanism, according to Table 2.4. For the high temperature climb of edge dislocations, the inverse grain size exponent equals zero (i.e. p = 0). Hence, Eqn. 2.5 can be written as:

$$\frac{\dot{\varepsilon}kT}{DEb} = A'\left(\frac{\sigma-\sigma_{th}}{E}\right)^{n} \tag{2.6}$$

The $(\frac{\dot{\varepsilon}kT}{DEb})$ data were plotted against the normalized effective stress $\left(\frac{\sigma-\sigma_{th}}{E}\right)$ as shown in Figure 2.9. It should be noted that for n = 5 the activation energy was 245.1 kJ/mol; but for n = 6, Q = 291.5 kJ/mol, as noted in Table 2.5. As a result, n = 5 was selected because of the better consistency of the activation energy and higher correlation coefficients. The relevant constitutive equation for the high temperature deformation of the Grade 92 steel studied is given by:

$$\frac{\dot{\varepsilon}kT}{DEb} = (1.62 \pm 0.03)\times 10^{6}\left(\frac{\sigma-\sigma_{th}}{E}\right)^{5.2\pm0.2} \tag{2.7}$$

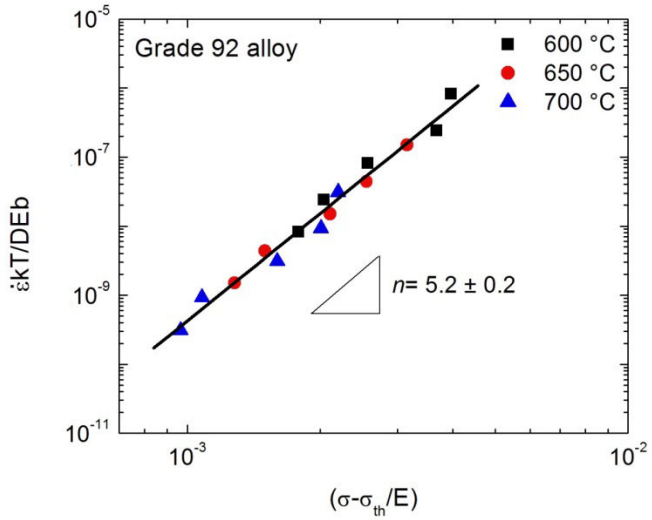

Figure 2.9. The diffusion compensated strain rate versus modulus compensated effective stress on a log–log plot.

2.4. Conclusion

The tensile testing at elevated temperatures in Grade 92 steels was performed in order to identify the high temperature deformation mechanism at different temperatures (600-700°C) and strain rates of 10^{-5}-10^{-3} s^{-1}. The following conclusions can be made:

1. The flow stress curves of Grade 92 steel at elevated temperatures and different strain rates were obtained and analyzed. Among all conditions, the lowest temperature (600°C) and the highest strain rate (10^{-3} s^{-1}) condition was associated with the highest strength. On the other hand, the minimum strength accompanied the highest temperature and lowest strain rate (700°C and 10^{-3} s^{-1}). In general, the elevated temperature strength of Grade 92 steel shows a gradual decrease as (1) temperature increases and (2) strain rate decreases.

2. The percentage of the uniform plastic deformation to the non-uniform plastic deformation ($e_u/e_{non\text{-}u}$) decreased as the test temperature increased. The long softening stage at elevated temperature tensile tests was pronounced. For particle hardened alloys such as

Grade 92, this behavior has been reported in literature and was attributed to the induced annihilation mechanisms exerted by the free dislocation density reduction and subgrain size growth.

3. The calculated activation energy and stress exponent for the as-received material were much higher than those of the conventional deformation mechanisms as a result of the presence of strengthening precipitates which inhibit the dislocation movement. Hence, the threshold concept was used.

4. The modified Bird–Mukherjee–Dorn (BMD) was used taking into consideration the threshold stress effect. The true stress exponent and activation energy of the high temperature deformation was found to be about 5 and 245 kJ/mol, respectively. As a result, the high temperature climb of edge dislocations was identified as the dominant deformation mechanism and the relevant constitutive equation was developed.

References

[1] T. Shrestha, M. Basirat, I. Charit, G. P. Potirniche, K. K. Rink, U. Sahaym, J. Nucl. Mater. 423 (2012) 110–119.

[2] L.J. Milovic, T. Vuherer, I. Blacic, M. Vrhovac, M. Stankovic, Mater. Des. 34 (2012) 566–575.

[3] P.J. Ennis, A. Zielinska-Lipiec, O. Wachter, A. Czyrska-Filemonowicz, Acta Mater. 45 (1997) 4901-4907.

[4] P.J. Ennis, A. Czyrska-Filemonowicz, Sadhana 28 (2003) 709-730.

[5] M. Carsi, F. Penalba, I. Rieiro, O.A. Ruano, Inter J. Mater Res. 102 (2011) 1378-1383.

[6] E. I. Samuel, B. K. Choudhary, D.P. Rao Palaparti, M.D. Mathew, Procedia Eng. 55 (2013) 64-69.

[7] S. Spigarelli, E. Cerri, P. Bianchi, E. Evangelista, Mater. Sci. Technol. 15 (1999) 1433–1440.

[8] F. Penalba, X. Gomez, R. Allende, M. Carsi, O. Ruano, Mater. Sci. Forum 638 (2010) 3128-3133.

[9] F. Dobes, K. Milicka, Metal Sci. 10 (1976) 382-384.

[10] B.K. Choudhary, K.B.S. Rao, S.L. Mannan, Trans. Ind. Inst. Met. 52 (1999) 327-236.

[11] B.K. Choudhary, S. Saroja, K.B.S. Rao, S.L. Mannan, Metall.Mater. Trans. A 30 (1999) 2825-2834.

[12] F. Abe, Strengthening mechanisms in creep of advanced ferritic power plants steels based on creep deformation analysis, in: Y. Weng, H. Dong, Y. Gan (Eds.), Advanced steels, Springer – Verlag Heidelberg and Metallurgical Industry Press, 2011, pp. 409-422.

[13] B.K. Choudhary, E. Isaac Samuel, G. Sainath, J. Christopher, M. D. Mathew, Metall. Mater. Trans. A 44 (2013) 4979-4992.

[14] L. Wang, M. Li, J. Almer, J. Nucl. Mater. 440 (2013) 81–90.

[15] M. Yoshizawa, M. Igarashi, K. Moriguchi, A. Iseda, H.G. Armaki, K. Maruyama, Mater. Sci. Eng. A 510–511 (2009) 162–168.

[16] J. Hald, Int. J. Pres. Ves. Pip. 85 (2008) 30–37.

[17] F. Abe, T. Horiuchi, M. Taneike, K. Sawada, Mater. Sci. Eng. A 378 (2004) 299–303.

[18] J. Zhao, D.M. Li, Y.Y. Fang, J. Press. Vess.-T ASME, 132 (2010) 064502-064506.

[19] K. Sawada, H. Kushima, K. Kimura, M. Tabuchi, ISIJ Inter. 47 (2007) 733–739.

[20] X. Guo, J. Gong, Y. Jiang, D. Rong, Mater. Sci. Eng. A 564 (2013) 199–205.

[21] P.F. Giroux, F. Dalle, M. Sauzay, J. Malaplate, B. Fournier,A.F. Gourgues-Lorenzon, Mater. Sci. Eng. A 527 (2010) 3984-3993.

[22] M.F. Giordanaa, P.-F. Girouxb, I. Alvarez-Armasa, M. Sauzayb, A. Armasa, T. Krumlc, Mater. Sci. Eng. A 550 (2012) 103–111.

[23] R. W. Armstrong, S.M. Walley, Inter. Mater. Rev. 53 (2008) 105-128.

[24] S. Ru-Xing, L. Zheng-Dong, J. Iron Steel Res Int. 18(7) (2011) 53-58.

[25] V. Sklenica, K. Kucharova, A. Dlouhy, J. Krejci, Proceedings of Conference on Materials for Advanced Power Engineering, Liege, Belgium (1994) p. 435.

[26] D.V.V. Satyanarayana, G. Malakondaiah, D.S. Sarma, Mater. Sci. Eng. A 323 (2002) 119–128.

[27] Y. Huang, T.G. Langdon, JOM 55 (2003) 15–20.

[28] R.S. Mishra, T.R. Bieler, A.K. Mukherjee, Acta Metall. Mater. 43 (1995) 877–891.

[29] I. Charit, K.L. Murty, J. Nucl. Mater. 374 (2008) 354–363.

CHAPTER 3: Microstructural Evolution in Deformed 9Cr-2W Steel at Elevated Temperatures

Sultan Alsagabi [a,b], Triratna Shrestha [a] and Indrajit Charit [a]

[a] Chemical and Materials Engineering, University of Idaho, Moscow, ID 83844-3024, USA

[b] Atomic Energy Research Institute, King Abdulaziz City for Science and Technology, Riyadh, Saudi Arabia

(*To be submitted to the Journal of Materials Science*)

Abstract

The 9Cr-2W ferritic-martensitic steel (namely Grade 92) was investigated through a set of tensile testing at room and elevated temperatures. The reduction in mechanical properties was investigated by studying the induced microstructural evolution at elevated temperatures. The microstructural evolution accelerated significantly under loading as temperature increased. For instance, the deformed microstructure at 600°C showed the early stages of nucleation of $M_{23}C_6$ precipitates under loading. These $M_{23}C_6$ precipitates showed more coarsening tendency; but, the MX-type (carbonitride) precipitates retained their size. As coarsening of $M_{23}C_6$ precipitates progressed at elevated temperatures, the strength gradually decreased as the solid solution strengthening deteriorated by removing W and Mo from the solid solution matrix.

Keywords: 9Cr-2W steel; tensile testing; fractography; microstructural evolution

3.1. Introduction

Producing more energy to address the growing energy demand is fraught with problems such as causing significant damage to the environment such as emission of harmful gases and particulates [1-5]. That is why efforts have been exerted to develop highly efficient, safe

energy-producing systems. The new generations of fission nuclear reactors were designed where new challenges have risen [1-2]. The new reactors are expected to perform under severe operating conditions; therefore, the mechanical and physical properties for the employed alloys have to meet these harsh service conditions [1-2]. Another factor was the desire of protecting the environment through decreasing the emission of carbon dioxide (CO_2) [3-5]. The ferritic-martensitic (FM) steels possess good mechanical properties to be considered as structural materials for these applications [3-5].

Ferritic-martensitic (FM) steels are being considered for the advanced energy system application [6-7]. For instance, they are considered as structural components as a result of their superior mechanical properties [7-8]. The FM steels have high temperature strength and creep-rupture properties [9-13]. Furthermore, they have low thermal expansion and high thermal conductivity [9-13]. The strength of FM steels is attributed to the fine/stable carbides and carbonitrides that form during tempering which pin the movement of dislocations; therefore, they enhance strength by delaying the onset of plastic deformation [7, 14]. At elevated temperatures, significant microstructural changes occur altering the mechanical behavior of steels [1, 9]. For instance, the dislocation sub-structure evolution, particle coarsening and new phase precipitation may deteriorate the mechanical performance [15-16]. Moreover, the microstructural evolution accelerates under loading [15-16].

Grade 92 steel (9Cr-2W) was introduced after Grade 91 steel (modified 9Cr-1Mo). The alloy design approach in developing Grade 92 steel included W enhancing the high temperature strength and helps in reducing the coarsening rate of the strengthening precipitates as well as imparting solid solution strengthening [8, 17]. It is necessary to understand the microstructural evolution at elevated temperatures for the investigated steel

thus the high temperature deformation mechanism in this class of steel has not been fully understood. For instance, partitioning the load between the several strengthening mechanisms will give insight on the role of each strengthening mechanism and its contribution to the overall strength. Also, more attention was devoted to investigate the microstructural evolution after long exposure hours (such as in creep); however, it is of interest to investigate the early stages of the microstructural evolution of these steels.

The aim of the current work is to investigate the associated microstructural evolution under loading in Grade 92 steel. Thus, tensile testing will be conducted at elevated temperatures and the microstructure of the deformed part of the specimens will be correlated to the non-deformed section at different temperatures and a particular strain rate. Also, the post-deformation fractography will be utilized to understand the fracture mechanism.

3.2. Experimental procedure

3.2.1. Material

The investigated steel was procured from the Tianjin Tiangang Weiye Steel Co. of China in the form of cylindrical bars with a diameter of 14 mm. The steel was normalized at a temperature between 1040-1080°C; then, it was tempered at a temperature between 730-800°C. Table 3.1 shows the nominal composition of the as-received steel.

Table 3.1. The chemical composition of the as-received Grade 92 steel.

Element	**Composition (wt%)**
C	0.09
Mn	0.42
Si	0.34
P	0.015
S	0.001

Cr	8.68
Mo	0.55
V	0.19
N	0.045
Ni	0.12
Al	0.02
Nb	0.079
W	1.66
B	0.003
Fe	Bal .

3.2.2. Tensile testing

Tensile testing was conducted using an Instron universal tester (model no. 5982) and tensile specimens were machined with a gage length of 25.4 mm and a gage diameter of 6.4 mm. The elevated temperature tensile testing was performed in a three-zone furnace (model no. SF-16 2230) and the soaking time was kept at 50 min. The tensile testing was conducted at different temperatures (600, 650 and 700°C) and strain rates of 1×10^{-5} s^{-1} and testing temperature was maintained within ± 3°C of the set point. As this work will investigate the microstructural evolution during the tensile testing, it is of interest to point out the testing time for each condition. The tensile testing periods for samples tested at 600, 650 and 700°C were 30100, 30200 and 30400 s, respectively.

3.2.3. Microstructural examination

The microstructure of the non-deformed condition was drawn from the grip section of the tensile specimen whereas the microstructure of the deformed condition was obtained from the gage length of the tensile specimen. An OLYMPUS PMG3 optical microscope was

employed to examine the relevant microstructures after performing standard metallographic procedures of grinding and polishing on the specimens. Thus, grinding was performed using silicon carbide grinding papers down to 1200 grit. Then polishing using water-based polycrystalline diamond suspensions was performed down to 3, 1 and 0.5 μm finish and samples etched using Marble etchant (50 ml of distilled water, 10 g of copper sulfate and 50 ml hydrochloric acid).

The TEM sample preparation was performed after punching out 3 mm diameter disks from 60 μm thick foils of the investigated samples. Thereafter, a Fischione twin-jet polisher was used to jet-polish samples using a solution of 80 vol.% methanol and 20 vol.% nitric acid in low temperature environment (~-45°C). A TF30-FEG Transmission Electron Microscope with STEM mode that operates at an accelerating voltage of 300 kV was used for TEM imaging in this work. Particles were identified using the energy dispersive X-ray spectroscopy (EDS) technique via STEM mode on TEM. The dislocation density of investigated samples was estimated while samples were oriented in a two-beam condition; also, the electron energy loss spectrum (EELS) technique was applied to estimate the sample thickness. After that, the dislocation density by intercept method was used to estimate the dislocation density from 2-3 microstructures of known thicknesses [18]. Finally, FEGSEM ZEISS Supra-35 Scanning Electron Microscope (SEM) was used to conduct the fractography part of this work at an accelerating voltage of 10-20 kV.

3.3. Results and discussion

3.3.1. Tensile properties of the investigated samples

The tensile testing in Grade 92 steel was evaluated through a set of tensile testing using a low strain rate of 10^{-5} s^{-1} to allow sufficient time in order to investigate the induced microstructural evolution during testing. The tensile stress-strain curves are compared at room temperature and elevated temperatures of 600, 650 and 700°C as shown in Figure 3.1. The corresponding tensile properties including tensile yield strength, ultimate tensile strength, fracture strength, elongation to failure and reduction in area, are shown in Table 3.2. The strength at room temperature tensile testing was much higher and decreased as the temperature increased. The higher testing temperature alters the microstructure which reduced the overall strength of the tested samples [15-16]. For example, the tensile testing at elevated temperature reduced the dislocation density and enhanced the dissolution of the strengthening precipitates which decreased their number density and led to their coarsening [1, 15]. The ductility, on the other hand, showed a noticeable reduction at higher temperatures compared to that of the sample tested at room temperature.

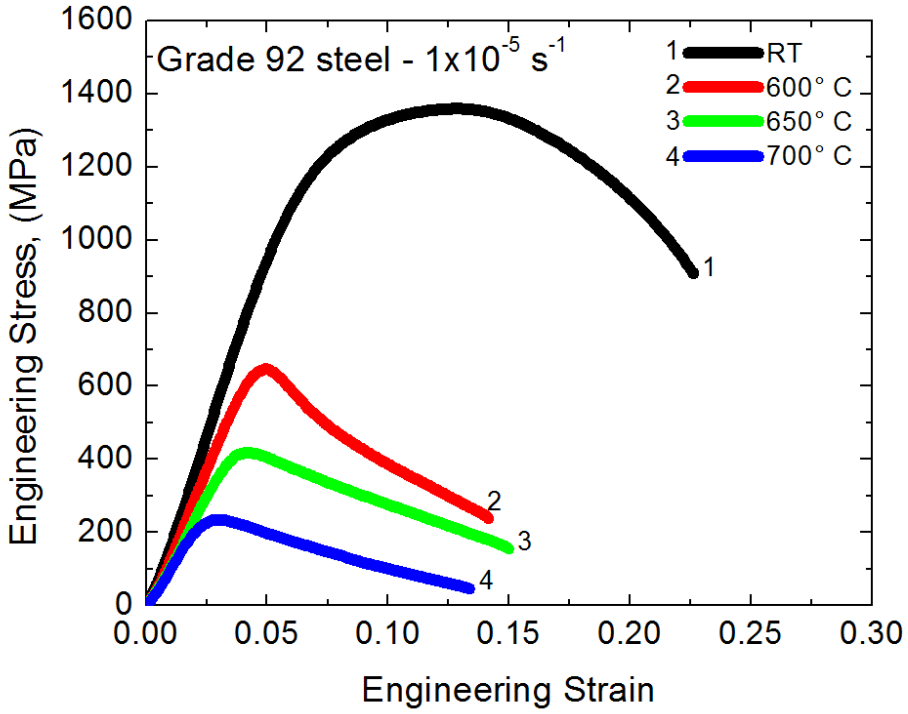

Figure 3.1. Tensile stress-strain curves of the Grade 92 steel at 10^{-5} s^{-1} strain rate and different temperatures.

Table 3.2. The tensile properties of the Grade 92 steel using the strain rate of 10^{-5} s^{-1}.

Condition	Yield strength (MPa) S_y	Ultimate tensile strength (MPa) S_u	Fracture strength (MPa) S_f	Elongation to failure *%EL*	Reduction in area %RA
RT	1038	1358	908	18.0	56.9
600°C	546	646	239	12.4	54.1
650°C	349	407	156	13.6	56.3
700°C	198	234	47	12.8	54.1

3.3.2. The microstructural evolution of the investigated samples

3.3.2.1. The microstructure of the as-received condition

The microstructure of the as-received Grade 92 steel is shown in Figures 3.2 and 3.3. Figure 3.2 shows the optical micrograph of the typical tempered martensite structure. Figure

3.3 shows the bright-field TEM microstructure of the as-received Grade 92 steel. The microstructure shows a highly dislocated tempered ferritic-martensitic (FM) structure. The elongated martensitic lath structure dominated the as-received microstructure and the dislocation density of the as-received condition was estimated as $(3.9\pm0.8) \times 10^{14}$ m^{-2} using TEM under the two-beam conditions. The estimated dislocation density is consistent with that of similarly tempered 9-12%Cr steels as they also have a high dislocation density, $(1\text{-}10) \times 10^{14}$ m^{-2} [20-21].

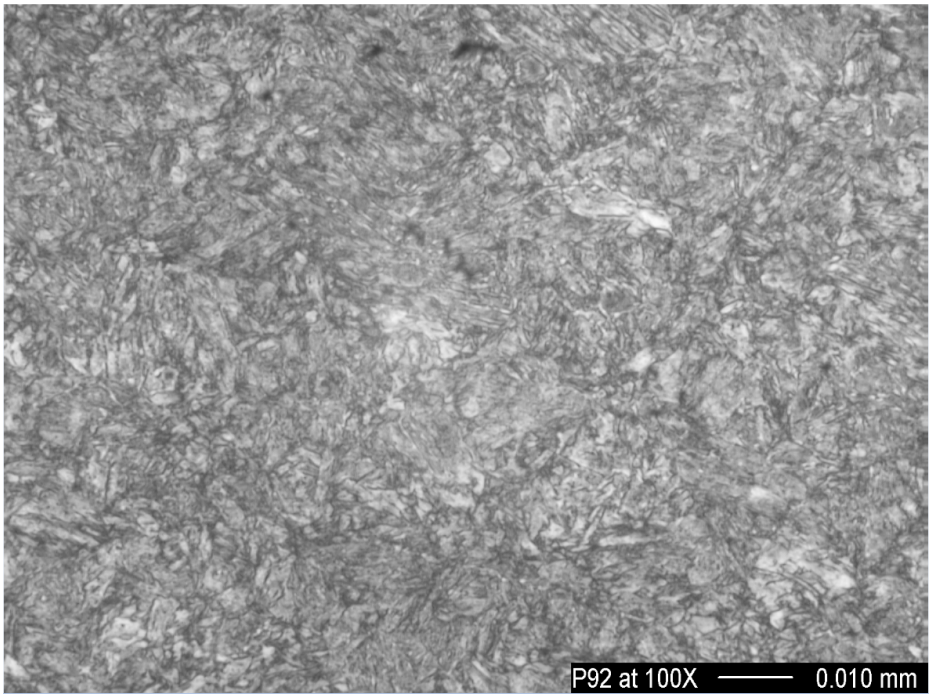

Figure 3.2. The optical micrograph of the as-received Grade 92 steel.

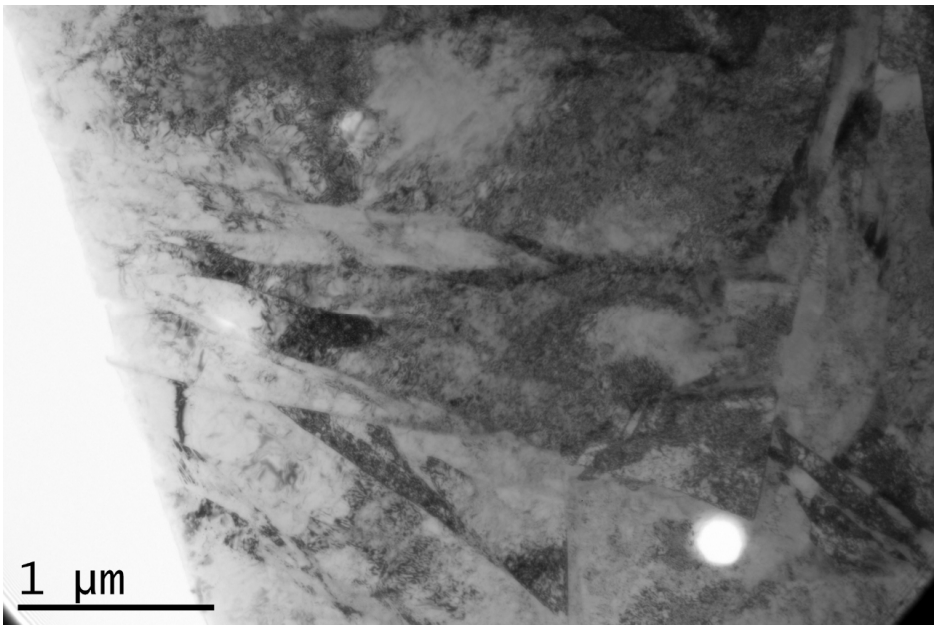

Figure 3.3. The microstructure of the as-received Grade 92 steel.

The presence of alloying elements such as Si, Cr, Mo and W increases the stability of the supersaturated iron-carbon solid solution and they cause the cementite to retain its fine Widmanstatten structure to higher temperature even after the fourth stage of tempering (i.e. up to 700°C) which significantly delay the softening of these steels during tempering [19]. That is why the microstructure of the as-received condition did not show definite $M_{23}C_6$ precipitates, i.e. $(Cr, Fe, Mo, W)_{23}C_6$ precipitate as shown in Figure 3.4. However, MX-type precipitates (i.e. (Nb, V)(N, C)) were observed with a diameter of around 50 nm. Also, the as-received alloy showed microstructure containing needle-like Fe-rich M_3C particles within the martensite laths under the STEM-mode as shown in Figure 3.4. The diffusivity of C and N is several orders of magnitude higher than other metallic elements considering that C and N diffuse interstitially through the iron lattice [19]. However, the other metallic elements diffuse substitutionally at higher temperatures through the iron lattice before the nucleation and growth of these alloy carbides [18].

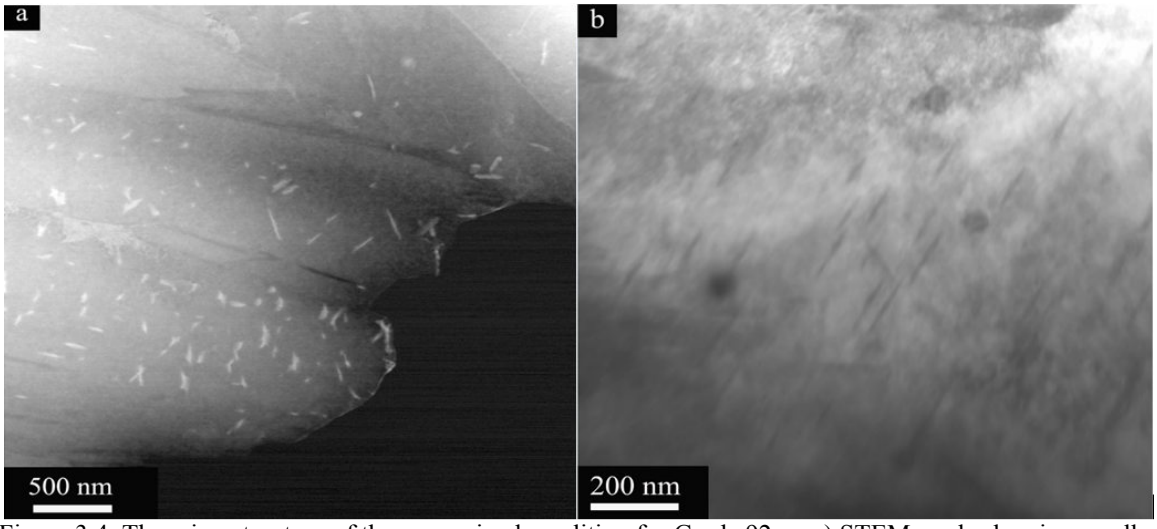

Figure 3.4. The microstructure of the as-received condition for Grade 92 on a) STEM mode showing needle-like Fe-rich M_3C particles and b) bright-field mode showing the needle-like M_3C particles and near-spherical MX-type precipitates.

Generally, the strength of high temperature steels is attributed to several strengthening mechanisms such as the solid solution strengthening, dislocation strengthening, precipitation strengthening, and boundary or sub-boundary strengthening [15]. The solid solution strengthening in 9-12% Cr steels has more significant strength than other strengthening mechanisms [22-23]. For instance, the dislocation movement will be hindered as the solute atoms in Grade 92 steel enhance the strength of the steel via the solid solution strengthening mechanism. The solute atoms occupy interstitial or substitutional sites which distort the parent lattice and introduce stress fields around these atoms [6, 24]. In Grade 92 steel, W and Mo (i.e. 1.66 and 0.55 wt.%, respectively) have much larger atomic size than iron and thus generate higher atomic misfit leading to a significant solid solution strengthening effect in these steels [6, 15, 24]. Resistance to creep rupture time has been shown to increase with the addition of W in the matrix; for instance, W addition has shown to slow down the recovery of the dislocation network and lath structure recovery in the microstructure as W in

solid solution retards the lath boundary migration [15]. Moreover, the coarsening rate of the MX-type precipitates in steels without W has been found to be more significant.

The solid solution strengthening, as a result of the local strain fields associated with different solute atoms sizes, enhanced the strength of the as-received condition. The contribution of solid solution strengthening as a result of the local strain fields associated with different solute atoms sizes can be described by the atomic misfit parameter (δ) and the shear modulus variation (η) as [25-26]:

$$\sigma_{SS} \cong \left(\sqrt{\delta^2 + \eta^2}\right)^m . c^n \quad (3.1)$$

where m is an interaction exponent, n concentration exponent (i.e. ~0.75) and c is the solute atoms concentration.

The atomic misfit parameter (δ) and the shear modulus variation (η) can be expressed as:

$$\delta = \frac{1}{a}\frac{da}{dc} \quad (3.2)$$

and,

$$\eta = \frac{1}{G}\frac{dG}{dc} \quad (3.3)$$

where a is the lattice constant, c the solute atoms concentration in the matrix, G is the shear modulus.

Hence, Equation (3.3) can be rewritten as:

$$\sigma_{SS} = \sum k_i . c_i^n \quad (3.4)$$

where the constant k (i.e. strengthening coefficient) is replacing both the atomic misfit parameter and the shear modulus variation.

Also, the strength of the as-received microstructure is, also, influenced by the detected precipitates and particles. For instance, as the microstructure of 9-12% Cr steels contains several types of precipitates, needle-like Fe-rich M_3C particles and carbonitride precipitates (i.e. MX-type) were detected within the martensite lath of the investigated as-received microstructure. The needle-like Fe-rich M_3C particles within the martensite lath of received condition had a length varying from ~50 nm to ~250 nm and around 15 nm thickness; however, the carbonitride particles had a spherical shape with a diameter of around 55 nm, Figure 3.4. Presence of these particles enhances the strength of the matrix via stabilizing the free dislocations and the sub-grain structure recovery at high temperatures [6, 27-28]. Moreover, they act as a barrier as dislocation moves which required higher stresses to excess certain threshold stress for dislocations to bypass particles, Orowan's mechanism [22, 27-28]. The induced strength is enhanced as the mean interparticle spacing becomes smaller, higher particle density [22, 27-28]. The precipitation strengthening (i.e. Orowan's equation) can be expressed as [29, 30]:

$$\Delta\sigma_{Or} = M\frac{0.4}{\pi}\frac{Gb}{\sqrt{1-v}}\frac{\ln\left(\frac{2r}{b}\right)}{\lambda} \quad (3.5)$$

where M is Taylor factor (i.e. taken 2.7 for BCC), G shear modulus, b Burgers vector, v Poisson's ratio, r average particle radius and λ is the inter-particle spacing which can be expressed as [29, 31]:

$$\lambda = [(\frac{3\pi}{4f})^{0.5} - 1.64]r \quad (3.6)$$

where f is the particle volume fraction.

Furthermore, the dislocation hardening mechanism is expected to enhance the strength of the investigated steel. For instance, the microstructure of the as-received Grade 92 steel

revealed a dislocation density of (3.9±0.8) × 10^{14} m^{-2}. The high dislocation density enhances the strength of the steel as the average distance between dislocations decreases; so, dislocations start blocking the motion of one another [23-24]. The Taylor's equation shows the contribution of dislocation strengthening as [29, 34]:

$$\sigma_D = M\alpha Gb\rho^{1/2} \quad (3.7)$$

where α is the dislocation strengthening coefficient (of the magnitude of about 0.4 [35] and ρ is the dislocation density.

Therefore, the contribution of the dislocation hardening mechanism was estimated to be 431 MPa.

Finally, the overall strengthening can be estimated as [29]:

$$\sigma_Y = \sigma_0 + \sigma_{SS} + \sigma_{Or} + \sigma_D \quad (3.8)$$

where σ_Y is the yield stress and σ_0 is the friction stress (50 MPa was used [29]).

3.3.2.2. Microstructural evolution at elevated temperatures

3.3.2.2.1. The non-deformed microstructure in Grade 92 steel

The microstructures of the non-deformed samples (taken from the grip regions of the tensile specimens) at 600 and 700°C are shown in Figures 3.5 and 3.6, respectively, where the microstructure was subjected to an annealing effect without being deformed under the application of load. The dislocation density of the non-deformed samples at 600°C was estimated as (1.1±0.2) × 10^{14} m^{-2}, which was lower than the as-received condition as annealing enhanced the dislocation annihilation mechanism leading to the reduction in dislocation density. Still, the microstructure of the non-deformed sample at 600°C did not show the formation of carbide precipitates either along the prior austenite grain boundaries

(i.e. PAGB) or lath boundaries highlighting the stability of the supersaturated iron-carbon solid solution with the presence of alloying elements such as Si, Cr, Mo and W. The V, W and Mo are strong carbide formers; still, higher temperatures appear to be needed in order for these elements to diffuse sufficiently rapidly to allow the formation of carbides [19]. Also, the needle-like Fe-rich M_3C particles were not detected within the non-deformed microstructure at 600°C. The dark-field TEM image of the non-deformed microstructure at 600°C showed thin grain boundary films as shown in Figure 3.5b. The nucleation of the carbides along the various boundaries within the microstructure is one of the ways of forming alloy carbides in steels [19]. For instance, boundaries are energetically favorable sites providing paths for solute atoms to diffuse rapidly and this early stage of carbide formation is not stable in many steels [19, 31]. Looking at the mechanical properties in Table 3.1, these thin grain boundary films may play a role in reduction of ductility by as much as 30% (i.e. from 18% to 12 %).

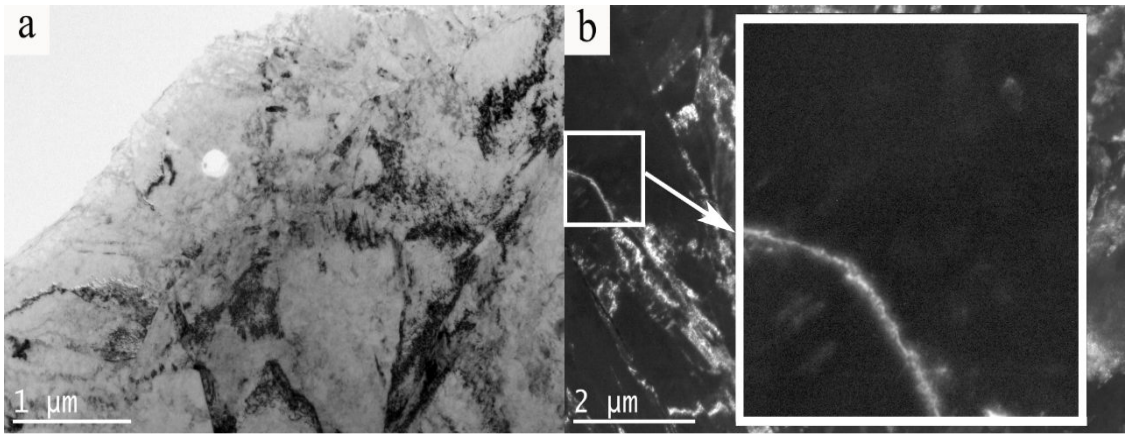

Figure 3.5. TEM images of the microstructure from the grip region (non-deformed) of the tensile specimen deformed at 600°C and 10^{-5} s^{-1} under a) bright-field and b) dark-field imaging modes.

At 700°C, there was an observable reduction in dislocation density. For instance, the estimated dislocation density of the non-deformed sample at 700°C was estimated to be $(0.94\pm0.4) \times 10^{14}$ m^{-2}. On the other hand, a STEM image shows the nucleation and

precipitation of carbides along PAGB and laths, as shown in Figure 3.6. As the annealing process progress at higher temperature, nucleation and growth of carbides become more significant along the boundary regions [19, 37]. Cr element diffuses more rapidly than most of the other metallic alloying elements and the addition of W enhances the nucleation and formation of $M_{23}C_6$ precipitates where M denotes Cr, Fe, Mo and/or W [15, 37]. As those precipitates grow, they deteriorate the solid solution strengthening effect by removing two of the main strengthening elements, W and Mo. The $M_{23}C_6$ carbide precipitates present in the non-deformed microstructure at 700°C were more spherical and more than 150 nm particles were detected; however, $M_{23}C_6$ carbide possessed an average diameter of ~75 nm. Apart from the deterioration of the solid solution strengthening, the presence of $M_{23}C_6$ precipitates on the lath boundaries indirectly help in restricting the growth of subgrains.

The particle compositions were measured using the EDS technique. On Figure 3.7, two particles are marked. These particles were identified via EDS, Figure 3.8, as these particles are Cr, W and Mo enriched precipitates; also, the MX-particles are shown as V-Nb bearing carbonitrides. The MX-type precipitates were much more resistant to coarsening, which is related to their high stability; hence, they maintained their size at ~50 nm [5, 38].

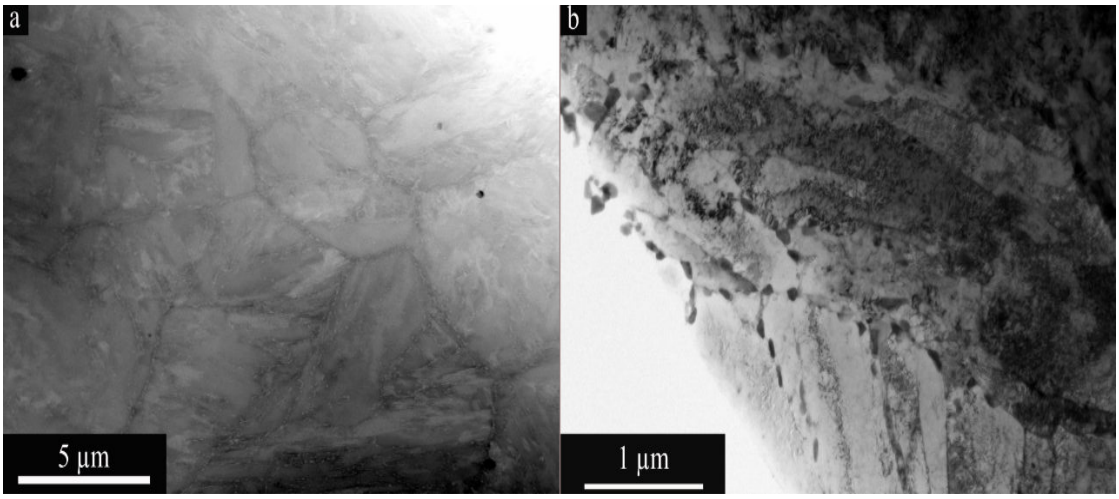

Figure 3.6. The non-deformed microstructure from the grip region of the tensile specimen deformed at 700°C and 10^{-5} s^{-1} on TEM a) STEM mode and b) bright-field mode.

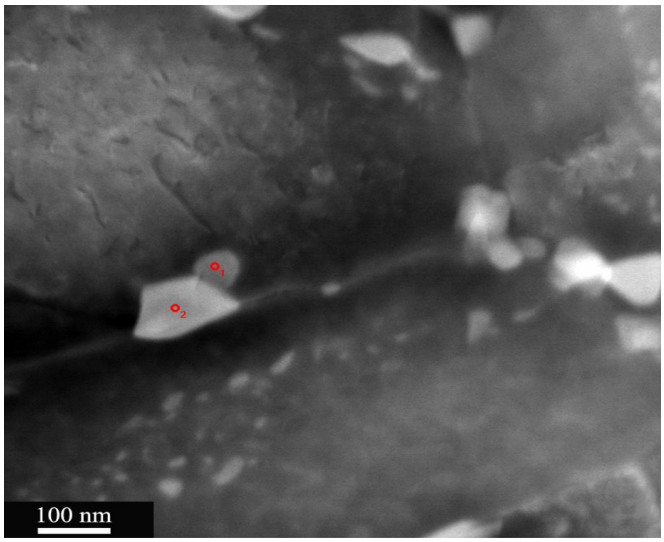

Figure 3.7. The STEM image of the non-deformed microstructure from the grip region of the tensile specimen deformed at 700°C and 10^{-5} s^{-1} showing the MX-type particles (point 1) and $M_{23}C_6$ particles (point 2).

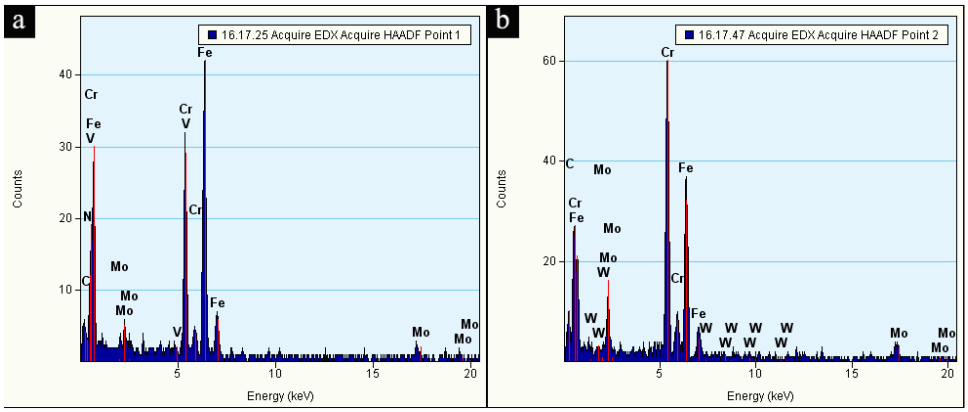

Figure 3.8. The EDS spectra of the two particles shown on Figure 3.7: a) point 1 and b) point 2.

3.3.2.2.2. Deformed microstructure in Grade 92 steel

The deformed microstructure of the tested specimens at 600°C and 10^{-5} s^{-1} strain rate is shown in Figure 3.9. The elongated deformed laths were dominating the microstructure; the lath width was 137±9 nm. As no carbide precipitates were detected in the non-deformed microstructure at 600°C and 10^{-5} s^{-1}, the deformed microstructure at 600°C and 10^{-5} s^{-1} shows the early stages of carbide precipitate nucleation along the lath boundaries as shown in Figure 3.9b, their length was around ~25 nm and width of ~15 nm. In 9-12% Cr steels, the carbide precipitation is much larger at the vicinity of the boundaries and microstructural evolution accelerates under loading [15, 39]. For instance, the solute atoms around moving dislocations are transported under loading to grain boundaries as dislocations can preferentially escape from boundaries vicinity, which enhances the carbide precipitation at grain boundaries under stress [39]. Thus, stress might preferentially activate the Cr diffusion as the diffusion of elements is influenced by the stress in solids [39-40]. According to Yamada *et al.*, precipitate growth accelerates under stress as a result of the enhanced diffusivity of solute atoms under stress [33]. The effective diffusivity of solute atoms was expressed as [39, 41]:

$$D_{eff} = D_L + (\frac{1}{\varphi})(\frac{L}{b})\varepsilon C_o D_p \qquad (3.9)$$

where D_L is lattice diffusivity, φ is the conversion factor from shear strain to tensile strain, L effective diameter of the solution atmosphere, b Burgers vector, ε the tensile strain, C_0 the atomic fraction of solutes in matrix and D_p is the pipe diffusivity [39]. This would explain the early stages of carbide precipitation in the deformed microstructure at 600°C while the non-deformed (i.e. statically annealed) microstructure at this certain temperature did not show any carbide precipitates.

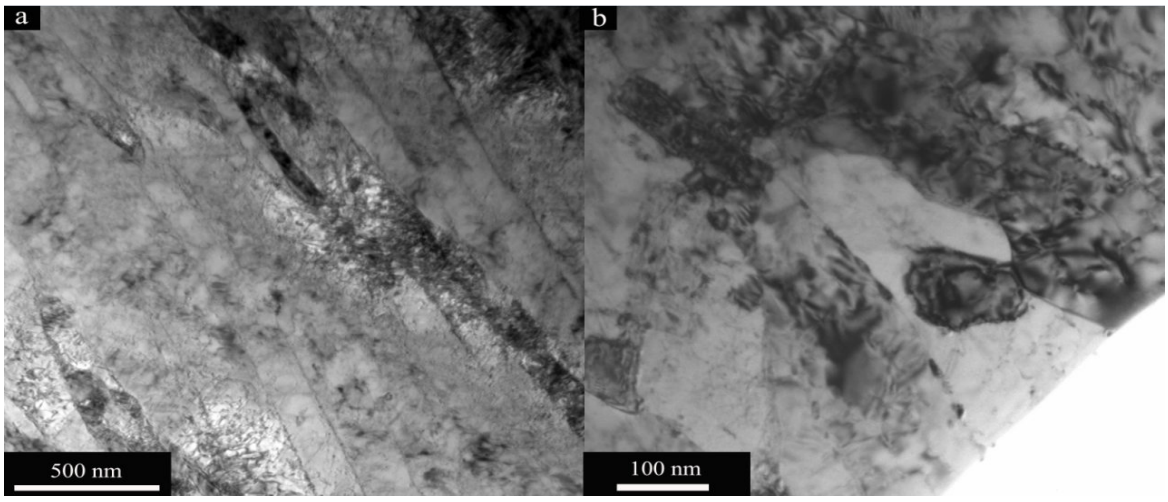

Figure 3.9. The bright-field TEM images of deformed microstructure (from the gage region of the tensile specimen tested at 600°C and 10^{-5} s^{-1} strain rate showing a) the deformed lath structure and b) the carbide precipitation along the lath at higher magnification.

The deformed microstructure of tensile samples tested at 650 and 700°C and 10^{-5} s^{-1} are shown in Figures 3.10 and 3.11, respectively. The carbide precipitation progressed along the elongated deformed grains and lath width showed appreciable widening. For instance, the lath widths were 174.2±26 and 234±26.3 nm for tested specimens at 650 and 700°C, respectively. The deformed samples at 650°C revealed an equiaxed and plate-like $M_{23}C_6$ particles, around 105 nm in length.

However, more than 300 nm long carbides were detected at 700°C throughout the microstructure. Also, the microstructure of the deformed sample at 700°C shows formation of subgrains. It is believed that the formation of $M_{23}C_6$ precipitates induces the essential pinning effect to stabilize the recovery of laths and subgrains [15, 38]. In fact, the effective size for $M_{23}C_6$ precipitates was estimated to be around 150 nm; beyond that, these precipitates lost their efficiency in providing the needed pinning effect. Their length increased from around 105 nm to around 300 nm after increasing the tensile test temperature from 650 to 700°C, which confirms the significant growth of these carbides. The $M_{23}C_6$ precipitates coarsening in 9-12% Cr steels at elevated temperatures is believed to obey

Ostwald ripening mechanism according to F. Abe [21]. On the other hand, the MX-type precipitates did not show any noticeable coarsening which comes in good agreement with the literature [42-44].

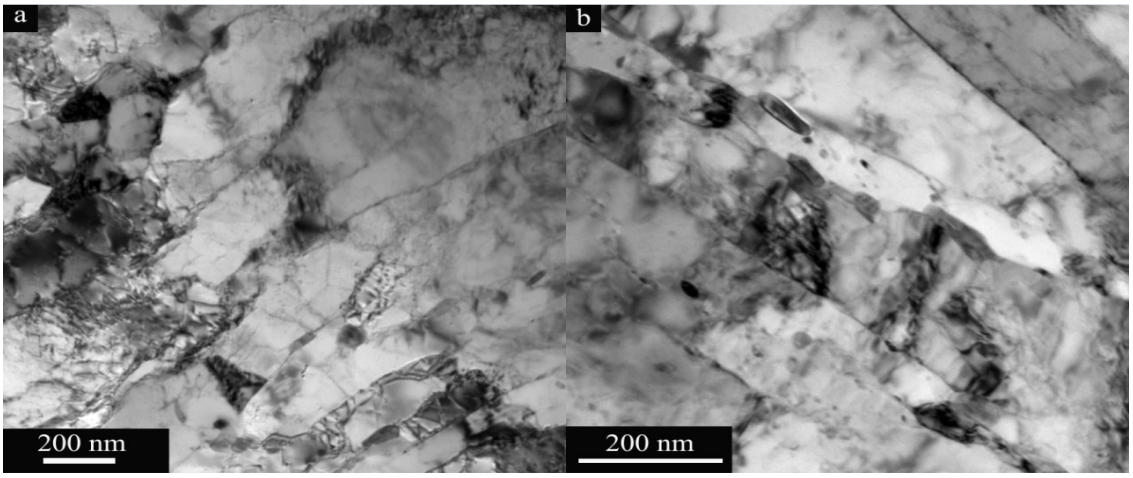

Figure 3.10. TEM images of the deformed microstructure from the gage section of the tensile specimen tested at 650°C and 10^{-5} s^{-1} strain rate a) at 10 kx and b) at 15 kx.

The precipitate strengthening is defined as one of the strengthening mechanisms in 9-12% Cr steels. As these particles coarsen, their effectiveness in hindering the dislocation movement diminishes leading to the deterioration of strength in these steels. Moreover, the formation of the carbide precipitates (i.e. namely $M_{23}C_6$) removes the solid solution strengthening elements, such as W and Mo, from the matrix which explains in part the reduction in strength with increasing temperature [5]. In addition, the observed lath widening along the associated dislocation density reduction at elevated temperatures furthermore contribute destructively to the overall strength of the material.

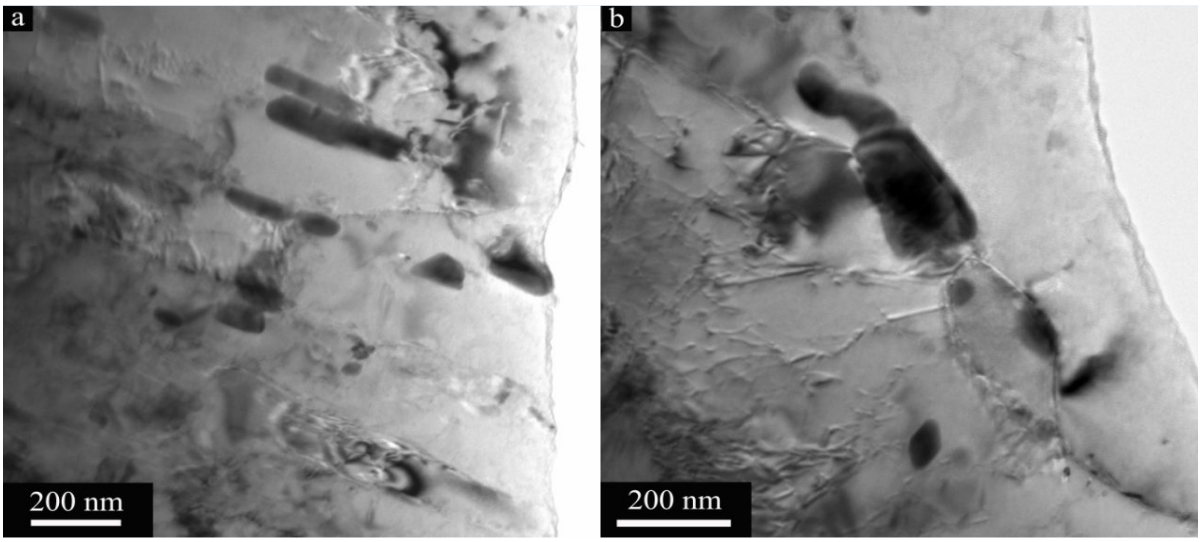

Figure 3.11. TEM images of the deformed microstructure from the gage section of the tensile specimen tested at 700°C and 10^{-5} s^{-1} strain rate on TEM a) at 12 kx and b) at 20 kx.

The volume fraction of the strengthening particles $M_{23}C_6$ and MX in the deformed microstructure at 700°C were estimated as 0.09 and 0.02, respectively.

3.3.3. The prediction of the yield strength based of the obtained microstructure

3.3.3.1. The yield strength for the as-received condition

The contribution of solid solution strengthening as a result of the local strain fields associated with different solute atoms sizes can be described by the atomic misfit parameter was shown in Eqn. 3.1. It was shown that the strengthening coefficient is replacing both the atomic misfit parameter and the shear modulus variation. Here, the main alloying elements of Cr, W, Mo, Si, Mn will be used to estimate the contribution of solid solution strengthening. The strengthening coefficient values for the main alloying elements of Cr, W, Mo, Si, Mn are 9.5, 76, 66, 76, 48, respectively [25-26]. As a result, using Eqn. 3.4, the contribution of solid solution strengthening was estimated to be 261 MPa. It is wise to point out that the induced solid solution strengthening is remarkably affected as a result of the depletion associated with the precipitation processes at higher temperatures.

The contribution of precipitation strengthening of the as-received microstructure is, also, influenced by the detected M_3C particles and carbonitride precipitates (i.e. MX-type). According to their sizes on the as-received condition, the induced precipitation strengthening according to the detected particles was estimated taking into account the observed microstructure using Orowan's equation, Eqn. 3.5. Table 3.3 shows the estimated parameters of the microstructure of the as-received condition and the material parameters used in this study. Accordingly, the contribution of precipitation strengthening was estimated to be 195 MPa, 101 MPa for MX particles and 94 MPa for M_3C.

Table 3.3. The estimated parameters of the microstructure of the as-received condition and the material parameters.

Parameter	Value	Reference
M	2.7	[22]
G	81 GPa	[32]
υ	0.3	[33]
b	0.25 nm	[33]
f_{M3C}	0.024	
f_{MX}	0.022	
r_{M3C} (aspect ratio)	69.6 nm	
r_{MX}	55.8 nm	

The microstructure of the as-received Grade 92 steel revealed a dislocation density of $(3.9\pm0.8) \times 10^{14}$ m^{-2}. The Taylor's equation (Eqn. 3.7) shows the contribution of dislocation strengthening to be 431 MPa.

Finally, the overall strengthening according to Eqn. 3.8 can be estimated was estimated to be 937 MPa for the as-received condition after adding the friction stress (experimental value was 1031±5 MPa). Table 3.4 shows the prediction of the yield strength based on the

obtained microstructure for the as-received condition considering the involving strengthening mechanisms.

Table 3.4. The prediction of the yield strength based on the obtained microstructure for the as-received condition.

<table>
<tr><th>Strengthening mechanism</th><th>Involved parameter</th><th>The contribution (MPa)</th><th>Reference</th></tr>
<tr><td>$\sigma_{SS} = \sum k_i . c_i^n$</td><td>Cr, W, Mo, Si, Mn</td><td>261</td><td>[25-26]</td></tr>
<tr><td>$\Delta\sigma_{Or} = M\frac{0.4}{\pi}\frac{Gb}{\sqrt{1-\upsilon}}\frac{\ln\left(\frac{2r}{b}\right)}{\lambda}$

$\lambda = [(\frac{3\pi}{4f})^{0.5} - 1.64]r$

(For M_3C and MX-type particles)</td><td><table><tr><td>M</td><td>2.7</td></tr><tr><td>G</td><td>81 GPa</td></tr><tr><td>υ</td><td>0.3</td></tr><tr><td>b</td><td>0.25 nm</td></tr><tr><td>f_{M3C}</td><td>0.024</td></tr><tr><td>f_{MX}</td><td>0.022</td></tr><tr><td>r_{M3C} (AR)</td><td>69.6 nm</td></tr><tr><td>r_{MX}</td><td>55.8 nm</td></tr></table></td><td>M_3C: 94
MX: 101</td><td>[22, 29, 32-33]</td></tr>
<tr><td>$\sigma_D = M\alpha Gb\rho^{1/2}$</td><td>$\rho_{as\text{-}received}$= 3.9×10^{14} m^{-2}</td><td>431</td><td>[34]</td></tr>
<tr><td>$\sigma_Y = \sigma_0 + \sigma_{SS} + \sigma_{Or} + \sigma_D$</td><td>$\sigma_0$= 50 MPa</td><td>937</td><td>[29]</td></tr>
<tr><td colspan="4">Experimentally obtained result = 1031±5 MPa</td></tr>
</table>

3.3.3.2. The yield strength for the deformed microstructure at 700°C

The contribution of the strengthening particles (mainly MX particles) in the deformed microstructure at 700°C according to their volume fraction was calculated to be 39 MPa. It

should to be taken in account that the temperature dependence of modulus at higher temperature (i.e.$\frac{T_m}{\mu_0}\frac{d\mu}{dT}$) was taken as -1.09 as stated in [32]. As a result, the shear modulus was calculated to be 48 GPa at 700°C.

Also, the contribution of the solid solution strengthening at elevated temperature is expected to operate up to $0.6T_m$ (i.e. 813°C). Therefore, it is important to estimate the contribution of the solid solution strengthening at 700°C. The formation of $M_{23}C_6$ precipitates, i.e. $(Cr, Fe, Mo, W)_{23}C_6$, removes beneficial contribution of these solid solution strengthening elements from the matrix. At 700°C, the volume fraction of $M_{23}C_6$ was estimated as 0.09 and attempt was dedicated to estimate the corresponding weight percent. In the beginning, it has been assumed that these precipitate contains only Cr. Using the data of the $M_{23}C_6$ volume fraction, stoichiometry and density, the removed Cr from matrix was estimated to be 7.5 wt% (1.4 wt% remaining). Since only Cr was assumed to precipitate at this stage, the nominal composition of the other strengthening elements W and Mo was kept the same. Therefore, the contribution of the solid solution strengthening at 700°C, taking into account the temperature dependence of the shear modulus, was estimated as 99 MPa. It should be pointed out that the contribution of the solid solution strengthening at 700°C is expected to be much lower as W and Mo precipitate.

The contribution of dislocation strengthening is not expected to be effective at elevated temperature. Along the reduction in dislocation density, the subgrain formation was more abundant in the deformed microstructure at 700°C. As stress enhances the number of mobile dislocations, the dislocation mobility improves at elevated temperatures. Thus, the subgrain formation accelerates as a result of increasing the dislocations mobility and quantity. Figure 3.12 shows the formed subgrains for the deformed microstructure at 700°C.

The strength of the deformed microstructure at 700°C was also augmented by the subgrain hardening as these interfaces hinder the dislocation movement. The subgrain formation is promoted by the recovery of excess dislocations at elevated temperature when the sub-boundary hardening mechanism is considered. Therefore, the strength increases as the size of the subgrains decreases [16, 36]. Hence, the contribution of the sub-boundary hardening mechanism depends on the formed subgrain size according to Abe [15]:

$$\sigma_{sg} = 10Gb/\lambda_{sg} \quad (3.10)$$

where λ_{sg} is defined as the formed subgrains width.

Consequently, the formed subgrain width was measured as 2.7 μm and the contribution of the tempered lath structure was estimated as 44 MPa. Finally, the yield strength for the deformed sample at 700°C was estimated as 212 MPa after adding the friction stress at 700°C (experimental value was 198 MPa). Table 3.5 shows the prediction of the yield strength based on the obtained microstructure at 700°C considering the involving strengthening mechanisms.

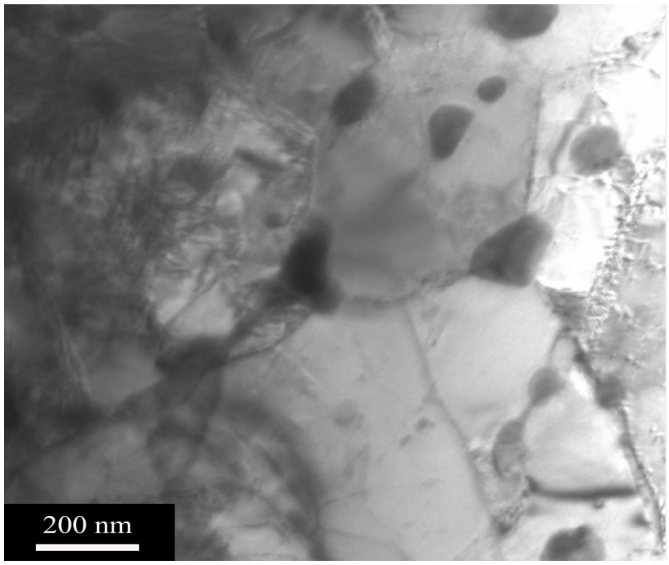

Figure 3.12. TEM images of the promoted subgrain formation of the deformed microstructure from the gage section of the tensile specimen tested at 700°C and 10^{-5} s^{-1} strain rate.

Table 3.5. The prediction of the yield strength based on the obtained microstructure at 700°C.

<table>
<tr><th>Strengthening mechanism</th><th>Involved parameter</th><th>The contribution (MPa)</th><th>Reference</th></tr>
<tr><td>$\Delta\sigma_{Or} = M\frac{0.4}{\pi}\frac{Gb}{\sqrt{1-\upsilon}}\frac{\ln\left(\frac{2r}{b}\right)}{\lambda}$

$\lambda = [(\frac{3\pi}{4f})^{0.5} - 1.64]r$

(For MX-type particles)</td><td><table><tr><td>M</td><td>2.7</td></tr><tr><td>$\frac{T_m}{\mu_0}\frac{d\mu}{dT}$</td><td>-1.09</td></tr><tr><td>G @700°C</td><td>48 GPa</td></tr><tr><td>υ</td><td>0.3</td></tr><tr><td>b</td><td>0.25 nm</td></tr><tr><td>f_{MX}</td><td>0.02</td></tr><tr><td>r_{MX}</td><td>56 nm</td></tr></table></td><td>MX: 39</td><td>[22, 29, 32-33]</td></tr>
<tr><td>$\sigma_{SS} = \sum k_i . c_i^n$</td><td>Affected by the $M_{23}C_6$ particle size</td><td>99</td><td>[25-26]</td></tr>
<tr><td>$\sigma_{sg} = 10Gb/\lambda_{sg}$</td><td></td><td>44</td><td>[15]</td></tr>
<tr><td>$\sigma_Y = \sigma_0 + \sigma_{SS} + \sigma_{Or} + \sigma_D$</td><td>$\sigma_0$= 30 MPa</td><td>212</td><td>[29]</td></tr>
<tr><td colspan="4">Experimentally obtained result = 198 MPa</td></tr>
</table>

3.3.4. Fracture behavior

The fracture surfaces of the tested samples at room temperature and elevated temperatures are shown in Figures 3.13 and 3.14. Figure 3.13 shows the low magnification of the fracture tips of the specimens tested at the strain rate of 10^{-5} s^{-1}. The fracture surface at room temperature showed the appearance of chisel tip in a lower magnification which results from the splitting of the martensite lath boundaries. On the other hand, the elevated

temperature fracture surfaces showed the typical cup and cone fracture mode. The observed fracture surfaces at elevated temperatures showed more necking which was consistent with the estimated reduction in area, Table 3.2.

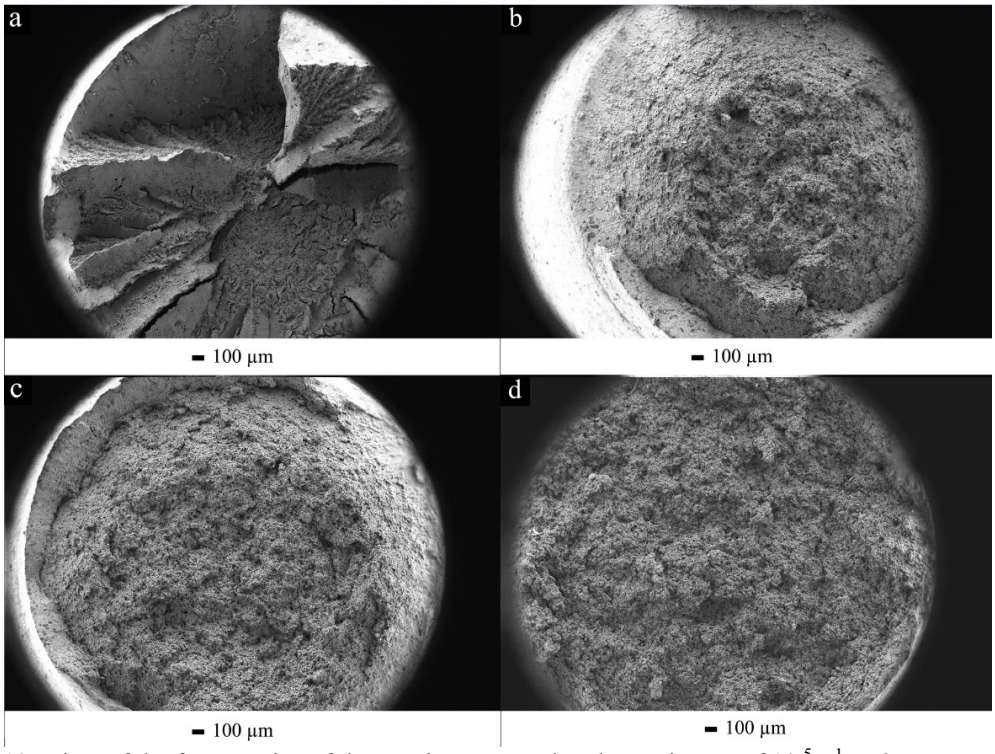

Figure 3.13. View of the fracture tips of the specimens tested at the strain rate of 10^{-5} s^{-1} and temperatures of a) 25°C, b) 600°C, c) 650°C and d) 700°C.

At higher magnification, ductile dimples which resulted from the coalescence of microvoids were observed at all temperatures, Figure 3.14. The fracture mode was dominated by these dimples and the size of the observed dimples increases as temperature increases which indicates the dominance of growth processes and the reduction in numbers of microvoid nucleation.

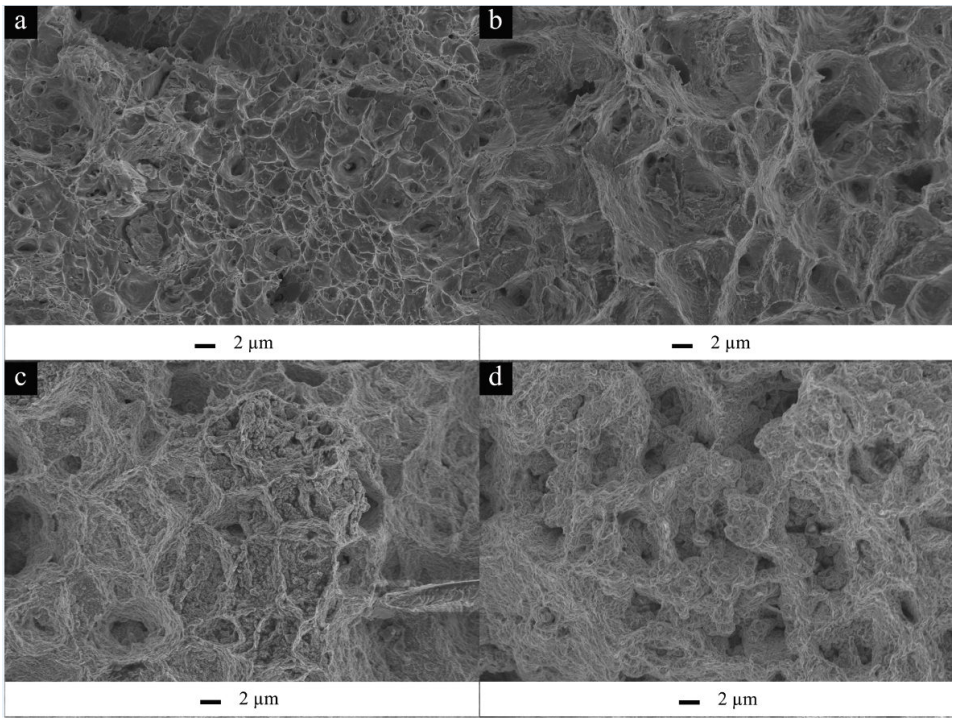

Figure 3.14. The microscopic views of the fracture surfaces of the tensile samples tested at the strain rate of 10^{-5} s^{-1} and at temperatures of at a) 25°C, b) 600°C, C) 650°C, and d) 700°C.

3.4. Conclusion

The tensile properties (as tested at the strain rate of 10^{-5} s^{-1}) of 9Cr-2W steel at room temperature and elevated temperatures of 600, 650 and 700°C were evaluated. The microstructure of the non-deformed samples and deformed samples were investigated. The following observations were made:

1. The high strength of the investigated 9Cr-2W steel at room temperature was attributed mainly to the solid solution strengthening mechanism imparted by strong solid solution strengtheners, MX-type precipitates and high dislocation density.
2. The contribution of main strengthening mechanisms of solid solution strengthening, precipitation strengthening and dislocation hardening was estimated quantitatively for the as-received condition to be 937 MPa.

3. The reduction in strength at elevated temperatures was attributed to the microstructural evolution; mainly, the precipitates growth, subgrain formation and the associated depletion of the strengthening elements.
4. As testing temperature increased, the $M_{23}C_6$ precipitation progressed more and precipitation increases with the increase in testing temperature. On the other hand, the other carbonitride particles exhibited good thermal stability against coarsening.
5. The contribution of main strengthening mechanisms of solid solution strengthening, precipitation strengthening and subgrain hardening was estimated at 700°C.

References

[1] R. Klueh, A. Nelson, J. Nucl. Mater., 371 (2007) 37–52.

[2] C. Kellera, M.M. Margulies, Z. Hadjem-Hamouche, I. Guillot, Mater. Sci. Eng. A, 527(24–25) (2010) 6758–6764.

[3] J. Hald, Int. J. Pres. Ves. Pip., 85 (2008) 30–37.

[4] H. K. Danielsen, J. Hald, Comput. Coupling Phase Diagrams Thermochem., 31 (2007) 505-514.

[5] P.J. Ennis, A. Zielinska-Lipiec, O. Wachter, A. Czyrska-Filemonowicz, Acta Mater., 45 (1997) 4901-4907.

[6] R. L. Klueh, R. Donald, R. Harries, High Chromium Ferritic and Martensitic Steels for Nuclear Applications, W. Conshohocken, PA, 2001.

[7] C. Topbasi, A. Motta, M. Kirk, J. Nucl. Mater., 425 (2012) 48-53.

[8] K. Sawada, M Takeda, K. Murayama, R. Ishii, M. Yamada, Y. Nygae, R. Komine, Metall. Mater. Trans., A 267 (1999)19-25.

[9] R.L. Klueh, Int. Mater. Rev. 50 (2005) 287-310.

[10] F. Masuyama, Int. J. Pres. Ves. Pip. 84 (2007) 53-61.

[11] Y. Kadoya, T. Goto, S. Date, T. Yamauchi, T. Saida, and T. Sada, ISIJ Int. 30 (1990) 854-861.

[12] K. Kimura, Y. Toda, H. Kushima, K. Sawada, Int. J. Pres. Ves. Pip. 87 (2010) 282-288.

[13] K. Sawada, K. Kubo, F. Abe, Mater. Sci. Eng. 319 (2001) 784-787.

[14] M. Yurechko, C. Schroer, A. Skrypnik, O. Wedemeyer, J. Konys, J. Nucl. Mater., 432 (2013) 78-86.

[15] F. Abe, Strengthening mechanisms in creep of advanced ferritic power plant steels based on creep deformation analysis, in: Y. Weng, D. Hand (Eds.). Advanced Steels: The Recent Scenario in Steel Science and Technology, Metallurgical Industry, Beijing, 2011, pp. 409-22.

[16] F. Abe, S. Nakazawa, H. Araki, T. Noda, Metall. Trans., A23 (1992) 469–477.

[17] L. Cipolla. H. K. Danilesen. D. Venditti, P.E. Di Nunzio, J. Hald, M. A. J. Somers, Acta Mater., 58 (2010) 669-679.

[18] R.L. Higginson, C.M. Sellars, Worked Examples in Quantitative Metallography, first ed., Maney Publishing, London, 2003.

[19] R. W. K Honeycombe, H. K. Bhadeshia, Steels: Microstructure and Properties, second ed., Edward Arnold, London, 1995.

[20] N. Ridley, S. Maropoulos, J. D. H. Paul, Mater. Sci. Tech. 10 (1994) 239-249.

[21] F. Abe, Metall. Mater. Trans., A34 (2003) 913-925.

[22] K. Maruyama, K. Sawada, J. Koike, ISIJ Int., 41 (2001) 641-653.

[23] R. Abbaschian, R. E. Reed-Hill, Physical Metallurgy Principles, fourth ed., Van Nostrand, New Jersey, (2008).

[24] F. Abe, Mater. Sci. Eng. A 319-321 (2001) 770-773.

[25] M. Butt, P. Feltham, J. Mater. Sci., 28 (1993) 2557-2576.

[26] C. Lacy, M. Gensamer, Trans. Am. Soc. Met., 32 (1944) 88-110.

[27] M. Taneike, F. Abe, and K. Sawada, Nature, 424 (2003) 294-296.

[28] R. C. Thomson, H. K. D. H. Bhadeshia, Metall. Trans., A23 (1992) 1171-1179.

[29] J. Wang, W. Yuan, R. S. Mishra, I. Charit, J. Nucl. Mater., 432 (2013) 274–280.

[30] L.M. Brown, R.K. Ham, Dislocation-particle interactions, A. Kelly, R.B. Nicholson (Eds.), Strengthening Methods in Crystals, Elsevier, Amsterdam (1971), pp. 9–135.

[31] E. Nembach, Particle Strengthening of Metals and Alloys, first ed., Wiley, New York, 1996.

[32] H.J. Frost, M.F. Ashby, Deformation Mechanism Maps, Pergamon Press, New York, NY (1982) pp. 61–70

[33] T. Shrestha, M. Basirat, I. Charit, G.P. Potirniche, K.K. Rink, Materials Science and Engineering: A, 565 (2013) 382–391.

[34] J.E. Bailey, P.B. Hirsch, Philos. Mag., 5 (1960), 485–497.

[35] T. Endo, F. Masuyama, K.S. Park, Materials Transactions, 2 (2003) 239-246.

[36] S. Takeuchi, A. S. Argon, J. Mater. Sci., 11 (1976) 1542-1566.

[37] V. Dudko, A. Belyakov, R. Kaibyshev, Mater. Sci. Forum, 706-709 (2012) 841-46.

[38] W. Yan, W. Wang, Y.Y. Shan, K. Yang, Front Mater. Sci., 7(1) (2013) 1–27.

[39] S. Yamada, M. Yaguchi, T. Ogatab, Mater. Sci. Eng. A, 560 (2013) 450–457.

[40] A.J. Ardell, S.V. Prikhodko, Acta Mater., 51 (2003) 5013–5019.

[41]T. Nakajima, M. Takeda, T. Endo, Mater. Sci. Eng. A 387–389 (2004) 670–673.

[42] J. Hald, L. Korcakova , ISIJ Int, 43(3) (2003) 420-427.

[43] M. Hattestrand, M. Schwind, H.-O. Andren, Mater Sci Eng A, 250 (1998) 27-36.

[44] J. Hald, VGB PowerTech, 12 (2004) 74-79.

CHAPTER 4: Microstructural Stability in 9Cr-2W Steel at Different Stages of Tempering and Its Effect on Mechanical Properties

Sultan Alsagabi [a,b], *Indrajit Charit* [a,1]

[a] *Department of Chemical and Materials Engineering, University of Idaho, Moscow, ID 83844, USA*

[b] *Atomic Energy Research Institute, King Abdulaziz City for Science and Technology, P.O. Box 6086, Riyadh 11442, Saudi Arabia*

(*To be submitted to the Journal of Materials Science*)

Abstract

The thermal stability of the microstructure of 9Cr-2W steel at different stages of tempering and its effect on the mechanical properties were investigated through a set of tempering treatments. Tempering was conducted at 560, 660 and 760°C for 10, 100 and 1000 hours to investigate the microstructural evolution. Mechanical properties were evaluated via tensile testing and hardness. The $M_{23}C_6$ particles were found to form along the prior austenite grain boundaries and lath boundaries before its coarsening at higher temperatures. The coarsening rate of $M_{23}C_6$ carbides was higher than the MX-type particles which appeared to possess very good coarsening resistance. However, the coarsening rates of $M_{23}C_6$ carbides was slower than the Laves phase particles which coarsen rapidly when they formed after long tempering times. The subgrain formation was associated with the lath widening mechanism at higher tempering temperatures and it was more pronounced at the highest tempering temperature. The influence of the tempering on the hardness data was demonstrated by using the Hollomon-Jaffe parameter as a function of both tempering temperature and time.

Keywords: 9Cr-2W steel; tempering; hardness; microstructural evolution

4.1.Introduction

The Grade 92 steel (9Cr-2W) was introduced by Nippon Steel in Japan and was given the designation NF616. It is basically an advanced version of the previous generation steel Grade 91, *aka* modified 9Cr-1Mo [1-2]. The Grade 92 steel possesses superior properties as a result of the fine and stable carbides and carbonitride precipitates which hinder the dislocations movement [3-4]. These precipitates form during the tempering of the martensitic structure in the form of carbides, carbonitrides and nitrides which enhance the mechanical strength of Grade 92 [5]. For instance, the coarse $M_{23}C_6$ {i.e. (Cr, Fe, Mo, W)$_{23}C_6$} carbides were observed to precipitate, preferentially, on prior austenite grain boundaries (PAGB), lath boundary, subgrain boundaries. However, the fine MX {i.e. (Nb,V)(N,C)} particles were observed to precipitate within martensite laths [2]. The $M_{23}C_6$ phase is considered the main precipitate in 9-12% Cr steels and they stabilize the lath structure. However, MX precipitates are finer than $M_{23}C_6$ carbide and form when strong carbide and/or carbonitride formers such as V, Nb or Ta are added to the matrix. As a result, the precipitate/dislocation interaction leads to improvement in the mechanical strength as precipitates hinder the movement of dislocations [1-2, 5]. Also, the subgrain growth can be impeded via these precipitates, which influence the strength properties through the subgrain hardening mechanism [1-2, 5]. Moreover, the fine MX precipitates enhance the strength as a result of pinning the free dislocations which contributes to the overall strength of these steels [1-2]. The coarse carbide precipitates (i.e. $M_{23}C_6$) and the fine MX-type precipitates improve the mechanical properties; however, their coarsening behavior varies greatly within a wide range of temperatures [1-2, 5].

Under elevated temperature exposure, significant microstructural changes take place such as dislocation density reduction, subgrain formation, precipitate coarsening and precipitation of secondary phases [3, 6]. The coarsening rate of fine MX precipitates is lower than that of the coarse $M_{23}C_6$ precipitates. The coarsening rate of $M_{23}C_6$ precipitates allows for the martensite lath to transform to more equiaxed subgrains which deteriorate the mechanical properties [3, 6]. In addition, the precipitation of secondary phases in Grade 92 steels such as the formation of the Laves phase, $(Fe,Cr)_2(Mo,W)$, and Z-phase, (Cr(V,Nb)N), occur [16]. The formation of Laves phase occurs at temperatures higher than 600°C and accelerates rapidly under loading [7]. Laves phase preferentially forms along the PAGBs and lath boundaries, and eventually its high growth weakens the solid solution strengthening [8-9]. On the other hand, the formation of Z-phase, defined as Cr(V,Nb)N, was found to occur at the expense of MX carbonitrides, leading to deterioration of creep performance [10].

Both microstructural stability and mechanical properties of Grade 92 have not been investigated extensively and further research needs to be conducted. Given the importance of Grade 92 steel, many researchers have investigated the creep properties of ferritic-martensitic (FM) steels [11-18]. Therefore, the focus of this work is to investigate microstructural stability and associated mechanical properties in Grade 92 steel. Thus, the microstructural stability as a result of tempering at different temperatures (560, 660 and 760°C) for different times (10, 100 and 1000 h) will be studied along with analyzing their effects on the mechanical properties in terms of hardness and tensile data will be assessed.

4.2.Experimental procedure

The experimental material was procured from the Tianjin Tiangang Weiye Steel Co., China in the form of cylindrical bars with a diameter of 14 mm and has the nominal composition as shown in Table 4.1. The procured steel was normalized at a temperature between 1040-1080°C and tempered at a temperature between 730-800°C according to the ASTM A182 standard. Also, the steel was in F92 condition in accordance with the ASTM A182.

The heat treatment schedule was set as follows: Austenitizing was conducted at 1050°C for 3 h followed by air cooling (normalizing); and then tempering was carried out at different temperatures (560, 660 and 760°C) for different time periods (10, 100 and 1000 h).

The mechanical properties were evaluated via tensile testing and microhardness. Therefore, the tensile testing of the tempered samples was conducted at room temperature and 10^{-3} s^{-1} strain rate using an Instron universal tester, model no. 5982. Before the tensile testing, strips of the as-received bar were cut and heat treated according to the set heat treatment schedules. After that, the tensile specimens were machined out of these strips with a gage diameter of 6.4 mm and a gage length of 25.4 mm. On the other hand, a LECO LM100 microhardness tester was used to evaluate the hardness of the investigated steel with the application of 0.5 kg-force (4.91 N) load for 15 s.

The relevant microstructure was revealed following standard metallographic procedures of grinding and polishing. After the grinding steps, water-based polycrystalline diamond suspensions of 3, 1 and 0.5 μm were used to obtain a mirror-like polished surface before etching. The surface etching was conducted using the Marble's reagent containing 50 ml hydrochloric acid, 10 g of copper sulfate and 50 ml of distilled water.

The TEM samples were prepared by punching out 3 mm disks from a thin foil (~60 μm). Thereafter, jet polishing was conducted using a Fischione twin-jet polisher in low temperature environment (around -40°C) generated by a dry ice bath. Jetpolishing was conducted using a solution of 20 vol.% nitric acid and 80 vol.% methanol.

JEOL JEM-2010 Transmission Electron Microscope (TEM) operated at an accelerating voltage of 200 kV and TF30-FEG TEM with STEM mode operated at an accelerating voltage of 300 kV were employed to conduct the TEM study. Particles were identified using the energy dispersive X-ray spectroscopy (EDS) technique utilizing the STEM mode available on TF30-FEG TEM. The dislocation density of investigated samples was estimated while samples were oriented in a two-beam condition; for that purpose, the electron energy loss spectrum (EELS) technique was applied to estimate the sample thickness.

Table 4.1. The chemical composition of the as-received Grade 92 steel.

Element	**Composition (wt%)**
C	0.09
P	0.015
S	0.001
Mo	0.55
V	0.19
N	0.045
Ni	0.12
W	1.66
B	0.003
Cr	8.68
Mn	0.42
Si	0.34
Al	0.02
Nb	0.079
Fe	Bal .

4.3.Results and discussion

4.3.1. Mechanical properties of the as-received and tempered Grade 92 steel

4.3.1.1.Tensile flow properties

The engineering stress-strain curve for the as-received Grade 92 steel at room temperature and a strain rate of 10^{-3} s^{-1} is shown in Figure 4.1. The as-received Grade 92 steel had a yield strength and an ultimate tensile strength of 1063 and 1385 MPa, respectively. The ductility was estimated to be ~19%.

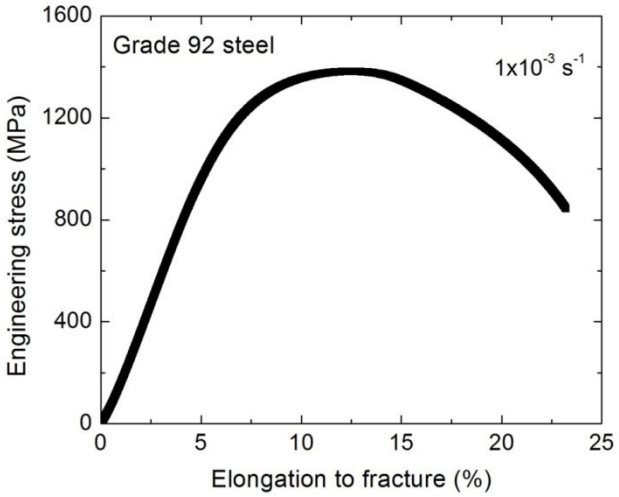

Figure 4.1. The engineering stress-strain curve for the as-received Grade 92 steel at room temperature and a strain rate of 10^{-3} s^{-1}.

For tempered conditions, the investigated samples were austenitized at 1050°C for 3 h and tempering was conducted at different temperatures of 560, 660 and 760°C for different times of 10, 100 and 1000 h. The variation in the tempering temperature and time was introduced to allow different stages of martensite recovery and dislocation density. For instance, the reduction in dislocation density enhanced by the recovery process occurs during tempering along with the formation of subgrains and dislocation networks.

The mechanical properties of tempered Grade 92 steel samples were evaluated. Figure 4.2 shows the engineering stress-strain curves of the steels. Strength decreased as tempering temperature or tempering time increased caused by the recovery process during tempering. However, the condition of the tempered steel at 560°C for 1000 h was not consistent with this trend. The microstructural evolution of the tempered conditions will be investigated to give more insight on the obtained results.

The tensile properties of Grade 92 steel for different tempering conditions are summarized in Table 4.2. The yield strength decreased as tempering time increased from 10 h to 100 h when tempering at 560°C. Increasing the tempering time at 560°C from 100 h to 1000 h unpredictably caused a gain in strength (S_y, S_u and S_f). The temping of the investigated steel, also, showed gradual decrease as time increased when tempering was conducted at 660°C. Lastly, more reduction in strength was obtained after tempering the investigated material at 760°C. The ductility showed a gradual increase as tempering temperature increased.

Table 4.2. The room temperature tensile properties of Grade 92 steel for different tempering conditions.

Condition	S_y (MPa)	S_u (MPa)	S_f (MPa)	*%EL*
10 h at 560°C	990	1105	629	17.9
100 h at 560°C	867	977	593	18.6
1000 h at 560°C	977	1083	638	16.6
10 h at 660°C	785	885	519	20.1
100 h at 660°C	642	750	418	22.9
1000 h at 660°C	480	619	320	26.8
10 h at 760°C	478	617	328	30.0
100 h at 760°C	387	572	304	32.9
1000 h at 760°C	454	503	263	31.1

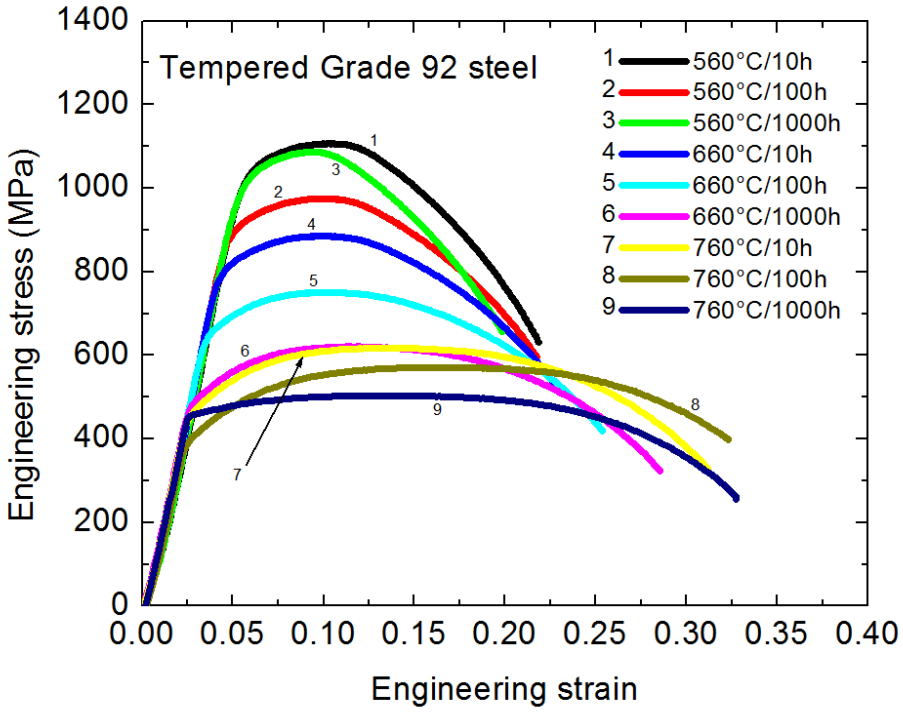

Figure 4.2. Engineering stress-strain curves of tempered Grade 92 steel samples.

4.3.1.2.Microhardness testing

Table 4.3 shows the results of the Vickers microhardness testing in Grade 92. In this table, the as-received, normalized and tempered conditions were compared. The hardness data dropped with increasing tempering temperature and time except one condition, tempered sample at 560°C for 1000 h, which comes in good agreement with the tensile testing results. Tempering enhances the recovery of the martensite structure after normalization which leads to the reduction in dislocation density and subgrain formation. Therefore, at higher tempering temperature, the recovery process accelerates which deteriorates the strength of the steel. The induced microstructural evolution during tempering will be discussed on later sections.

Table 4.3. The Vickers microhardness results for all condition of Grade 92 steel.

Condition	Avg.
As-received sample	397.0±1.6
Normalized sample	420.2±3.1
Tempered samples	
10 h at 560°C	343.4±2.2
100 h at 560°C	309.3±1.5
1000 h at 560°C	334.6±1.3
10 h at 660°C	294.6±1.9
100 h at 660°C	251.2±2.0
1000 h at 660°C	181.4±2.1
10 h at 760°C	195.2±1.0
100 h at 760°C	182.8±1.0
1000 h at 760°C	133.4±2.0

4.3.2. Microstructural evolution in normalized and tempered Grade 92 steel

4.3.2.1.The normalized condition in Grade 92

Figure 4.3 shows the microstructure of the normalized sample for 3 hours at 1050°C. Generally, the microstructure of the normalized in similar steels is composed of PAGB subdivided into block and packets. However, it was complicated to estimate the grain size of the prior austenite grains with the obtained microstructure. The fine microstructure shows a high dislocation density within the martensitic lath structures with an estimated lath width of 176±9 nm.

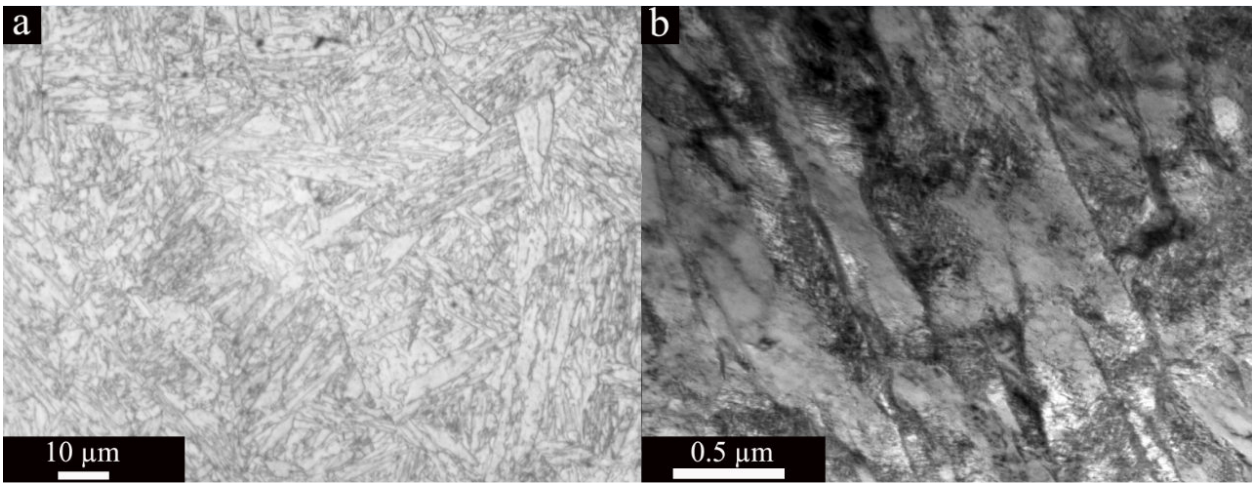

Figure 4.3. The normalized condition microstructure (a) optical micrograph and (b) bright-field TEM image of the normalized Grade 92 steel.

4.3.2.2.Tempering at 560°C:

Tempering of the normalized Grade 92 steel was conducted at different temperatures and times in order to investigate the microstructural evolution and relate it with the mechanical properties. Figure 4.4 shows the TEM images from the Grade 92 steel tempered at 560°C for 10 h. The lath structure was pronounced and the lath width was estimated to be 181±14 nm after tempering at 560°C for 10 h. The dislocation density of the tempered samples at 560°C for 10 h was estimated as (5.7±0.2) × 10^{13} m^{-2}, which was (3.9±0.8) × 10^{14} m^{-2} for the as-received condition. This tempering condition did not show any spherical carbide precipitates. However, round shaped MX-type precipitates were detected with an average diameter of ~50 nm as shown in Figure 4.4. The formation of $M_{23}C_6$ carbides as thin films along the lath boundaries was observed as shown in Figure 4.4a. A similar observation was made by Dudko *et al.* [19] where $M_{23}C_6$ carbides was formed as an extended thin films along the PAGB and lath boundaries when P92 steel was tempered at 525°C for 3 h. The formation of $M_{23}C_6$ carbides as thin films occurs as a result of carbon segregation in martensite where Cr fraction in these films is high [20]. During the tempering process of the

9-12% Cr steels, the carbide transformation occurs according to the following reaction [20-21]:

$$M_3C \rightarrow M_7C_3 \rightarrow M_{23}C_6 \quad (4.1)$$

The first part of the reaction involves the transformation of M_3C, has an orthorhombic structure, to M_7C_3, which is believed to occur as a result of an independent nucleation process based on the fact that these two carbides have different iron and chromium content [20-22]. Therefore, this difference suggests that the diffusion of chromium from martensite enhances the internal rearrangement of cementite lattice [20-21]. The M_7C_3 is less stable than the other carbides ($M_{23}C_6$); therefore, it dissolves during the formation of the more stable carbide $M_{23}C_6$ [20-22]. On the other hand, there is a second mechanism of carbide transformation (i.e. M_7C_3 to $M_{23}C_6$), which occurs through an independent nucleation process involving rearrangement of M_7C_3 lattice into the lattice of face-centered cubic $M_{23}C_6$ [20-22]. However, during the early stages of the $M_{23}C_6$ carbide formation, the carbide formation occurs according to the following reaction [20-21]:

$$M_{23}C_6^{film} \rightarrow M_{23}C_6^{round}. \quad (4.2)$$

Hence, the mechanism described in Eqn. 4.2 requires the transformation of $M_{23}C_6$ precipitates along with increase in the iron content in these precipitates.

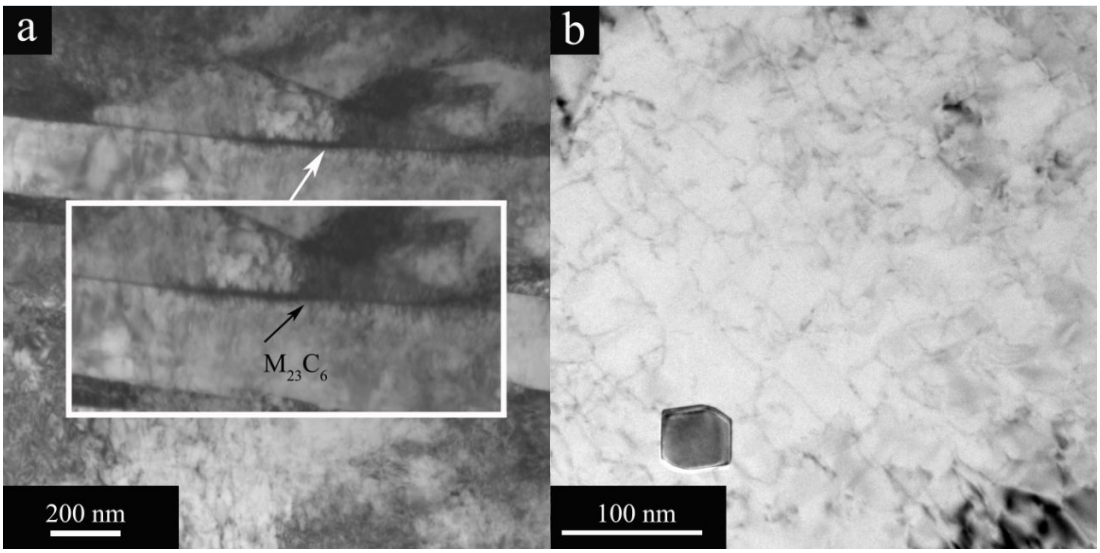

Figure 4.4. The bright-field TEM image of the tempered Grade 92 steel (560°C for 10 h) showing a) extended thin films of $M_{23}C_6$ along the lath boundaries and b) MX-type precipitates within a lath.

Tempering of Grade 92 steel for 1000 h at 560°C highlights an interesting result. When the tempering time was increased from 10 to 100 h at 560°C, the yield strength dropped from 990 to 867 MPa. However, the strength increased again after tempering for 1000 h to 977 MPa. The same behavior was obtained using the microhardness data as shown in Table 4.3. In order to correlate the mechanical properties of the investigated steel, the microstructural evolution of the tempered sample for 1000 h at 560°C will be investigated in depth to study the effect of long tempering time on the mechanical properties at 560°C.

The dislocation density of the tempered sample at 560°C for 1000 h was estimated as $(4.6\pm0.4) \times 10^{13}$ m^{-2}. The microstructure of the tempered Grade 92 steel tempered at 560°C for 1000 h is shown in Figure 4.5. The dark field image of this tempered steel shown in Figure 4.5a clearly illustrates the carbide thin films formed along the lath boundaries, which was detected after tempering the steel for 10 h earlier. Moreover, rectangular-shape particles as shown in Figure 4.5b were found along the boundaries, these particles were much brighter as shown in Figure 4.5a. The MX particles, on the other hand, were distributed

randomly within the martensite laths and they show good coarsening resistance as they maintained their size around 50-60 nm.

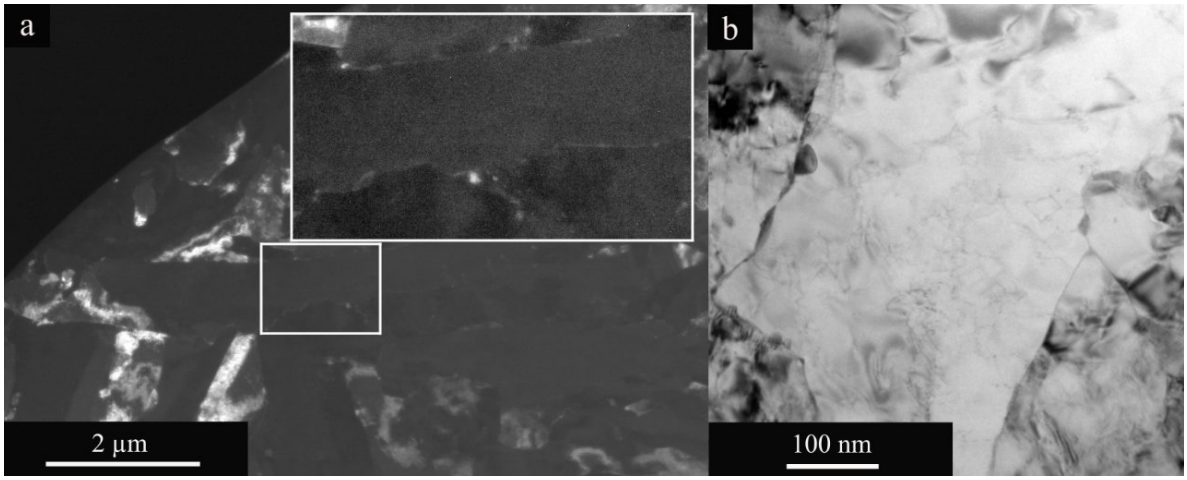

Figure 4.5. The TEM of the tempered condition at 560°C for 1000 h showing a) a dark-field image at low magnification and b) a bright-field TEM image showing the carbide formation in the form of film and rectangular-shape particles.

According to Thermo-Calc calculations for 9Cr-2W steel, the nucleation of new phase (i.e. Laves phase $\{(Fe,Cr)_2(Mo,W)\}$) occurs at a temperature lower than 720°C after a long tempering time [19]. Above 720°C, Laves phase dissolves in the matrix [19]. The Laves phase can be detected using the backscattered electron mode in an SEM where Laves phase particles look brighter since these particles contain elements (W and Mo) having large atomic numbers and they segregate, preferentially, on PAGBs and lath boundaries. Using the bright field TEM imaging mode, Laves phase are present as dark rectangular particles with one side connected to the boundary [23-24]. At the early stages of Laves phase nucleation, they are distributed inhomogeneously at the lath boundaries where they preferentially nucleate. The Laves phase nucleation can occurs as a result of the segregation of strengthening elements (i.e. such as W and Mo) along the boundaries after long tempering period which causes the beginning of Laves phase precipitation when these boundaries become highly condensed at certain tempering temperatures [23-24]. Also, the nucleation of

Laves phase occurs as a result of growing on $M_{23}C_6$ particles as nucleation sites which facilitate the Laves phase formation [23-24].

For that reason, the EDS spectra of the observed rectangular-shape particles, when sample was tempered at 560°C for 1000 h, was carried out as shown in Figure 4.6. These particles were identified as Laves phase particles via EDS as shown in Figure 4.6 as these particles are Fe, Cr, W and Mo enriched particles. The induced strengthening effect by Laves phase has also been observed by Abe *et al.* [7] and Lee *et al.* [12]. Once Laves phase particles are formed, the deterioration associated with drawing out Mo/W from solid solution can be compensated by the precipitation strengthening at an early stage of precipitation of Laves phase particles. However, Laves phase particles possess high coarsening rate so their beneficial effect diminishes at higher temperatures and/or under loading where microstructural evolution accelerates. For that reason, the induced strengthening by the formation of Laves phase, in the early stages, could compensate for the loss in solid solution strengthening of 9-12% Cr steels.

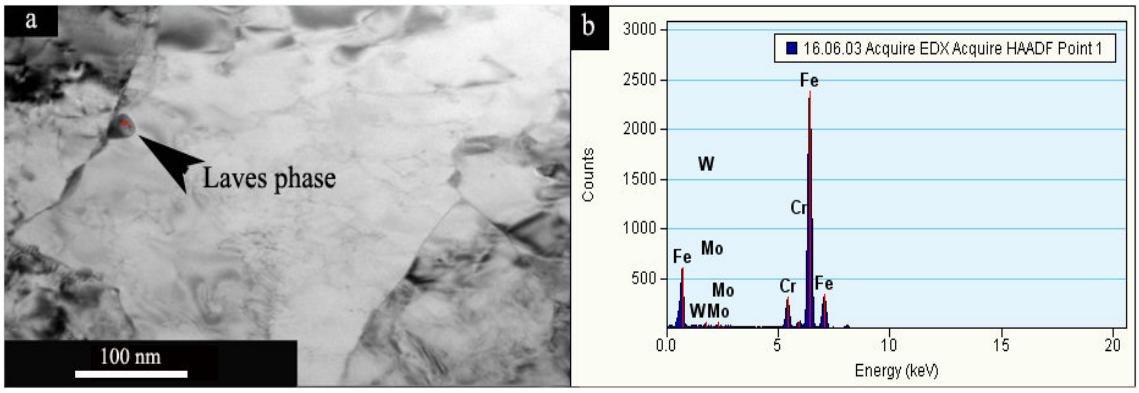

Figure 4.6. The tempered condition at 560°C for 1000 h showing (a) bright-field TEM image showing the carbide formation in the form of film and rectangular-shape Laves phase particles and (b) The EDS spectra of Laves phase.

In conclusion, tempering was conducted at 560°C for 10, 100 and 1000 h, and the corresponding yield stress values were 990, 867, 977 MPa, respectively. The higher strength

of the tempered samples at 560°C can be mainly attributed to the maintained martensitic lath structure, dislocation hardening and the induced precipitation strengthening. The MX particles were distributed randomly when tempering at 560°C within the martensite laths and they showed good coarsening resistance. The formation of $M_{23}C_6$ carbides occurred as thin films along the lath boundaries at the early stages of tempering, after 10 h.

After tempering for long time 1000 h, strength has increased. The evolution of the Laves phase after long tempering period (1000 h) enhanced the steel strength which explains the gain in strength after tempering for 1000 h. The ductility of the tempered samples at 560°C was lower than other tempering temperatures which might be attributed to the formation of the carbide thin film which induces tempering brittleness [20]. That is why the lower ductility values were obtained at the tempering temperature of 560°C.

4.3.2.3.Tempering at 660°C:

As tempering temperature was raised to 660°C, the microstructure of the tempered sample after 10 h showed a pronounced lath structure with an early stage of subgrain boundary formation, as shown in Figure 4.7a. But, the regular martensitic lath structure observed at 560°C did not show any well formed subgrains. Precipitation of $M_{23}C_6$ was detected along the lath boundaries and PAGBs, as shown in Figure 4.7b. The observed $M_{23}C_6$ carbides after tempering the steel at 660° for 10 h were found as round shaped particles (diameter of around 36 nm) and were also detected as plate-like particles (65±6 nm in length and 16±2 nm in width) at the lath boundaries, as shown in Figure 4.7b. Hence, it is clear that these carbides replaced the earlier formed thin carbide film at the boundaries. At higher tempering temperature, $M_{23}C_6$ formation occurs as result of the occurrence of two

concurrent processes; the transformation of the formed thin carbide film into more equiaxed particles and independent precipitation of round $M_{23}C_6$ particles; where the latter mechanism is more dominant [19-20]. The dual $M_{23}C_6$ carbide precipitation mechanism was reported at tempering temperatures close to 650°C (i.e. at 625°C for 3 h) wherein the $M_{23}C_6$ formation was reported both in equiaxed and plate-like shapes [19-20].

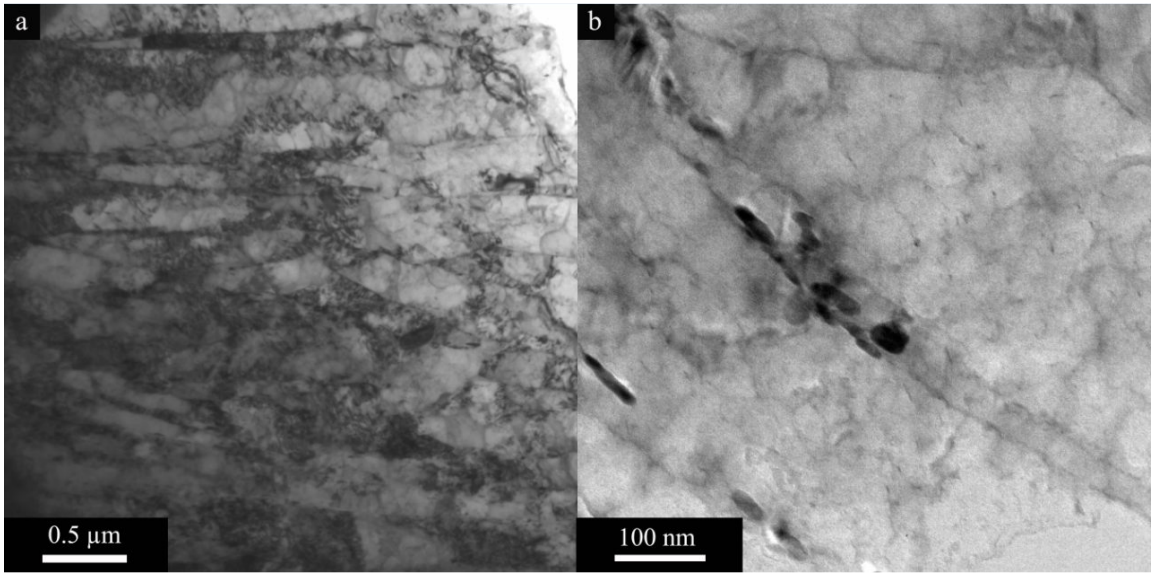

Figure 4.7. TEM images of the tempered Grade 92 steel tempered at 660°C for 10 h showing a) the lath structure and b) $M_{23}C_6$ precipitation along the lath boundaries.

For the sample tempered at 660°C for 1000 h, the lath widening becomes more evident, as shown in Figure 4.8a. For instance, the lath width increased from 214.5±13.0 nm (i.e. at 660°C for 10 h) to 396.1±23.2 nm (1000 h at 660°C). During heat treatment of the martensitic structure, the relatively small laths tend to shrink in width and eventually disappear, whereas the larger laths get wider [27]. This mechanism is driven by the accumulated strain generated during the martensitic transformation, which provides the driving force for the process [24, 27].

The lath boundary migration was believed to depend on $M_{23}C_6$ carbides; thus, $M_{23}C_6$ carbides decorating the lath boundaries are larger than the other MX precipitates so that the

migrating lath boundary will travel toward the inside of the adjacent lath rather than crossing $M_{23}C_6$ carbides [27]. At that time, the migrating lath boundary will cross the small size MX particles which can be much easier to overcome [24, 27]. Finally, the migration of the lath boundary will come to an end when it reaches other obstacles such as another lath boundary, $M_{23}C_6$ carbides or PAGBs [24, 27]. This can be clearly seen in Figure 4.7b where the bulging of lath boundaries were stopped by the carbide precipitation where the inner lath bulk (i.e. lath on the middle) shows the precipitation on the inner two sides of the middle lath allowing it to retain very small width.

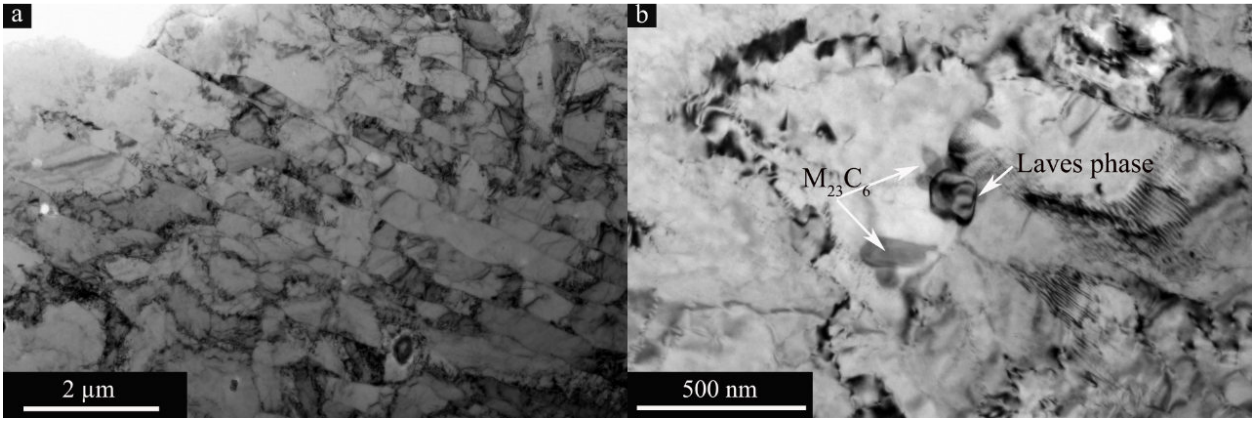

Figure 4.8. The TEM images of the tempered Grade 92 steel tempered at 660°C for 1000 h showing a) lath structure and b) precipitates of $M_{23}C_6$ carbides and Laves phase.

The equiaxed $M_{23}C_6$ particles after tempering at 660°C for 1000 h coarsened noticeably. Thus, they were found to occur with an average size of around 61 nm. Also, the plate-like $M_{23}C_6$ particles were detected with 176±29 nm in length and 54±7 nm in width, Figure 4.8b.

During the investigation of precipitates for this condition (660°C for 1000 h), special attention was devoted to detect the Laves phase particles. For instance, the rectangular Laves phase particles evolve at temperatures lower than 720°C after long tempering time. Therefore, Laves phase particles were detected at sizes around 180 nm which would contribute to the significant drop in strength for this specific condition, Figure 4.8b. The

Laves phase deteriorates the strength of the steel via the associated weakening of solid solution strengthening. That is why, the Laves particles are not desirable for two reasons: 1) The induced reduction in solid solution strengthening as a result of W and Mo segregation from the matrix to the Laves phase, and 2) its high coarsening rate which weakens the solid solution strengthening rapidly before they act as cavity trigger, especially at a size of around 130 nm [24, 28-29].

The subgrain formation was more pronounced after tempering the steel at 660°C for 1000 h. While the tempered sample at 660°C for 10 h showed an early stage of the subgrain evolution, the formation of the subgrains progressed after tempering at 660° for 1000 h, Figure 4.9. Hence, the induced subgrain grow at this condition enhances softening of the tempered steel.

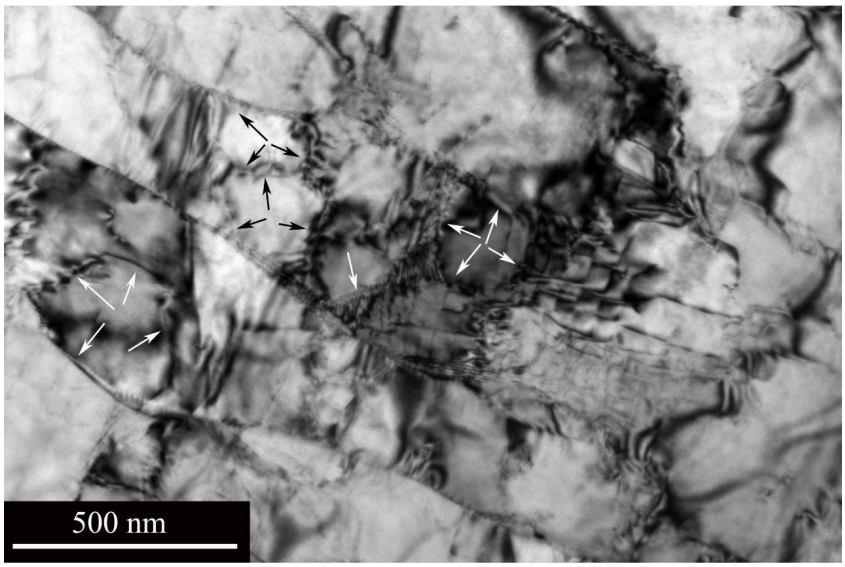

Figure 4.9. The TEM images of the tempered Grade 92 steel tempered at 660°C for 1000 h showing the formation of subgrains within the laths.

In conclusion, tempering was conducted at 660°C for 10, 100 and 1000 h and the corresponding yield stress values were 785, 642, 480 MPa, respectively. The precipitation of the strengthening precipitates $M_{23}C_6$ and MX-type particles was observed. Also, the Laves

phase which precipitates after long tempering times was detected after tempering for 1000 h. The high coarsening rate of the $M_{23}C_6$ and Laves phase weakens the solid solution strengthening. Also, the formation of the subgrains which progressed noticeably after 1000 h enhances the softening of the tempered steel.

As tempering enhances the ductility, the ductility increased after the tempering temperature was increased from 560°C to 660°C. Moreover, the ductility increased as tempering time was increased at 660°C. Thus, the maximum ductility was found after tempering the steel for 1000 h which was attributed to the induced softening and to the more homogenous deformation as a result of the progressed subgrain formation.

4.3.2.4.Tempering at 760°C:

As the tempering temperature was increased to 760°C, the microstructure changed substantially, as shown in Figure 4.10. For instance, the subgrain formation was more pronounced within the bulk of the laths and the $M_{23}C_6$ carbide precipitation was more noticeable, as shown in Figure 4.10a. The MX-type particles within the laths, as shown in Figure 4.10b, maintained their size around 50 nm which comes in good agreement with the reported in literature [19, 30]. The equiaxed round and plate-like $M_{23}C_6$ carbides were detected and their coarsening was obvious. For example, the equiaxed round $M_{23}C_6$ carbides at 760°C for 10 h had a diameter of around 130 nm whereas the plate-like $M_{23}C_6$ carbides had a length of ~ 270 nm and width ~ 170 nm, as shown in Figure 4.10b. The detectable coarsening of these $M_{23}C_6$ carbides reduces their efficiency in pinning the boundaries at higher diameters (more than 200 nm). The $M_{23}C_6$ precipitates in contact with the subgrain boundaries coarsened more than other carbides which lost contact with the boundaries due to the

subgrain growth, as shown in Figure 4.10b. This behavior was also observed by Eggeler since the pipe diffusion will be enhanced along the boundaries of the subgrains [31]. Therefore, the coarsening of $M_{23}C_6$ carbides will enhance the dislocation movement leading to subgrain formation and subgrain growth.

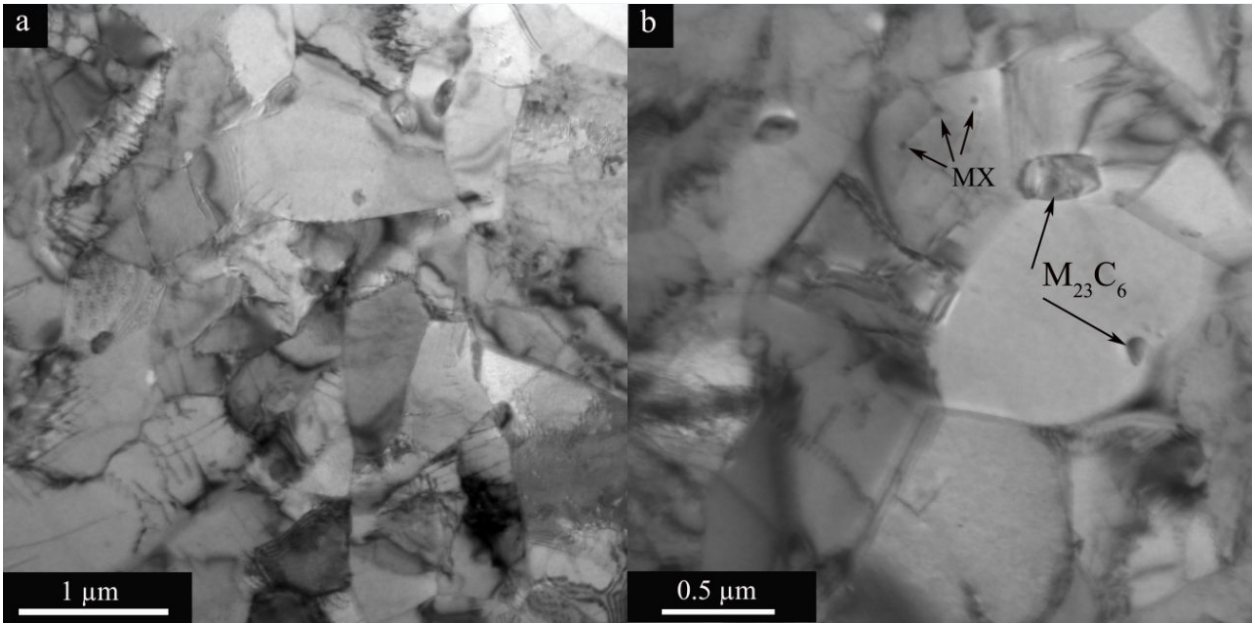

Figure 4.10. TEM images of the tempered Grade 92 steel at 760°C for 10 h showing a) the pronounced subgrain formation within the lath structure and b) MX particles within the laths, and round and plate-like $M_{23}C_6$ carbides.

When tempering the samples at 760°C for 10 h, subgrains with more than 1 μm diameter were observed. The formation of subgrains within the martensitic laths was promoted by the higher tempering temperature [24, 32]. The higher tempering temperature promotes the dislocation movement and interaction with one another which induces polygonization of the dislocation walls into well-defined subgrain boundaries as illustrated in Figure 4.11 [24, 32]. Because of the small size of the MX particles (~50 nm), it is believed that the $M_{23}C_6$ particles play a dominant role in controlling the formation and growth of subgrains. For example, the $M_{23}C_6$ particles precipitate along the boundaries which enhance the sub-

boundary stabilization and provide the needed pinning effect as long as they maintain an effective pinning size up to about 150 nm.

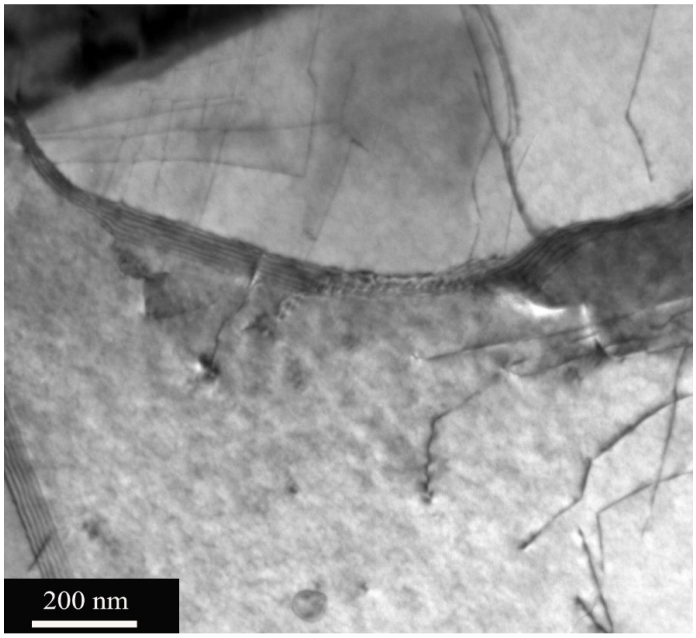

Figure 4.11. Aligned walls of dislocations interacting to form subgrain boundaries.

The TEM images of the Grade 92 steel tempered at 760°C for 1000 h is shown in Figure 4.12. The subgrain formation at 760°C for 1000 h was more pronounced. Thus, subgrains with diameters more than 2 μm were observed as shown in Figure 4.12a. The volume fraction of the $M_{23}C_6$ carbide was much less than the shorter tempering time at the same temperature (760°C for 10 h). Still, the $M_{23}C_6$ particles substantially coarsened, as shown in Figure 4.12b, around 650 nm in diameter. On the other hand, no Laves phase was detected as these particles are not expected to form above 720°C because they dissolve back in the matrix (i.e. the solubility temperature for this phase) [19]. The MX particles showed good coarsening resistance (~55 nm) even after tempering the sample for 1000 h for 760°C as depicted in Figure 4.13. Similar coarsening resistance of these particles (MX-type) has been noted even after long elevated temperature exposure during creep deformation [2, 34].

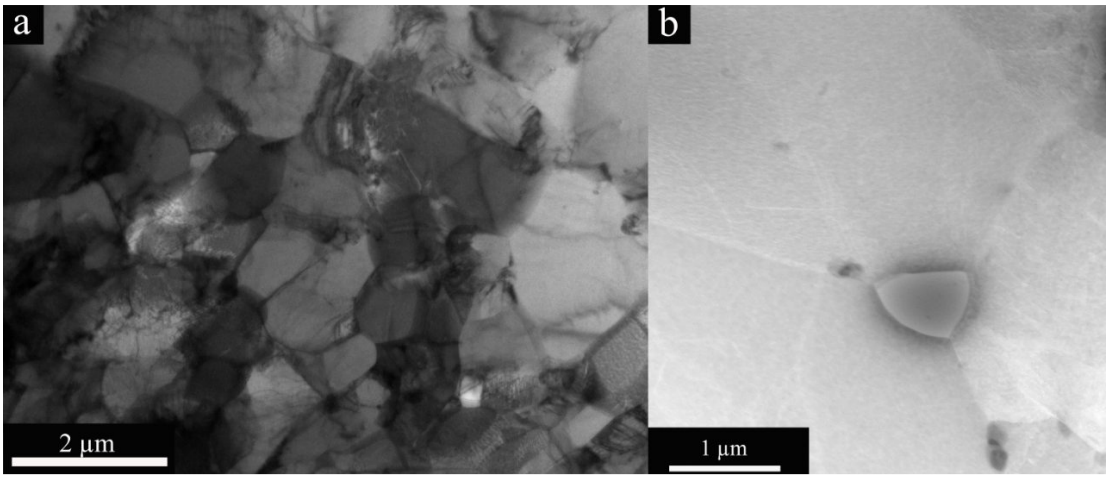

Figure 4.12. The TEM images of the Grade 92 steel tempered at 760°C for 1000 h showing a) the pronounced subgrain formation (bright field mode) and b) $M_{23}C_6$ carbides (in STEM mode).

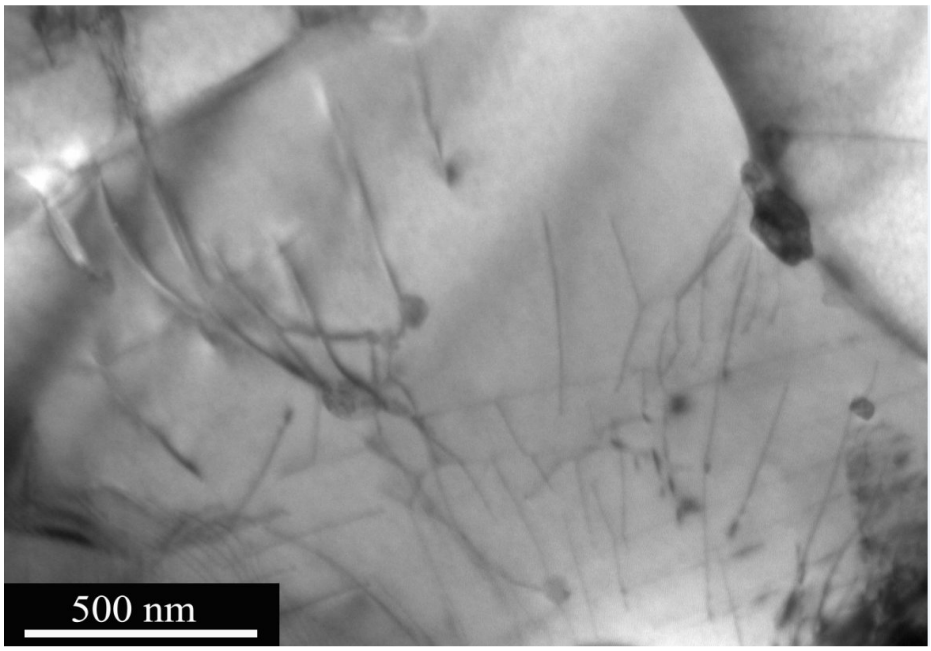

Figure 4.13. The MX-particles after tempering of the Grade 92 sample at 760°C for 1000 h.

The mechanical properties (tensile and hardness) showed the lowest ranges at this tempering temperature, 760°C. For instance, the $M_{23}C_6$ particles coarsened significantly which deteriorated the precipitation hardening drastically. Moreover, the subgrain formation during highest tempering temperature (760°C) indicated higher dislocation mobility which

led to the reduction in dislocation density. Thus, the subgrain formation enhanced the steel softening resulting from the movement of dislocations within the bulk of laths through recovery process [7]. On the other hand, the ductility, on this specific tempering temperature, scored the highest among other tempering temperatures which can be attributed to the enhanced softening and associated homogeneous deformation as a result of the progressed subgrain formation.

4.3.3. Evaluation of Hollomon-Jaffe parameter in Grade 92 steel

The tempering of steels influences mechanical properties greatly. While, the temperature has more influence in the reduction of hardness and residual stresses, the soaking time must be considered. That is why the Hollomon-Jaffe parameter incorporates the effect of both tempering temperature and time according to the following equation [35-36]:

$$P = T(C + \log t) \tag{4.3}$$

where P is the Hollomon-Jaffe parameter, T is temperature in K, C is the Hollomon-Jaffe constant and t is time in s.

The Hollomon-Jaffe constant depends solely on the carbon content in steel and can be estimated according to [35]:

$$C = 21.3 - (5.8 \times wt\%\ Carbon) \tag{4.4}$$

Here, the Hollomon-Jaffe parameter for Grade 92 steel was calculated to be 20.8. Figure 4.14 was constructed to show the degree of tempering as a function of both tempering temperature and time where the associated fitting coefficient was more than 0.96 for the investigated steel. The obtained results fit well with the data obtained by Dudko *et al.* [19]

who investigated the P92 steel after tempering for 3 hours at temperatures between 525-720°C.

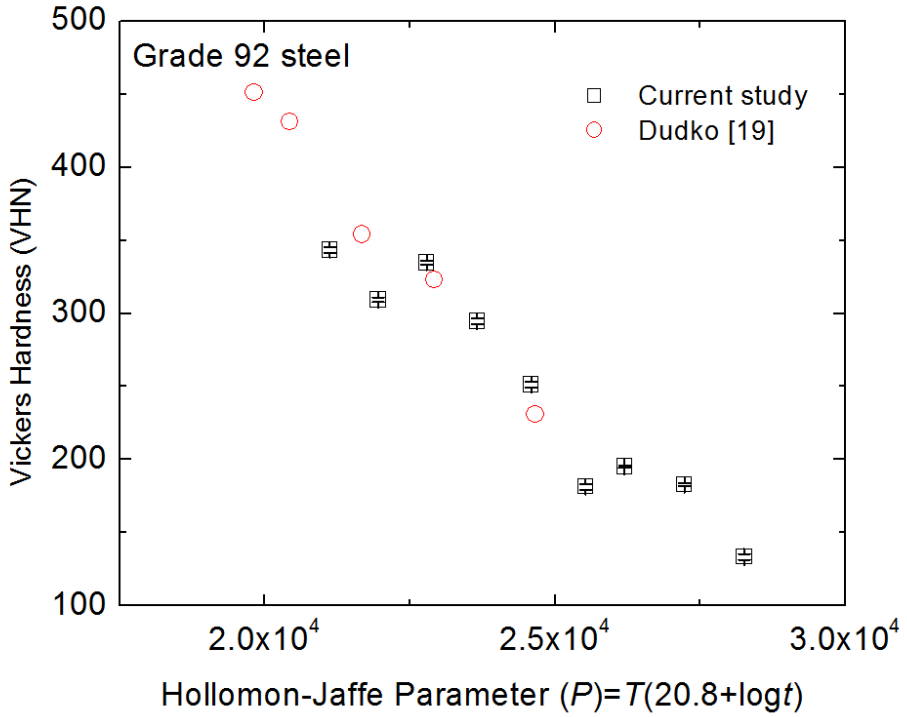

Figure 4.14. The Hollomon-Jaffe Parameter for the Grade 92 steel.

4.4.Conclusion

The thermal stability and mechanical properties of Grade 92 steel were evaluated. Normalizing was conducted at 1050°C for 3 h and schedule sets of tempering were carried out at 560, 660 and 760°C for 10, 100 and 1000 h. The following conclusions can be established:

1- After tempering the sample at 560°C, the $M_{23}C_6$ carbide formation along the prior austenite grain boundaries and lath boundaries caused tempering brittleness, leading to the lowest ductility among all tempering temperatures.

2- The strength values after tempering the sample at 560°C dropped after increasing the time from 10 h to 100 h. However, the strength increased again after increasing the time from 100 to 1000 h which was attributed to the secondary hardening effect and the strengthening effect induced by the Laves phase.

3- The $M_{23}C_6$ carbides precipitation after tempering at 660°C occurred as round shaped particles and plate-like particles. The carbide coarsening was observed and progressive strength reduction occurred as the tempering time was increased.

4- During the tempering at 660°C, subgrain formation within the laths and lath widening process were more pronounced and progressed as tempering times increases.

5- After tempering at 760°C, the subgrain formation was dominating the investigated microstructure along rapid carbide coarsening; however, MX-type particles showed good coarsening resistance.

6- The Hollomon-Jaffe constant which depends on the carbon content on steel was estimated as 20.8 and Hollomon-Jaffe parameter (P) fits well the hardness data.

References

[1] A. Czyrska-Filemonowicz, A. Lipiec, P.J. Ennis, J Achievements Mater. Manuf. Eng., 19 (2006) 43-48.

[2] P.J. Ennis, A. Zielinska-Lipiec, O. Wachter, A. Czyrska-Filemonowicz, Acta Mater., 45 (1997) 4901-4907.

[3] R.L. Klueh, Int. Mater. Rev., 50 (2005) 287-310.

[4] F. Masuyama, Int. J. Pres. Ves. Pip., 84 (2007) 53-61.

[5] T. Shrestha, M. Basirat, I. Charit, G. P. Potirniche, K.K. Rink, U. Sahaym, J. Nucl. Mater., 423 (2012) 110–119.

[6] R.L. Klueh, A.T. Nelson, J. Nucl. Mater., 371 (2007) 37-52.

[7] F. Abe, Strengthening mechanisms in creep of advanced ferritic power plant steels based on creep deformation analysis, in: Y. Weng, D. Hand (Eds.). Advanced Steels: The Recent Scenario in Steel Science and Technology, Metallurgical Industry, Beijing, 2011, pp. 409-22.

[8] C. Panait, W. Bendick, A. Fuchsmann, A.-F. Gourgues-Lorenzon, J. Besson, Int. J. Press. Vess. Pip., 87 (2010) 326–335.

[9] L. Korcakova, J. Hald, Mater. Charact., 47 (2001) 111-117.

[10] M. Yurechko, C. Schroer, A. Skrypnik, O. Wedemeyer, J. Konys, J. Nucl. Mater., 432 (2013) 78-86.

[11] V. Sklenicka, K. Kucharova, M. Svoboda, L. Kloc, J. Bursik, A. Kroupa, Mater. Charact., 51 (2003) 35-48.

[12] J.S. Lee, H.G. Armaki, K. Maruyama, T. Muraki, H. Asahi, Mater. Sci. Eng. A, 428 (2006) 270-275.

[13] L. Kloc, V. Sklenicka, Mater. Sci. Eng. A, 234 (1997) 962–965.

[14] B.K. Choudhary, E.I. Samuel, J. Nucl. Mater., 412 (2011) 82–89.

[15] F. Penalba, X. Gomez, R. Allende, M. Carsi, O. Ruano, Mater. Sci. Forum, 638 (2010) 3128-3133.

[16] F. Dobes, K. Milicka, Metal Sci., 10 (1976) 382-384.

[17] B.K. Choudhary, K.B.S. Rao, S.L. Mannan, Trans. Ind. Inst. Met., 52 (1999) 327-236.

[18] B.K. Choudhary, S. Saroja, K.B.S. Rao, S.L. Mannan, Metall. Mater. Trans., A30 (1999) 2825-2834.

[19] V. Dudko, A. Belyakov, R. Kaibyshev, Mater. Sci. Forum, 706-709 (2012) 841-46.

[20] A.Yu. Kipelova, A.N. Belyakov, V.N. Skorobogatykh, I.A. Shchenkova, R.O. Kaibyshev, Met. Sci. Heat Treat., 52 (2010) 100–110.

[21] S. Kobayashi, K. Toshimori, K. Nakai, Y. Ohmori, H. Asahi, T. Muraki, ISIJ Int., 42 (2002) S72 – S76.

[22] K. Maruyama, K. Sawada, J.-I. Koike, ISIJ Int., 41(6) (2001) 641 – 653.

[23] K. Sawada, M. Takeda, K. Maruyama, R. Ishii, M. Yamada, Y. Nagae, Mater. Sci. Eng. A, 267(1) (1999) 19–25.

[24] W. Yan, W. Wang, Y. Shan, K. Yang, Front. Mater. Sci., 7 (1) (2013) 1–27.

[25] R.W.K. Honeycombe, H.K. Bhadeshia, Steels: Microstructure and Properties, second ed., Edward Arnold, London, 1995.

[26] S. Wei, Steels: From Materials Science to Structural Engineering, first ed., Springer, London, 2013.

[27] K. Sawada, M. Taneike, K. Kimura, F. Abe, Mater. Sci. Technol., 19 (2003) 739–742.

[28] P. Hu , W. Yan, W. Sha, W. Wang, Z. Guo, Y. Shan, K. Yang, Front. Mater. Sci. Chin, 3 (2009) 434–441.

[29] J. S. Lee, H. G. Armaki, K. Maruyama, T. Muraki, H. Asahi, Mater. Sci. Eng. A, 428 (2006) 270–275.

[30] C. Panait, A. Zielinska-Lipiec, T. Koziel, A. Czyrska-Filemonowicz, A.F. Gourgues-Lorenzon, W. Bendick, Mater. Sci. Eng. A, 527 (2010) 4062–4069.

[31] G. Eggeler, Acta Met., 37(12) (1989) 3225–3234.

[32] C. Keller, M.M. Margulies, Z. Hadjem-Hamouche Z.I. Guillot, Mater. Sci. Eng. A, 527 (2010) 6758–6764.

[33] A. Kostka, K.G. Tak, R.J. Hellmig, Y. Estrin, G. Eggeler, Acta. Mater., 55 (2007) 539–550.

[34] A. Aghajani, C. Somsen, G. Eggeler, Acta Mater., 57 (2009) 5093–5106.

[35] G.E. Totten, M.A. Howes, Steel Heat Treatment Handbook, first ed., Marcel Dekker, New York, 1997.

[36] J. Hollomon, L. Jaffe, Ferrous metallurgical design; design principles for fully hardened steel, first ed., Wiley, New York, 1947.

CHAPTER 5: Irradiation-Induced Microstructural Evolution and Hardening in Grade 92 Steel under the Influence of Fe-ion Irradiation

Sultan Alsagabi [a,b], *Indrajit Charit* [a,1]

[a] *Department of Chemical and Materials Engineering, University of Idaho, Moscow, ID 83844, USA*

[b] *Atomic Energy Research Institute, King Abdulaziz City for Science and Technology, P.O. Box 6086, Riyadh 11442, Saudi Arabia*

(*To be submitted to the Journal of Nuclear Materials*)

Abstract

Grade 92 steel (9Cr-2W) is a ferritic-martensitic steel with good mechanical and thermophysical properties. It is being considered for structural applications in advanced nuclear energy systems. Still, the irradiation performance of this alloy is not fully understood as a result of the limited available data. For that purpose, Grade 92 steel was irradiated by self-ion (Fe^{+2}) beam to 10, 50 and 100 dpa. Irradiation experiments were conducted at 30 and 500°C. In general, the sample showed good radiation damage resistance at these irradiation testing parameters. The irradiation-induced hardening was higher at 30°C with higher dislocation densities and the dislocation density was less pronounced at higher temperatures. Moreover, the irradiated samples at 30°C had defect clusters and their density increased at higher doses. On the other hand, dislocation loops were found in the irradiated samples at 50 dpa and 500°C. Lastly, the irradiated samples did not show any bubble or void.

Keywords: 9Cr-2W steel; irradiation performance; irradiation-induced hardening; microstructural evolution; nanoindentation

5.1.Introduction

Ferritic-martensitic (FM) steels possess superior mechanical and thermophysical properties [1-3]. For instance, high temperature and creep strength, high thermal conductivity and low thermal expansion coefficient [3-6]. Also, ferritic-martensitic steels possess low swelling rates. Therefore, ferritic-martensitic steels are being considered for structural applications in the Next Generation Nuclear Plant (NGNP) among other steels [1-7]. Ferritic-martensitic steels, austenitic stainless steels and nickel-base alloys were candidate as structural components in some advanced reactors such as the super-critical water reactor (SCWR) [1, 8-9]. Grade 91, HT9 and Grade 92 are considered as structural components as a result of their superior properties [10-11]. The ferritic-martensitic steels would be less vulnerable to radiation-induced damages such as swelling and transmutation as a result of the minor Ni content in these steels which make these steels more resistant to helium transmutation when exposed to neutron irradiation [10-11]. For that reason, the ferritic-martensitic steel has attracted attention to find applications for applications in the advanced reactors [1, 8-9].

The hardening behavior of ferritic-martensitic steels was lower than other austenitic steels; among these, the FM steel 9Cr-2W had lower hardening than other ferritic-martensitic steels [12]. The radiation damage in ferritic-martensitic steels needs further assessment based on the limited available data. Therefore, evaluation of the radiation-induced damage is crucial to evaluate the irradiation behavior [13]. For instance, the radiation-induced microstructural evolution such as the segregation of main strengthening elements in 9-12% Cr steels (Cr and W) and depletion of Fe in carbides was observed as the dose increased at room temperature [14]. Also, the irradiation induced segregation and

depletion became more severe at higher doses under heavy ion irradiation in 9-12% Cr steels [14].

The irradiation temperature influences the radiation damage in FM steels which consequentially alters the mechanical properties before reaching a saturation stage - the radiation-induced saturation [1, 8]. The irradiation-induced swelling in 9-12% Cr steels generally show low swelling rates. Thus, comparing the swelling rate for some ferritic-martensitic steels showed that they possess low swelling rate and two ferritic-martensitic steels had less than 2% swelling even when irradiated at 200 dpa and 400°C [15]. In addition, the radiation-induced hardening was increasing until reaching 450°C when the irradiation hardening saturates [15]. The irradiation hardening saturation depends solely on both irradiation temperatures and doses; however, the irradiation temperature being the more important factor [16]. For instance, the in-situ irradiation work conducted by Topbasi *et al.* [10] on Grade 92 steel showed that the defect cluster density increases with dose and saturates when reaching around 6 dpa. Also, the low temperature range (~200°C) does not influence either the average size or distribution of irradiation-induced defect clusters at that low temperature range [10]. On the other hand, the irradiation damage assessment at elevated temperatures (between 290-500°C) showed that small carbide re-precipitates and voids were created. Also, the segregation of strengthening elements (Cr and W) in voids was more pronounced at higher temperatures [16].

The irradiation-induced hardening alters the mechanical properties which affect major properties [8, 17]. For that purpose, the irradiation-induced toughness was evaluated qualitatively and irradiation-induced hardening was found to increase the ductile–brittle

transition temperature (DBTT) [8, 17]. However, the Grade 91 ferritic-martensitic steel showed insignificant shifting as a result of irradiation [8, 17].

Ferritic-martensitic steels have the potential to be employed in the advanced reactors; however, in order to assess their feasibility of using, further examination into their irradiation performance of these steels needs to be carried out. The 9Cr-2W steel was considered with more momentous promises to meet some in-core and out-core applications in advanced reactors [18]. In this work, the induced microstructural evolution and corresponding mechanical properties will be investigated at different doses (10, 50 and 100 dpa) and temperatures (30 and 500°C).

5.2.Experimental procedure

5.2.1. Experimental material

The investigated material was procured from the Tianjin Tiangang Weiye Steel Co., China in the form of cylindrical bars with a diameter of 14 mm and has the nominal composition as shown in Table 5.1. The procured steel was in F92 condition in accordance with the ASTM A182 and normalized at a temperature between 1040-1080°C and tempered at a temperature between 730-800°C according to the ASTM A182 standard.

Table 5.1. The chemical composition of the as-received Grade 92 steel.

Element	**Composition (wt%)**
C	0.09
P	0.015
S	0.001
Mo	0.55
V	0.19
N	0.045
Ni	0.12
W	1.66

B	0.003
Cr	8.68
Mn	0.42
Si	0.34
Al	0.02
Nb	0.079
Fe	Bal .

5.2.2. Irradiation by self-ions

Polished samples with mirror-like surface, with 14 mm diameter and 0.7 mm thickness, were obtained following standard metallographic procedures of grinding and polishing. Polishing using water-based polycrystalline diamond suspensions of 3, 1 and 0.5 μm were performed. After that, vibratory polishing was carried out to prepare samples for raster scanning irradiation with iron (Fe^{2+}) ions. For that purpose, IoneX 1.7 MV Tandetron accelerator with SNICS sputter ion source at the Texas A&M Ion Beam Laboratories was used. Irradiation was conducted at two temperatures of 30 and 500°C. Table 5.2 shows the irradiation parameters used in this study.

Table 5.2. The irradiation parameters for raster scanning irradiation using iron (Fe^{2+}) ions and 4MeV for the as-received Grade 92 steel.

Condition	Rastering region (mm^2)	Fluence (ion/cm^2)	Time under irradiation (min.)
10 dpa at 30°C	10×10	5.86×10^{15}	95
50 dpa at 30°C	10×10	2.93×10^{16}	417
100 dpa at 30°C	10×10	5.86×10^{16}	369
10 dpa at 500°C	7×7	5.86×10^{15}	95
50 dpa at 500°C	7×7	2.93×10^{16}	417
100 dpa at 500°C	7×7	5.86×10^{16}	369

At 30°C, samples were attached to an electrically isolated stage by double sided copper tape which can read the beam current directly via a current integrator. At elevated temperature, samples were mounted using a silver paint to a heated stage and temperature was measured by a thermocouple near the edge of the stage and Firestick-type resistance heater was used to heat the samples. The difference between the center and the edge of the stage was controlled precisely and temperature calibration was performed to check if there is any difference. At elevated temperature, stage emits electrons when it is heated and the current cannot be directly measured. As a result of the high stability of the sputter source, a current measurement was taken from the Faraday cup directly in front of the sample stage every ~20 min which gives very accurate results.

In order to extract Fe ions, the sputter ion source is started to maximum power after turning on the ionizer which has a tungsten filament with a ceramic coating. Heating process has to be conducted slowly as the thermal expansion of tungsten relative to the ceramic coating is different. After that, the filament will start producing electrons once the filament is hot. In order to extract the ion species from the target cathode (pure Fe 99.95 %), various voltages are needed. Then, Cs reservoir is heated to allow its vapors to rise into the source head so the Fe ions will begin to be extracted once Cs reservoir has reached proper temperature. Figure 5.1 shows the implantation beam line and the hot stage at the Texas A&M Ion Beam Laboratories.

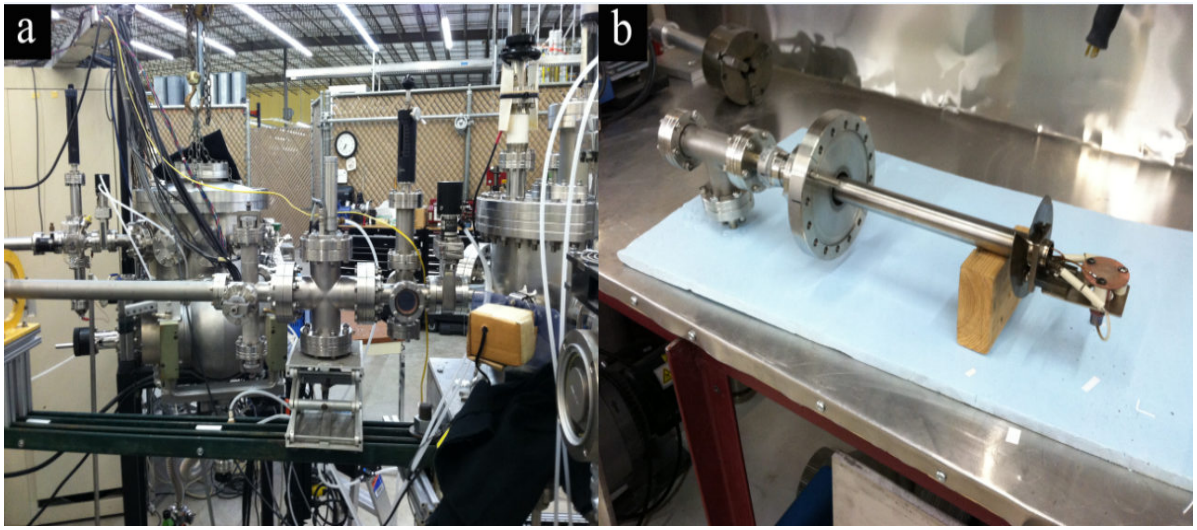

Figure 5.1. The IoneX 1.7 MV Tandetron accelerator at Texas A&M Ion Beam Laboratories showing (a) implantation beam line and (b) the hot stage.

The displacement per atom (DPA) was measured based on peak damage level in sample and a peak damage dose of 10, 50 and 100 dpa were achieved using a the corresponding fluence as shown in Table 5.2. The radiation damage profile (i.e. dpa versus depth) is shown in Figure 5.2 and it was estimated using the Stopping and Range of Ions in Matter (SRIM) 2008.04 software.

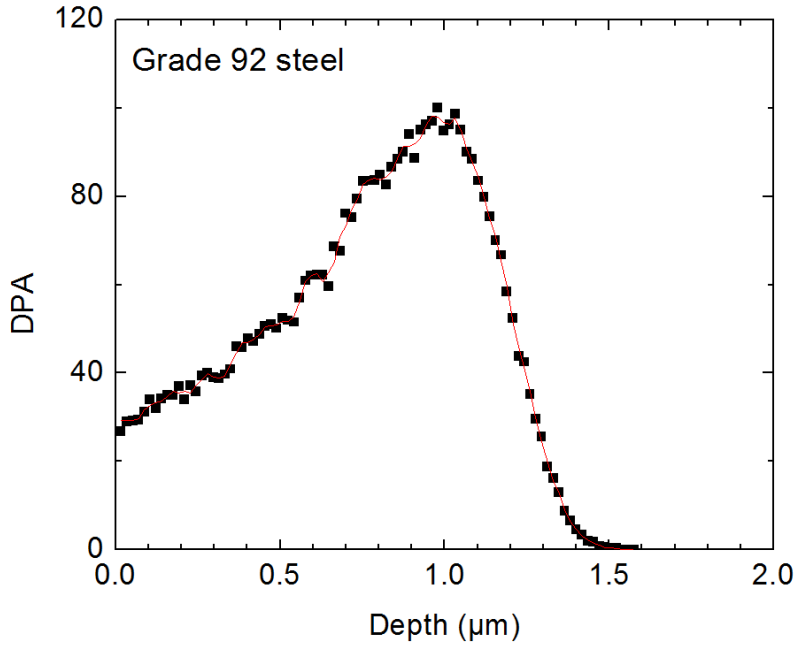

Figure 5.2. The radiation damage profile, displacement per atom (dpa) versus depth.

5.2.3. Microstructural and mechanical characterization

The irradiated samples were prepared for TEM studies using Focused Ion Beam-Scanning Electron Microscope (FIB-SEM) (model Quanta 3D FEG). The FIBing procedure starts with protecting the irradiated surface with a Pt deposition layer. After that, ion bulk (rough) milling is carried out at relatively higher parameters of voltage and current (30 kV and 7 nA). Then, bulk (rough) cleaning takes place at lower current, in the range of 3 nA. After finishing the rough cleaning, the lamella is welded to an inserted needle after cutting the roughly cleaned lamella. Then, the lamella is moved and attached to a TEM grid before starting the thinning procedure. The used current during the thinning procedure starts at 3 nA and finishes at 0.1 nA. Finally, final thinning is performed using 5 kV and 48 pA for at least 5 minutes until reaching a thickness less than 100 nm. During the FIBing procedure, caution must be made to protect the irradiated part of the sample (around 1 µm below the Pt deposited layer). Figure 5.3 shows the FIBed sample after the FIBing procedure.

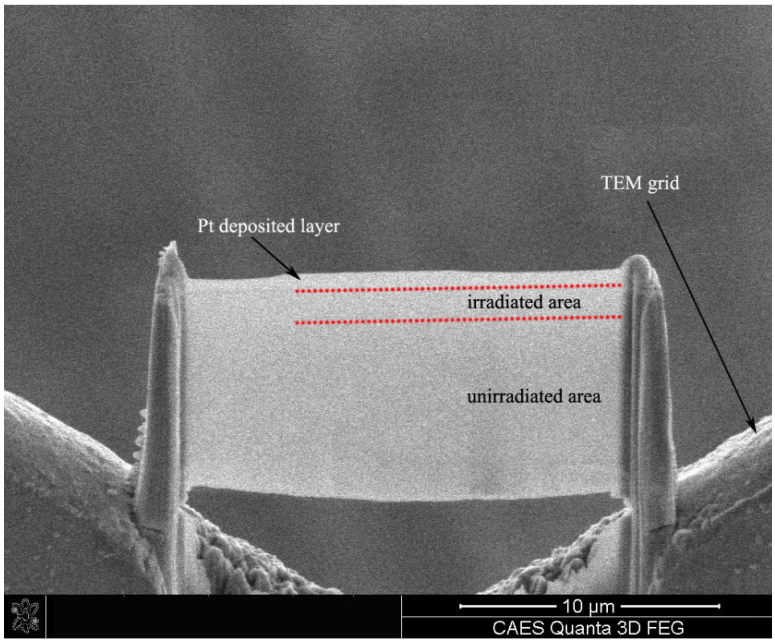

Figure 5.3 The FIBed sample showing the Pt deposited layer, irradiated and unirradiated area.

For detailed microstructural characterization, TF30-FEG Transmission Electron Microscope with STEM mode operated at an accelerating voltage of 300 kV was utilized. The FIBed samples were attached to a copper TEM grid in order to be examined inside the TEM. The dislocation density of prepared samples was estimated while samples were oriented in a two-beam condition. Also, the electron energy loss spectrum (EELS) technique was applied to estimate the sample thickness. The TEM images of irradiated samples were obtained from the irradiated area in the FIBed sample; however, unirradiated area was used for investigating the unirradiated condition.

Finally, a Hysitron Nanoindenter (model TI-950 TriboIndenter) was used for the hardness measurement as a function of depth. The indentation was performed in a direction normal to the surface of the sample using constant time segment. The nanoindenter was employed to induce a penetration depth profile of 1000 nm using a pyramidal diamond tip (Berkovich type) with an included angle of 142.35°. Before starting the indentation testing, a total of 100 indents in a fused silica reference material at various loads were performed to calibrate the tip geometry. The depth profile of hardness measurement was conducted via multi-cycling indentation technique. For each condition, more than ten arrays of indentations were collected for accuracy in order to estimate the damage profile. The hardness was performed on the original polished samples (14 mm diameter and 0.7 mm thickness) where the hardness of the irradiated samples was obtained within the rastering region.

5.3.Results and discussion

5.3.1. Microstructural characteristics of the as-received condition

The microstructure of the as-received Grade 92 steel is shown in Figure 5.4. Figure 5.4a shows the optical micrograph of the typical tempered martensitic structure. Figure 4.5b

shows the bright-field TEM microstructure of the as-received Grade 92 steel. The microstructure shows a tempered ferritic-martensitic (FM) structure with high dislocation density. The elongated lath structure was dominant. The dislocation density was measured to be $(3.9\pm0.8) \times 10^{14}$ m^{-2}.

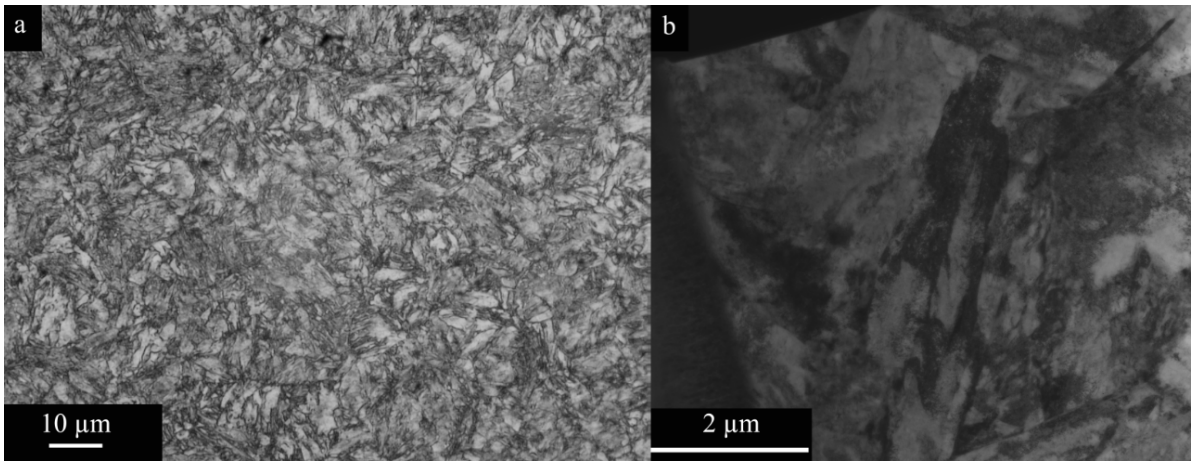

Figure 5.4. The micrograph of the as-received Grade 92 steel showing (a) an optical micrograph and (b) bright-field TEM image.

5.3.2. The microstructural evolution of irradiated samples

Figure 5.6 shows the bright-field images of irradiated samples for different conditions at low magnification. According to the estimated damage profile, the maximum damage will occur at 1 μm. It should be noted that dose level is different at varying depths and will not be constant as a function of depth; however, damage profile should be constant across the surface of the samples [25]. As observed in Figure 5.6, the irradiated samples did not show any visible defects.

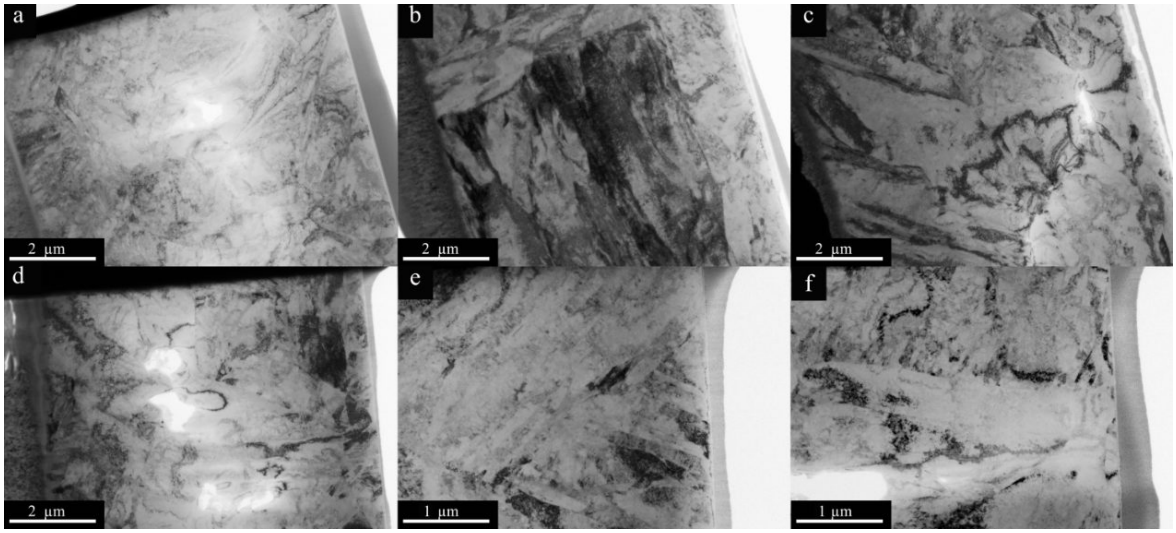

Figure 5.6. The bright-field TEM images of irradiated microstructures of Grade 92 steel under different irradiation conditions: a) 10 dpa and 30°C at 2.9kx, b) 50 dpa and 30°C at 2.9kx, c) 100 dpa and 30°C at 2.9kx, d) 10 dpa and 500°C at 2.9kx, e) 50 dpa and 500°C at 5.9kx and f) 100 dpa and 500°C at 5.9kx.

The irradiation-induced damage evolution of irradiated samples at 30°C as a function of damage dose (dpa) is shown in Figure 5.7. The irradiated samples did not show any distinctly resolvable irradiation induced precipitates, dislocation loops or voids. However, the irradiated samples show the presence of irradiation-induced defect clusters appear as 'black dots' and the overall concentration of these clusters increased when increasing dose. The high density of induced clusters in the form of dots did not appear beyond irradiated areas. For instance, the unirradiated area did not show any form of clustering which confirm the fact that these clusters were not the artifacts induced by FIBing.

The number density of irradiation-induced defect clusters was estimated to be 0.09, 1.5 and 1.7 for samples irradiated at 10, 50 and 100 dpa at 30°C. The size of these defect clusters at 30°C was very small after irradiating the sample at 10 dpa and increased to saturate around 3~4 nm for sample irradiated at 50 and 100 dpa. The irradiation dose enhanced the formation of the induced defect clusters; however, the number density of these defects saturated at later stages which can be attributed to the limited mobility of clusters at 30°C.

It has been noted in literature that the irradiation-induced damage enhances defects formation within the displacement cascade [24, 25]. The defect clusters can migrate away from the cascade if they become stable. However, the various defects present in the microstructure, such as dislocations and grain boundaries, can act as defect sinks where the vacancies/interstitials creating these clusters might be absorbed [25]. As the irradiation dose increases, the irradiation-induced cluster formation become more pronounced [25]. For instance, the irradiation-induced clusters were formed at lower dose in NF616 (i.e. around 2.5 dpa) when samples were irradiated with Kr ion and the size of the induced-clusters did not change at higher temperature (i.e. 200°C) [10]. The defect cluster density in irradiated NF616 steel showed similar behavior where cluster density increased as dose increased [10]. Also, the saturation density of defect clusters by the work by Topbasi *et al.* [10] decreased as temperature increased which was consistent with the obtained results.

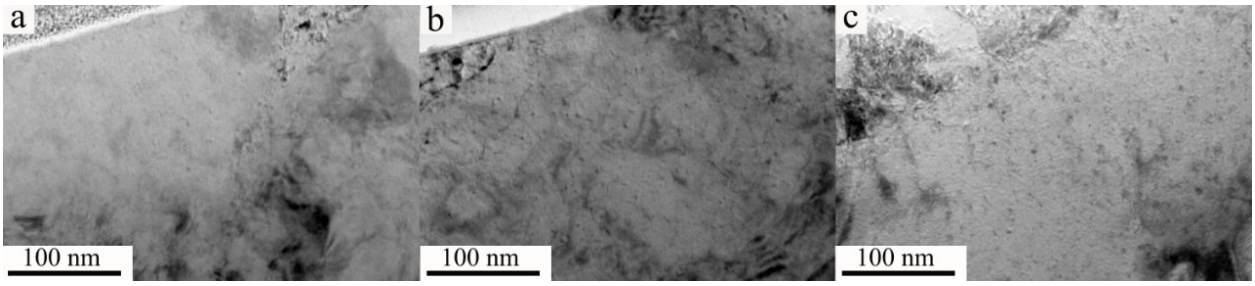

Figure 5.7. The bright-field TEM images of irradiated microstructure at 30°C and a) 10 dpa, b) 50 dpa and c) 100 dpa.

On the contrary, samples irradiated at higher temperature (i.e. 500°C) did not show any voids or cavities. However, some dislocation loops were found in the sample irradiated at 50 dpa and 500°C, Figure 5.8. For instance, the irradiation-induced vacancies and interstitials give rise to dislocation loops as they can shrink or grow depending of the irradiation flux [25]. The irradiation-induced interstitials form the dislocation loops while the irradiation-induced vacancy agglomerate into platelets which collapse so that the dislocation loops can

be formed [25]. At higher irradiation temperatures, the irradiation-induced dislocation loops becomes more stable as they grow in size reaching a critical size [25]. After that, they remain stable within the microstructure and they might interact with other induced loops or with the microstructure dislocation networks already present in the microstructure [25]. However, the observed dislocation loops for sample irradiated at 50 dpa and 500^{o}C, Figure 5.8, was localized within the observed microstructure. Also, the other irradiated samples at 500°C (10 and 100 dpa) did not show any observable induced defects which was attributed to the higher rate of the recovery processes at 500°C.

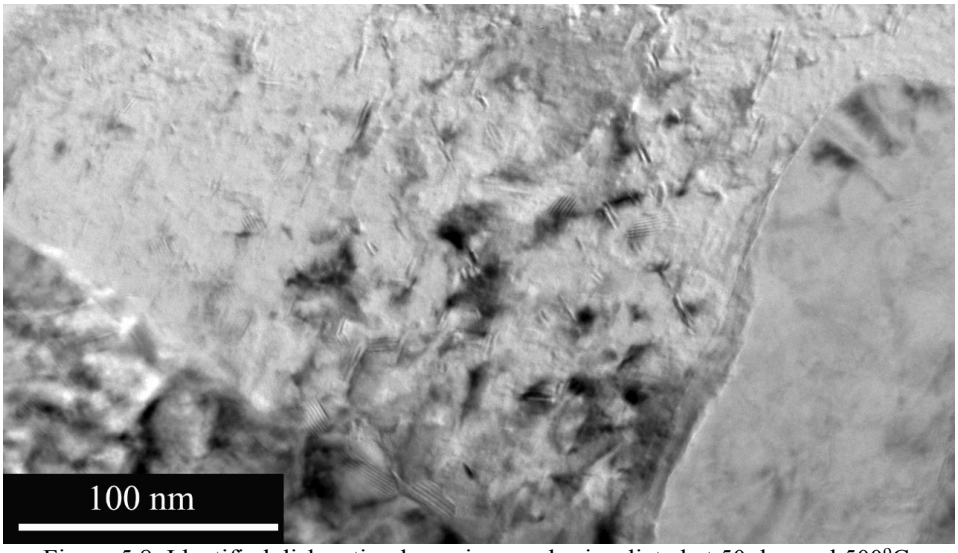

Figure 5.8. Identified dislocation loops in samples irradiated at 50 dpa and 500^{o}C.

Beside the obtained radiation defect clusters at 30°C, both the irradiated samples at 30° and 500°C did not show any significant radiation-induced damage. On the other hand, the work by Jin *et al.* [26] reported the occurrence of radiation-induced segregation when P92 steel (9Cr-2W) was irradiated to 34.5 dpa using Ar ion at room temperature. For instance, the radiation-induced segregation was reported to increase as temperature increased and/or dose increased as they enhance the solute atom diffusivity which was called radiation-enhanced diffusion (RED) [16]. However, the current investigated steel (9Cr-2W) did not

show that type of black dots even at higher dose of 50 and 100 dpa at 30 and 500°C. Also, the work by C. Topbasi *et al.* [10] did not find any induced segregation after irradiating the NF616 steel (9Cr-2W) with Kr ion at 200°C and up to 7.6 dpa.

The investigated samples did not show any cavities such as bubble or void at 30 and 500°C. For instance, it can be noted that the elevated temperature is defined as a key factor for the cavity formation. The current investigation was conducted at 30 and 500°C which might suggest that the investigated temperatures were insufficient for enough atom mobility to nucleate and form cavities as the low defect mobility limits the growth of defects. For example, the ferritic-martensitic steel (Grade 91) irradiated at low temperature with mixed proton and neutron spectra did not show any void formation [27]. That is why as the irradiation temperature was raised to 550°C [17], some very small voids were obtained in P92 steel at 7 dpa (void swelling rate ~ 0.03%) and these voids remained very small even at higher dpa of 12 (void swelling rate ~ 0.044%). It should be noted that other ferritic-martensitic steel showed some cavities at higher temperatures around 550°C [28-31]. In short, the investigated Grade 92 steel in the current work did not exhibit any voids at 500°C even after being irradiated at 100 dpa.

The diffraction patterns in samples irradiated to 100 dpa at 30 and 500°C are shown in Figure 5.9. The diffraction pattern shows the typical bright and diffraction spots without any faint diffraction rings. Hence, the irradiated sample did not show any amorphization process since the diffraction patterns did not contain amorphous halos, faded diffraction beam intensities or loss of diffraction contrast. The definite amorphization of Grade 92 was obtained at higher dpa at room temperature (i.e. 230 dpa and room temperature in Jin *et al.* [26]) where the amorphization was evidenced by the loss of diffraction contrast and the

appearance of amorphous halos. However, in the current work, the maximum dose was 100 dpa and the investigated samples did not show any irradiation-induced amorphization at that dose. At temperature above 230°C, Grade 92 steel is not expected to undergo any amorphization as that certain temperature (230°C) was defined as the controlling temperature below which amorphization is expected at sufficient dose [26, 32-33]. At elevated temperatures, the induced annealing action at high temperature reduces the lattice disorder [26, 32-33]. Also, the elevated temperature enhances the recrystallinity of irradiation-induced amorphous peripheries within the matrix which might prevent the irradiation-induced amorphization [26, 32-33].

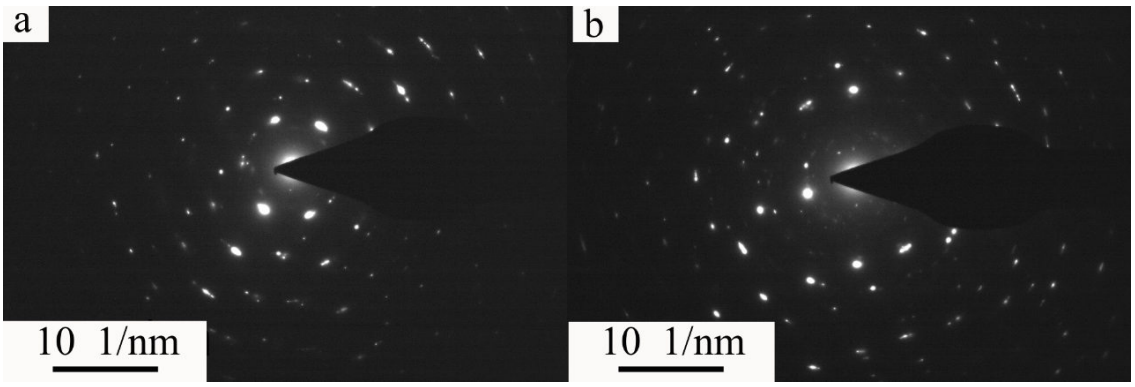

Figure 5.9. The diffraction patterns of Grade 92 matrices irradiated to 100 dpa at a) 30 and b) 500°C.

The dislocation density of the irradiated and unirradiated samples was measured from TEM micrographs taken under two-beam conditions such as shown in Figure 5.10. Firstly, the irradiated samples showed higher dislocation densities than the unirradiated condition. In addition, the dislocation structure showed a gradual increase in the dislocation density as dose increased at 30°C.

At higher irradiation temperature (500°C), the dislocation structure of the irradiated samples was less dense than those at 30°C. Still, the dislocation structure of irradiated samples was denser than the unirradiated conditions at 500°C.

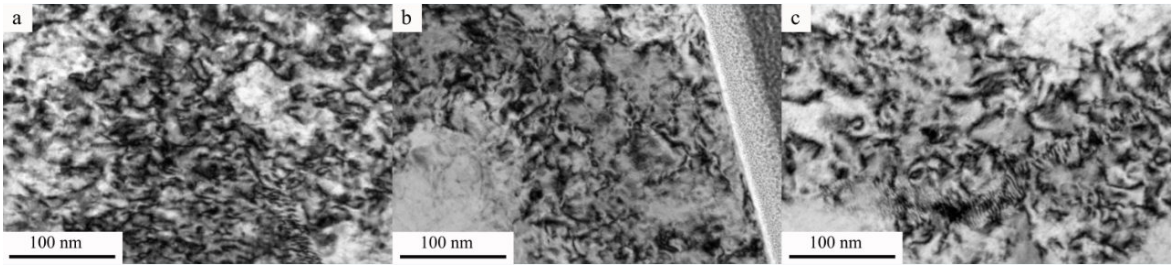

Figure 5.10. TEM images under two-beam conditions of irradiated sample at a) 10 dpa and 30°C, b) 50 dpa and 500°C and c) 100 dpa and 500°C.

Figure 5.11 shows the quantitative dislocation density of the investigated samples. At 30°C, the dislocation density increased from 3.9×10^{14} m^{-2} for the unirradiated condition to reach 4.3×10^{14}, 4.7×10^{14} and 5.3×10^{14} m^{-2} for samples irradiated at 10, 50 and 100 dpa, respectively. The ion implantation enhances dislocation density [25]. For instance, the dislocation density increased as a response to the high surface stresses caused by the high dose of implanted surfaces during the ion implantation process.

At higher temperature (500°C), it should be noted that dislocation density of the unirradiated condition was estimated from the unirradiated region of the sample irradiated at 100 dpa and 500°C. The sample irradiated at 10 dpa and 500°C was subjected to less irradiation time at higher temperature (i.e. 500°C) during the irradiation process which would explain the higher dislocation density compared to the irradiation conditions at 50 and 100 dpa at the same temperature. Also, it should be noted that the dislocation densities at elevated temperature did not change much indicating the annealing effect taking place over a longer time in case of 50 dpa and 100 dpa while irradiating the samples at elevated temperature, as shown in Table 5.2.

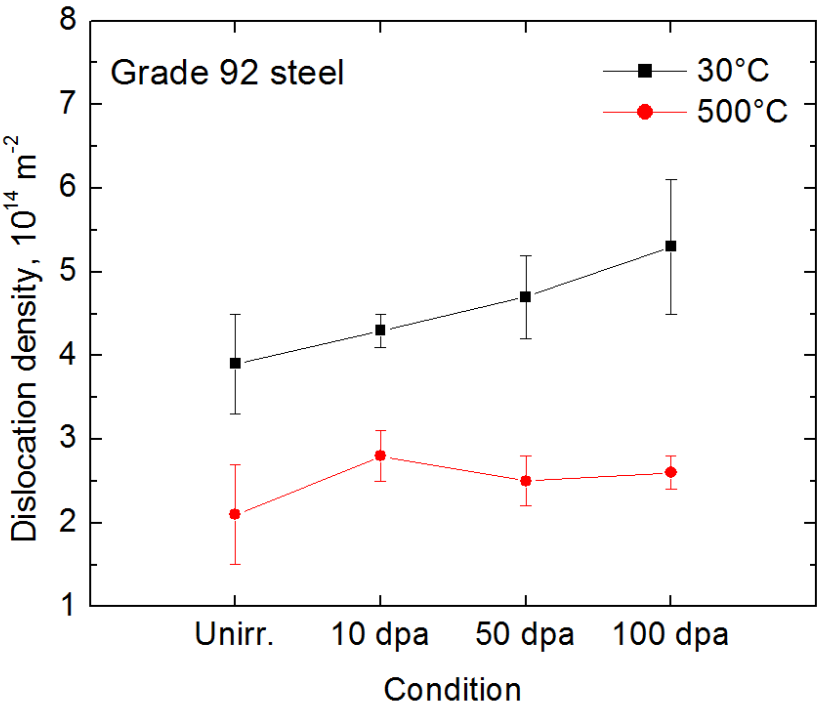

Figure 5.11. The dislocation density of the investigated samples for different conditions.

5.3.3. Nanoindentation results

Figure 5.12 shows the hardness data as a function of indentation depth for different conditions. More than 10 arrays of testing were performed for each condition to ensure the accuracy of testing. The hardness was measured for samples irradiated at room temperature (30°C) and elevated temperature (500°C). Irradiation with Fe^{+2} ions was conducted to induce damages of 10, 50 and 100 dpa.

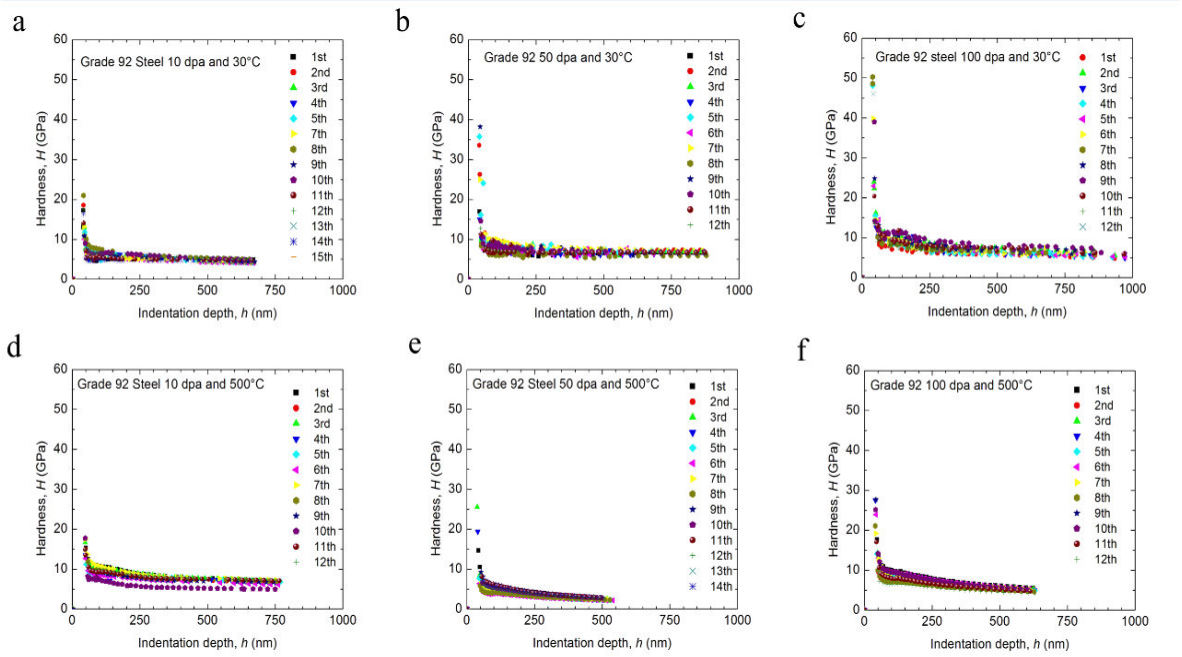

Figure 5.12. The hardness profiles as a function of depth for Grade 92 steel irradiated at a) 10 dpa and 30°C, b) 50 dpa and 30°C, c) 100 dpa and 30°C, d) 10 dpa and 500°C, e) 50 dpa and 500°C and f) 100 dpa and 500°C.

The irradiated samples at room temperature (30°C) showed an evident hardening phenomenon; thus, the hardness increased as the dose increased. At high irradiation temperature (500°C), the irradiation hardening was less pronounced. For instance, the hardness results showed lower hardening at the higher temperature after comparing the obtained hardness profiles. Clearly, the higher irradiation dose conditions had higher hardness, especially in the near-surface region, less than 300 nm. So, the monotonous increase of hardness with increasing fluence was obtained. However, the irradiated material (10 dpa and 500°C condition) showed higher hardness in the near-surface region than 50 dpa and 500°C. Figure 5.13 shows a derivative plot of Figure 5.12 where the hardness data will be plotted as a function of depth (at 250 nm). The hardness at 250 nm showed a gradual increase at 30°C which can be attributed to the irradiation-induced hardening. However, at elevated temperature 500°C, the hardness showed gradual decrease and increased afterwards. Thus, irradiation-induced hardening will take place taking into account two

processes (1) the induced hardening generated by the induced defects and (2) the enhanced structure recovery at elevated temperature. According to reported time under irradiation (Table 5.2), the lower hardening was obtained for the irradiated sample at 500°C and 50 dpa (417 min.) which indicate the enhanced structure recovery at 500°C. Similar observations were reported by Allen el al. [24] that the induced hardening of the irradiated steels showed a gradual decrease as the irradiation temperature increased [24]. For instance, the recovery of the irradiation-induced defects occurred at higher rates more than the induced hardening associated with microstructural defects [19-23].

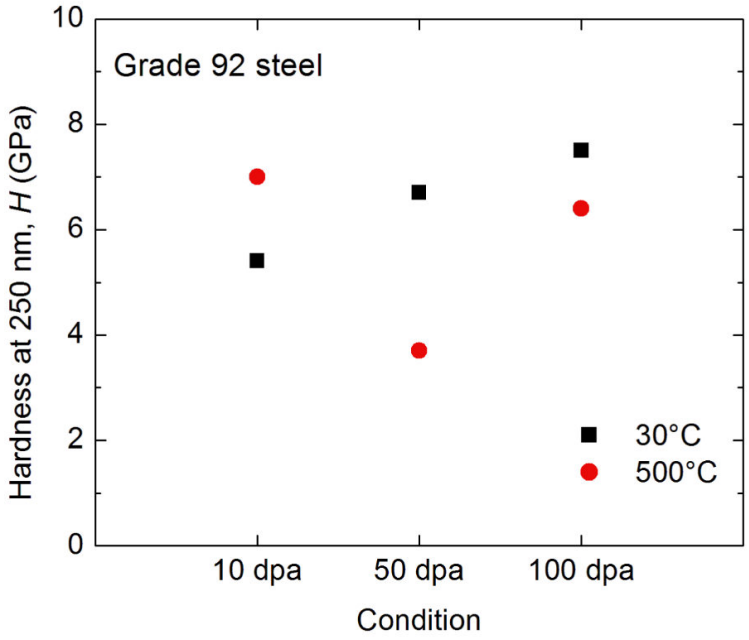

Figure 5.13. Derivative plot of Figure 5.12 shows the hardness as a function of depth (at 250 nm).

5.4.Conclusion

The heavy irradiation damage in Grade 92 using iron-ion irradiation was conducted to 10, 50 and 100 dpa at 30 and 500°C in the present study. The microstructural evolution of

the irradiated samples and the nanoindentation hardness data was investigated to assess the irradiation-induced damage. The main results can be summarized as follows:

1. The irradiation-induced hardening was obvious and hardness increased as dose increased at 30°C. But the irradiation-induced hardening was less definite at elevated temperature (500°C) as annihilation mechanism becomes more pronounced. This was accompanied by the higher dislocation density of samples irradiated at 30°C.
2. The irradiated samples at 30°C showed the presence of irradiation-induced defect clusters appearing as dots in the irradiated area and the density of these clusters increased as dose increased. At higher temperature (500°C), some dislocation loops were found in the sample irradiated at 50 dpa and 500°C.
3. The number density of the irradiation-induced clusters at 30°C increased as dose increased and they saturate in size (3~4 nm) at 50 and 100 dpa.
4. The investigated samples did not show any cavities such as bubble or void under these testing parameters.

References

[1] R. L. Klueh, R. Donald, R. Harries, High Chromium Ferritic and Martensitic Steels for Nuclear Applications, W. Conshohocken, PA, 2001.

[2] M. Yurechko, C. Schroer, A. Skrypnik, O. Wedemeyer, J. Konys, J. Nucl. Mater. 432 (2013) 78-86.

[3] F. Abe, T. Horiuchi, M. Taneike, K. Sawada, Mater. Sci. Eng. A 378 (2004) 299-303.

[4] R. L. Klueh, J. M. Vitek, J. Nucl. Mater. 182 (1991) 230-239.

[5] G.S. Was, P. Ampornrat, G. Gupta, S. Teysseyre, E.A. West, T.R. Allen *et al*, J. Nucl. Mater., 371 (2007), 176–201.

[6] P. Ampornrat, G. Gupta, G.S. Was, J. Nucl. Mater., 395 (2009), 30–36.

[7] R.L. Klueh, P.J. Maziasz, Metall. Trans., 20A (1989) 373-382.

[8] R.L. Klueh, A.T. Nelson, J. Nucl. Mater. 371 (2007) 37-52.

[9] F. Abe, Strengthening mechanisms in creep of advanced ferritic power plant steels based on creep deformation analysis, in: Y. Weng, D. Hand (Eds.). Advanced Steels: The Recent Scenario in Steel Science and Technology, Metallurgical Industry, Beijing,2011, pp. 409-22.

[10] C. Topbasi, A. Motta, M. Kirk, J. Nucl. Mater. 425 (2012) 48-53.

[11] K. Sawada, M, K. Murayama, R. Ishii, M. Yamada, Y. Nygae, R. Komine, Metall. Mater. Trans. A 267 (1999)19-25.

[12] M. Horsten, M. Osch, D.S. Gelles, M.L. Hamilton, in: M.L. Hamilton, A.S. Kumar, S.T. Rosinski, M.L. Grossbeck (Eds.), Effects of Irradiation on Materials: 19th International Symposium, ASTM STP 1366, American Society for Testing and Materials, 2000, p. 579.

[13] M.A. Kirk, P.M. Baldo, A.C.Y. Liu, E.A. Ryan, R.C. Birtcher, Z. Yao, Sen Xu, M.L. Jenkins, M. Hernandez-Mayoral, D. Kaoumi, A.T. Motta, Microsc. Res. Tech., 72 (2009) 182-186.

[14] S. Jin, L. Guo, Z. Yang *et al.*, Mater. Charact. 68 (2011) 136–142.

[15] R. L. Klueh, J. J. Kai, D. J. Alexander, J. Nucl. Mater. 225 (1995) 175-186.

[16] S. Jin, L. Guo, T. Li et al, Mater. Charact. 68 (2012) 63–70

[17] R.L. Klueh, J.M. Vitek, J. Nucl. Mater. 132 (1985) 27-31

[18] E.I. Samuel, B.K. Choudhary, D.P. Rao Palaparti, M.D. Mathew, Procedia Eng. 55 (2013) 64-69.

[19] X. Liu, R. Wang, A. Ren *et al.* J. Nucl. Mater. 444 (2014) 1–6

[20] C. Heintze, C. Recknagel, F. Bergner, M. Hernandez-Mayoral, A. Kolitsch, Nucl. Instrum. Methods B, 267 (2009) 1505–1508.

[21] R. Kasada, Y. Takayama, K. Yabuuchi, A. Kimura, Fusion Eng. Des., 86 (2011) 2658–2661.

[22] K. Katoh, M. Ando, J. Nucl. Mater. 323 (2003) 251–262

[23] P. Hosemann, C. Vieh, R.R. Greco, S. Kabra, J.A. Valdez, M.J. Cappiello, S.A. Maloy, J. Nucl. Mater., 389 (2009), 239–247.

[24] T.R. Allen, L. Tan, J. Gan, G. Gupta, G.S. Was, E.A. Kenik, S. Shutthanandan, S. Thevuthasan, J. Nucl. Mater., 351 (2006) 174-186.

[25] G. Was, Fundamentals of Radiation Materials Science: Metals and Alloys, first ed., Springer, Berlin, 2007.

[26] S. Jin, L. Guo, Z. Yang *et al.*, Mater. Charact. 62 (2011) 136-142.

[27] B.H. Sencer, F.A. Garnerb, D.S. Gellesb, G.M. Bondc, S.A. Maloy, J. Nucl. Mater., 307–311 (2002) 266–271.

[28] C.H. Zhang, K.Q. Chen, Y.S. Wang, J.G. Sun, B.F. Hu, Y.F. Jin *et al.*, J. Nucl. Mater., 283 (2000) 259–262.

[29] C.H. Zhang, J. Jang, M.C. Kim, H.D. Cho, Y.T. Yang, Y.M. Sun, J. Nucl. Mater., 375 (2008) 185–191.

[30] E. Wakai, T. Sawai, K. Furuya, A. Naito, T. Aruga, K. Kikuchi *et al.*, J. Nucl. Mater., 307 (2002) 278–282.

[31] F. Zhao, J.S. Qiao, Y.N. Huang, F.R. Wan, S. Ohnuki, Mater. Charact., 59 (2008) 344–347.

[32] H. Tanigawa, H. Sakasegawa, H. Ogiwara, H. Kishimoto, A. Kohyama, J. Nucl. Mater., 367 (2007) 132–136

[33] X. Jia, Y. Dai, J. Nucl. Mater., 318 (2003) 207–214.